Static and Dynamic Performance of Ti Foams

DPhil Thesis

Petros Siegkas
Worcester College
Department of Engineering Science
University of Oxford

Hilary Term 2013

Summary

Titanium (Ti) foams of different densities 1622-4100 Kgm^{-3} ($\bar{\rho} = 0.36 - 0.9$) made by a powder sintering technique were studied as to their structural and mechanical properties. The foams were tested under static and dynamic loading. The material was tested quasi statically and dynamically under strain rates in the range of 0.001-2500 s^{-1} and under different loading modes. It was found that strain rate sensitivity is more pronounced in lower density foams. Experiments were complimented by virtual testing. Based on the Voronoi tessellations a computational method was developed to generate stochastic foam geometries. Statistical control was applied to produce geometries with the microstructural characteristics of the tested material. The generated structures were numerically tested under different loading modes and strain rates. Voronoi polyhedrals were used to form the porosity network of the open cell foams. The virtually generated foams replicated the geometrical features of the experimentally tested material. Meshes for finite element simulations were produced. Existing material models were used for the parent material behaviour (sintered Ti) and calibrated to experiments. The virtual foam geometries of different densities were numerically tested quasi statically under uniaxial, biaxial and triaxial loading modes in order to investigate their macroscopic behaviour. Dynamic loading was also applied for compression. Strain rate sensitive and insensitive models were used for the parent material model in order to examine the influence of geometry and material strain rate sensitivity under high rates of deformation. It was found that inertial effects can enhance the strain rate sensitivity for low density foams and numerical predictions for the generated foam geometries were in very good agreement with experimental results. Power laws were established in scaling material properties with density. The study includes:

1. Information on the material behaviour and data for macroscopically modelling this type of foams for a range of densities and under different strain rates.
2. A proposed method for virtually generating foam geometries at a microscopic scale and examine the effect of geometrical characteristics on the macroscopic behaviour of foams.

Contents

List of figures

List of tables

List of notations

Abbreviations

ESEM	Environmental Scanning Electron Microscope
FE	Finite Element
FEA	Finite Element Analysis
HR	High Rate
LVDT	Linear Voltage displacement Transducer
MR	Medium Rate
MRI	Magnetic resonance imaging
QS	Quasi static
μCT	Micro computed tomography
SEM	Scanning electron microscopy

SHPB	Split Hopkinson Pressure Bar
XMT	X –ray micro tomography

Symbols

Roman letters

A_o	cross sectional area of bar
A_n	probability of each pore from the distribution curve
C_o	wave velocity
C	numerical constant
c_s	longitudinal wave propagation speed
d	cell size
D	specimen size
E	elastic modulus
E_f	foam stiffness
E_s	stiffness of cell wall material
G	shear modulus
h	height (or depth)
i	number of seed points
l	length
L	length
M	moment
n	numerical constant depending on cell type
P	force load
P_t	total porosity
P_M	macro porosity

P_m	micro porosity
R	Pearson's correlation coefficient
t	thickness
t	time
V	volume
V	interphase velocity
U_p	particle velocity
X	set of Voronoi cells
Y	foam geometry
Y_u	uniaxial yield stress

Greek letters

α	aspect ratio of the ellipse
ε	strain
ε_I	incident strain
ε_T	transmitted strain
ε_R	reflected strain
$\dot{\varepsilon}$	strain rate
ε_{eq}	equivalent strain
ε_m	mean strain
σ	stress
σ_m	mean stress
σ_{eq}	equivalent stress
ρ	density

$\bar{\rho}$	relative density
Ψ	material dependent constant

Acknowledgements

I would like to thank my supervisors Nik Petrinic and Vito Tagarielli for sharing their knowledge and experience, the friends from solid mechanics group with whom we shared offices and labs and finally I am grateful to my friends and family who have been supportive throughout the years.

1 Introduction

1.1 **Porous and cellular materials**

The word ‘cell’ derives from the Latin word ‘cella’ that is a small department or enclosed space and the word ‘porous’ originates from the Greek word ‘πόρος’ that means passage. They are often used to describe materials which are structures with these characteristics.

These materials can often be described by the ratio of the pore volume to the overall volume of the structure (porosity) or the ratio of the overall density to the parent material density (relative density). Porous materials can be either made artificially or found in nature where they have usually evolved to serve a function Figure 1-1. Their complexity and regularity can vary significantly ranging between topologically ordered structures (e.g. honeycombs) to very random and irregular (e.g. sponges). Manufacturers have recognized the favorable properties of cellular materials and are able to produce a wide range of porous structures based on application requirements. Such examples are bone implants, containments, thermal contactors e.t.c.

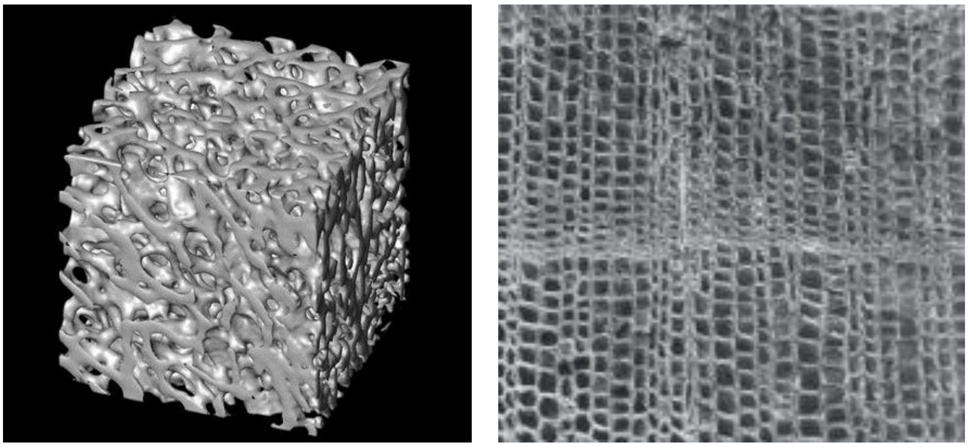

Figure 1-1 (Left) MRI reconstruction of human bone. [1, 2] (Right) SEM image of balsa wood. [2]

1.2 The role of titanium and alloys in gas turbine engines and bone Implants

Titanium holds many desirable properties amongst which it is possible to mention biocompatibility, high specific strength, resistance to corrosion, strain rate sensitivity [3-5]. These characteristics make Titanium and its alloys ideal for the design of aerospace components and implants. Some of these components that are typically made of Titanium alloys include: fan blades, compressor blades, stator vanes, compressor discs and containment casings Figure 1-2.

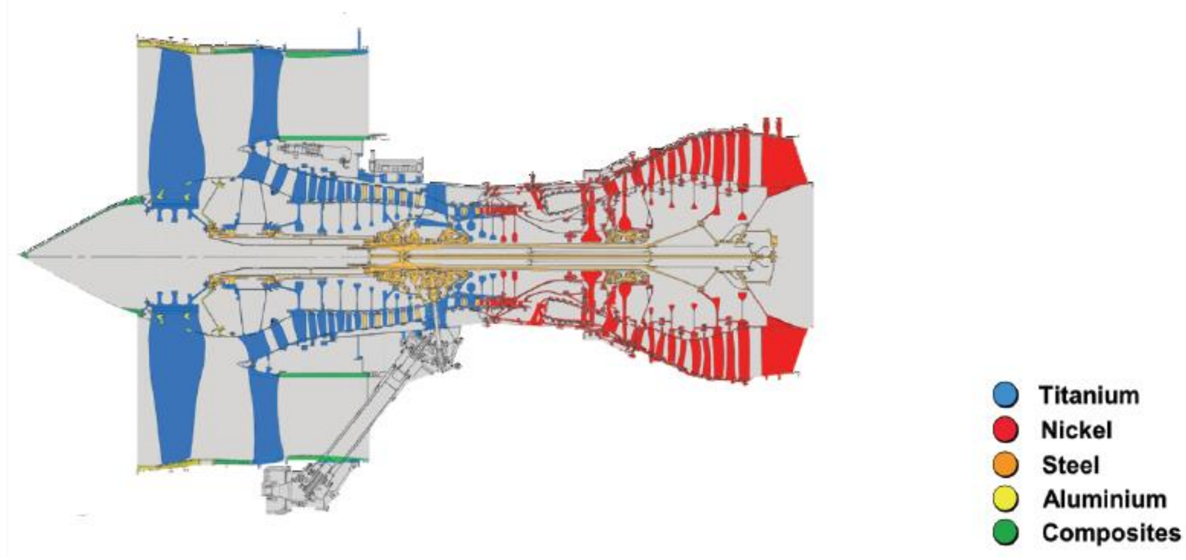

Figure 1-2 - Materials used in a typical gas turbine engine. [6]

1.3 Titanium foams

Porous and lattice materials have been found to exist in many structures from bones to spider webs, honeycombs and crystals , sponges and seeds as they fulfil the criteria for low weight to strength ratio, bouncy, high permeability and provide excellent protective casing at relatively high rates of deformation. The combination of materials and structures can be optimised to approach the requirements of biomechanical applications.

Using Titanium in porous structures offers a good mix of the properties of Ti alloys and the benefits of cellular structures. This combination can be extremely useful in cases of medical implants where the biocompatibility of Ti can be combined with a suitable porosity in order to match the bones stiffness (Figure 1-3). Furthermore the pores serve as scaffold for tissue development. The aerospace industry also uses cellular materials to combine the benefits of light weight, excellent energy absorption and strain rate sensitivity for confinement purposes.

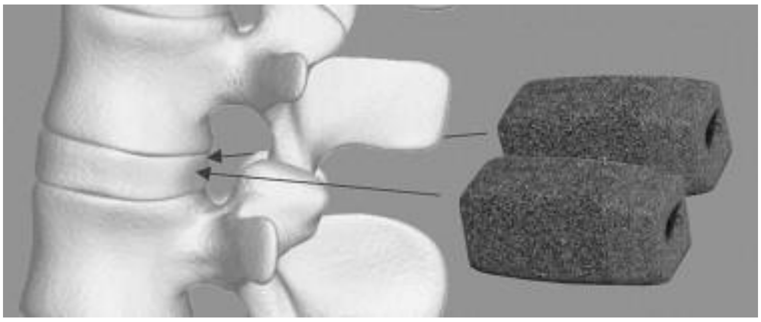

Figure 1-3 A posterior lumber interbody fusion device made of titanium foam (porosity of 65 %). The implant is 22 mm long and enlarged relative to the spinal column. [7]

1.4 **Objective and outline**

This research project is aimed at investigating and understanding the behaviour of stochastic Titanium foams of density 1622-4100 Kgm^{-3} $\bar{\rho} = 0.36 - 0.91$ under various different strain rates (10^{-3}-10^{3} s^{-1}). A method for replicating the foam geometries is developed in order to capture and explain the effect of structure to the macroscopic material properties. This is to allow for modelling of foams at a micron scale and potentially serve as a design tool for tailoring structures to application requirements.

- Experimental Study:
    1. Various foam densities where tested under three different strain rates in compression. The aim was to determine the strain rate sensitivity of the parent material and foam structures. High speed photography was employed.
    2. The parent material was tested in tension and compression at different strain rates.
    3. Quasi static tension and shear tests were performed for low density foams.
    4. SEM microscopy was used to examine the surface and pores of the foam structure.
    5. In situ SEM compression was performed to examine the deformation mechanisms of the structure.
    6. X- Ray Tomography was used to obtain the geometrical characteristics of the foam structure
- Modelling:
    1. A method was developed to virtually generate irregular foam structures. The method was used to replicate existing foam specimens and virtually generate specimens of different densities.
    2. The properties of the parent material were used to model the structure and FE methods were employed to replicate and compare the quasi static experiments of the foams.
    3. The foams were virtually tested by simulating different loading modes.

4. Strain rate sensitive and insensitive models were used for the parent material. Simulations of compression predictions under different strain rates were compared with experimental data.

Table 1-1, 2 shows a brief summary of the experimental and numerical work included in this thesis. The experimental work was application driven and restricted by the financial and time cost of the foam specimens and testing. The work was mainly focused on the compressive properties of the foams as it was expected to be their strongest quality.

The numerical work involved generating and simulating tests for virtual foam specimens simulated at a mesoscale level. The simulations were of fine meshed irregular geometries. Computational cost was a limiting factor in the number of density simulations and specimen size.

Experiments	Densities	Strain rates
Compression	4	3
Tension Foams	1	1
Tension sintered powder (4100 Kgm^{-3} , $\bar{\rho} = 0.9$)	1	3
Shear	1	1
Taylor impact	1	
SEM observation	4 (pre and post test)	
XMT observation	3	

Table 1-1 Summary of the main experimental work

FE simulations	Densities	Strain rates	Simulations
Compression	6	2	3 directions per density
Tension	2	1	3 directions per density
Shear	2	1	3 directions per density
Biaxial Compression	2	1	3 directions per density
Biaxial Tension	2	1	3 directions per density
Hydrostatic compression	2	1	3 virtual specimens
Hydrostatic tension	2	1	3 virtual specimens
Triaxial loading	1	1	2 virtual specimens X 2 modes X 3 directions

Table 1-2 Summary of the main numerical work.

2 Literature review

2.1 Overview of manufacturing methods for open cell metal foams

Metal foams hold many useful properties that make them suitable for a wide range of applications.

- Lightweight Structures: Very good stiffness to weight ratio.
- Biocompatible inserts: The texture promotes the development of tissue inside the pores
- Acoustic absorption: Sound absorbing abilities
- Vibration control: High natural flexural vibration frequency
- Energy management: Exceptional ability to absorb energy
- Thermal management: Open cell foams have large accessible surface
- Sandwich cores: Low density with good shear and fracture strength
- Strain isolation: Ability to take up strain mismatch by crushing at controlled pressure
- Mechanical damping: Damping capacity is up to 10 times larger than that of solid metals
- Buoyancy: Low density and corrosion resistance
- Packaging with high-temperature capability: Impact absorption at constant load coupled with thermal stability above room temperature

The foam properties relate to the material and structure of the foam. A number of manufacturing methods are used by industry. [8, 9]

The quality and consistency in the behaviour of foams is strongly dependant on the type of process used for its production [10].

2.1.1 Furnace sintered metal powders

The sintering operation is a high temperature process that causes the bonding of particles without significantly altering their shape. The volume fraction of porosity is associated with the degree of particle interconnectivity and particle size. It can be controlled by process variables such as compacted powder density, sintering temperature, time and alloying additions. A disadvantage of this method is that the pore size and shape are dictated by powder size and shape. For spherical powder particles porosity is limited to 50 % and the pore shape is highly non spherical (Figure 2-1). [11]

The sintering operation involved in Titanium and Titanium alloy porous materials requires a non oxidizing environment to achieve good bonding. This is due to the high activity of Ti at high temperatures that results in contaminating the ingredients with oxides. Highly contaminated material would hinder particle bonding. Thus it is necessary for a high vacuum oven (~10^{-5} mbar) and sintering temperatures of 1250 °C. [11]

Metal powders are used to fill a mold and then are sintered. Application of compaction force is not necessary and the process is called loose powder sintering [10, 12]. This may be considered as the simplest manufacturing route [13]. Compacted powders are also sintered but anisotropy effects have been observed in comparison to loose powders sintering. [14]

Ti alloy powders (Ti-6Al-4V) can be sintered loose at 1000 ^{o}C for times between 0.5-2 hours achieving porosities between 41-55 %. The strength is dictated by the necks formed between the powder particles. [15, 16]

The pore size, volume fraction, morphology and its distribution throughout the sample thickness and the inter particle neck size have an impact on the mechanical properties of the resulting material. Sintered metal powders are often very brittle with poor toughness and are prone to crack propagation at low stresses or at low impact energies. Under fatigue conditions, cracks are likely to initiate at the sintered necks of individual powder particles. Sintered coating is sometimes used to provide strong bonds between the powder spheres without significantly degrading the strength and corrosion resistance of the component. [11]

2.1.2 Sintered fibre metal

Metal fibres of the order of 10 μm may be produced using e.g. melt extraction, machining, drawing processes; to form metal foam structures. There are also commercially availiable fibres (Fibretech) [10, 17, 18]. The points of contact amongst fibres become bonds. A disadvantage of this technique is that fibres must be compacted to a form prior to sintering. The problem of ensuring good bonding lies in that the fibres may spring back during metal fibre compaction that can result to inadequate contact that would lead to poor bonding after sintering. [11]

The mode of failure between powder and fibre sintered foams is what differentiates these structures. This corresponds to the fact that the fibres do not fail by crack propagation. Failure occurs over large displacement range by means of tearing as rupture of the bonds between fibres. The porosity of metal fibre structures is limited up to 30-50 %. [11]

However Ducheheyne et al, reported porosities of 65-90 % by using interlocked fibre sheets that are then sintered for additional coherence. The sheets are intended for stabilising prosthetic devices. [19]

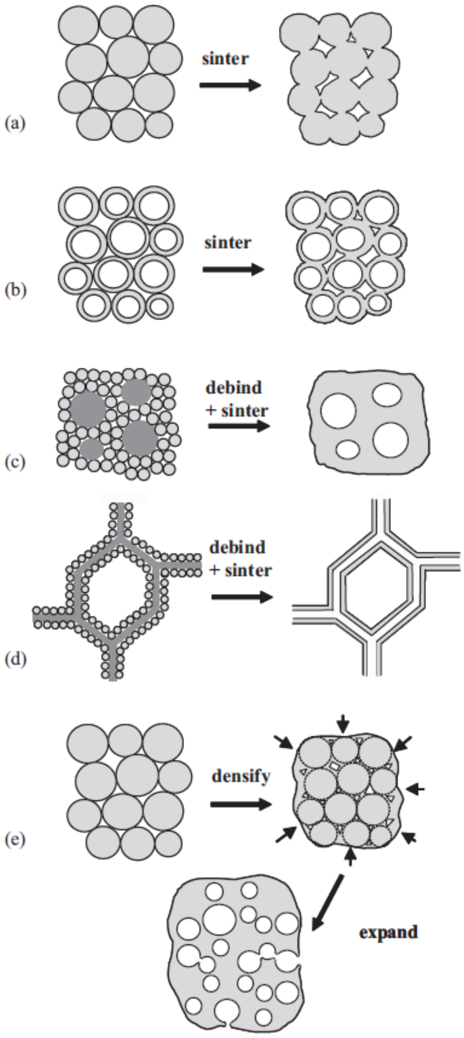

Figure 2-1 (a) Metal powder sintering, (b) hollow sphere sintering, (c) gas expansion, (d) powder sintering on scaffold, (e) powder densification and gas expansion. [20]

2.1.3 Space holder method

The space holder method is a process that can be used in order to produce foams with porosities greater than 50 %. The metal powders are mixed with a space holder material (e.g. a polymer) that would dissolve and evaporate at relatively low temperatures (Figure 2-2). The mixture is then compacted and the resulting pellet is subjected to heat treatment to remove the space holder material. The metal powders are sintered by progressively increasing the temperature to allow for densification of the structure and the improvement of the structural integrity. [20]

Various space holders may be used based on their shape and chemical features. Wenjuan N. et al, used carbamide on the basis of its spherical shape and its size can be controlled by reduction using water and ethanol dissolve. The powder particles were mixed with a binder and then the carbamide particles were added. Mixtures were compacted under pressures of 100-250 MPa and then heated up to 500 ^{o}C in a vacuum induction furnace to remove the carbamide and its dissociation products. After that sintering was done at 1250 ^{o}C for 3 hours. [21]

Esen and Bor used magnesium mixed with gas atomised spherical titanium powders of specific size distribution. A polyvinyl alcohol solution was added as binder for the poder mixtures and then titanium/magnesium mixtures of different ratios were cold compressed under 500 MPa. The mixtures were debinded and sintered while magnesium evaporated by heating the compacts slowly up-to 1200 ^{o}C. [22]

This method can produce foams with a close to homogeneous pore structure and porosities of 45-80 %.Variation of the size and shape of the space holder material can adjust the properties of the result foam. [20, 22]

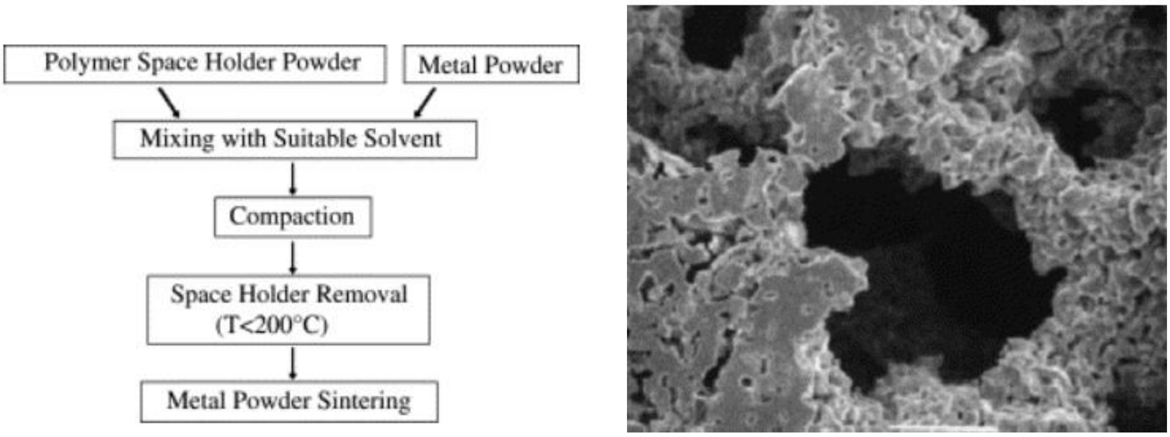

Figure 2-2 Foam fabricated by the space holder method. [11]

2.1.4 Replication

This method (Figure 2-3) is based in replicating an existing polyurethane foam scaffold. The composite pattern is immersed in Ti slurry comprising Ti_6Al_4V powder H_2O and ammonia solution [11]. Alternatively a polymer scaffold is repeatedly coated with a mixture of titanium powders and binder. After thermal removal of the scaffold and sintering at 1250-1300 ^{o}C in high vacuum, non-oxidising environment the powders form open cell foam with hollow struts is produced of up to 80 % porosity. [15, 23]

After repeating the procedure, densification and quality improvement is occurred as a result of correction of flaws in the Titanium struts. This process results in foams with high porosity consisting of three types of pores: primary on the surface of the hollow struts, secondary porosity at the core of the struts previously occupied by polyurethane and open tertiary porosity between struts. [11]

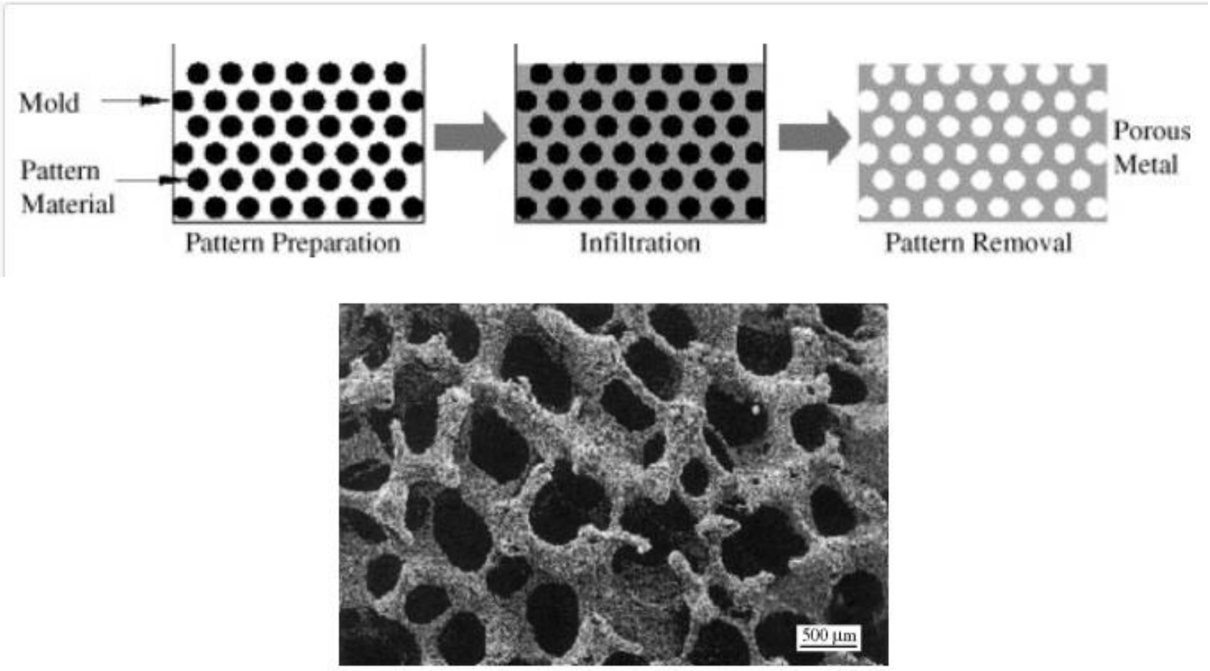

Figure 2-3 Foam created by deposition of powder on polyurethane scaffold. [11]

2.1.5 Combustion synthesis

This method is used in the production of high purity Ni Ti porous material by several authors [24-26]. Metal powders are placed in a container and are ignited after cold compression. The particles fuse as a result of a highly exothermic, self-sustaining reaction (Figure 2-4).

Ti and porous powders are mixed and blended by ball milling for 12 hours and then pressed into cylindrical compacts. A small hole is drilled on the side to accommodate a thermocouple and the compact is preheated to 350 ^oC. The preheated pellet is then ignited on one end and the combustion wave self-propagates along the axis to the other end of the compact. [27]

The mechanical properties of the resulting structure are controlled by the variation of the reactant particle size of the powders, the use of binder and the compaction pressure that affect the final microstructure and porosity of the sample. Porosity of ~54 % is reported to have been created mainly for test as implant material. [11, 24, 28]

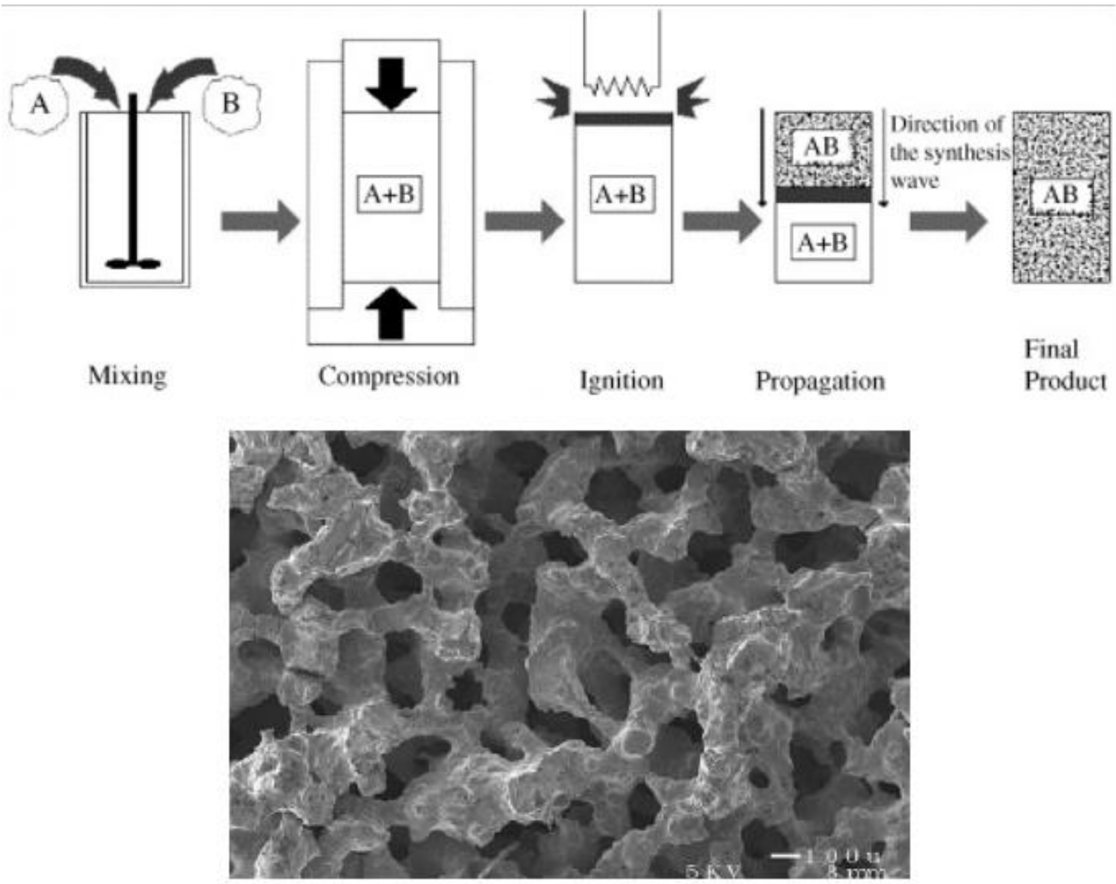

Figure 2-4 Resulting foam after compaction synthesis. [11]

2.1.6 Plasma spraying

Gas heated to extremely high temperatures (~20000 ^oC) to plasma conditions is shot through a gas gun accelerating and heating metal powders injected into the plasma jet stream. The melted powder particles impact onto the substrate material creating a porous foam coating (Figure 2-5) or fully porous structures. [11, 29, 30]

The degree of porosity varies depending on the spraying parameters. Coatings produced by this method are characterized by gradual change of porosity with the inner layer being very dense and pores gradually increasing in size as moving to the exterior. Even though the process is usually taking place in a vacuum environment issues of contamination and presence of impurity phases still exist. [11]

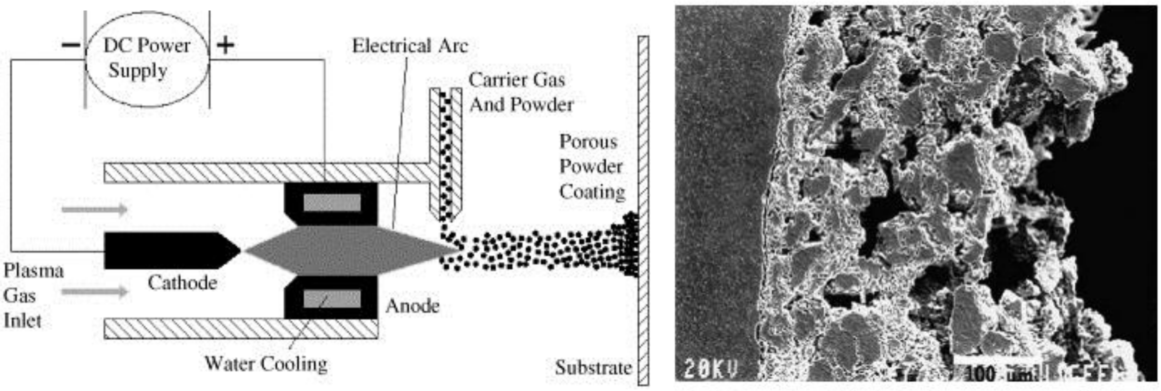

Figure 2-5 Plasma spraying technique (left), foam resulting of plasma spraying technique (right). [11]

2.1.7 Electrical field- assisted powder consolidation

This method is known by different names depending on author as field assisted consolidation technique (FAST) [30], spark plasma spraying (SPS) [31, 32], plasma activated sintering. [33] It is one of electrical field activated sintering and it involves the application of an external current to assist powder consolidation. The equipment consists of a uniaxial compression device and the electrical components to apply the pulsed and steady currents. The powder is directly placed into the punch and die unit. The device is commonly placed in a vacuum or specific gas environment (Figure 2-6). [11]

The consolidation process involves two stages (1) initial activation by applying a pulsed voltage and (2) heating and densification by using DC current. A pulse discharge can be achieved by applying a low voltage (~10 V) and a 600-1000 A current. A basic difference between FAST and EDC is the number of discharges: in EDC the electric energy is suddenly released where in FAST multiple discharges are applied. The sintering process of Ti and Ti alloys requires high temperature in high vacuum for a long period of time. This can be both difficult and expensive but it is useful in that the high current discharge can melt the oxide surface film on the powder particles and bring them into closer contact, improving the formed junctions. Produced Ti_6AL_4V porous specimens using this method were found to have a yield stress ranging from 270 to 530 MPa and ultimate compressive strength of 125 MPa for 32 % porosity. [11]

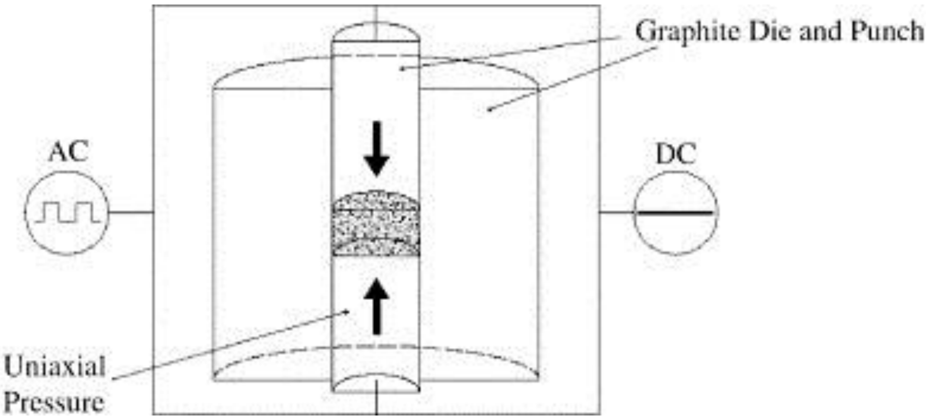

Figure 2-6 Electrical field assisted powder consolidation. [11]

2.1.8 Argon expansion process

Ti alloy powders are confined in a canister which is evacuated and filled with a neutral gas such as argon. The powders are then densified by hot isostatic pressing at 890 ^oC and 100 MPa for 125 minutes using commercially pure Ti powders and producing a matrix with confined argon inclusions. The canister is removed and the matrix is exposed to high temperatures (860 ^oC) that allow creep expansion and gas escape. Porosities up to 40 % are reported with pores varying in size as anisotropic expansion is occurred. [20, 34]

2.1.9 Rapid prototyping techniques

Manufacturing processes using a type of three dimensional printing technique are used to create either the precursor for the foam or directly the foam itself to create porous implants with controllable size, shape and distribution of porosity [11, 35]. The structure is achieved either by depositing slurry with an inkjet type of way [36], or by selective laser melting of powders at specific points that follow a 3D cad design of cellular solids. [37]

A 3D fibre depositing device (Figure 2-7) is used to place the material at each layer driven by specific software. The Ti_6Al_4V is mixed with a solution of methylcellulose and stearic acid. The slurry is stirred for 1 hour at room temperature to obtain homogeneity. The concentration of the Ti_6Al_4V powder in the slurries has influence on the viscosity of the slurry. [36]

In this way by layer after layer depositing, a three dimensional structure is formed. The sample is dried for 24 hours at room temperature and then for 24 hours at 50 ^oC. It is then sintered in high vacuum producing the final porous material. Variables such as Ti_6Al_4V powder concentration, air pressure, feeding speed and original height of fibre deposition are directly relevant to the final product of this procedure. Porosities of 40-70 % can be produced. This method has the advantage that complex geometries of foam- lattice materials can be achieved with significant control. No inner supporting structure that could leave remains in the material is needed during the process. These methods can be used for a range of materials in different temperatures. Nevertheless limitations exist on the nozzle size tip diameter speed and pressure for the depositing of the suitable fibres at each case. Some anisotropy might occur as the pore size is not equal in all directions (z in comparison to x,y). Pore occlusions may occur at the boundaries due to the deposition path that has a changing orbit. [11, 36]

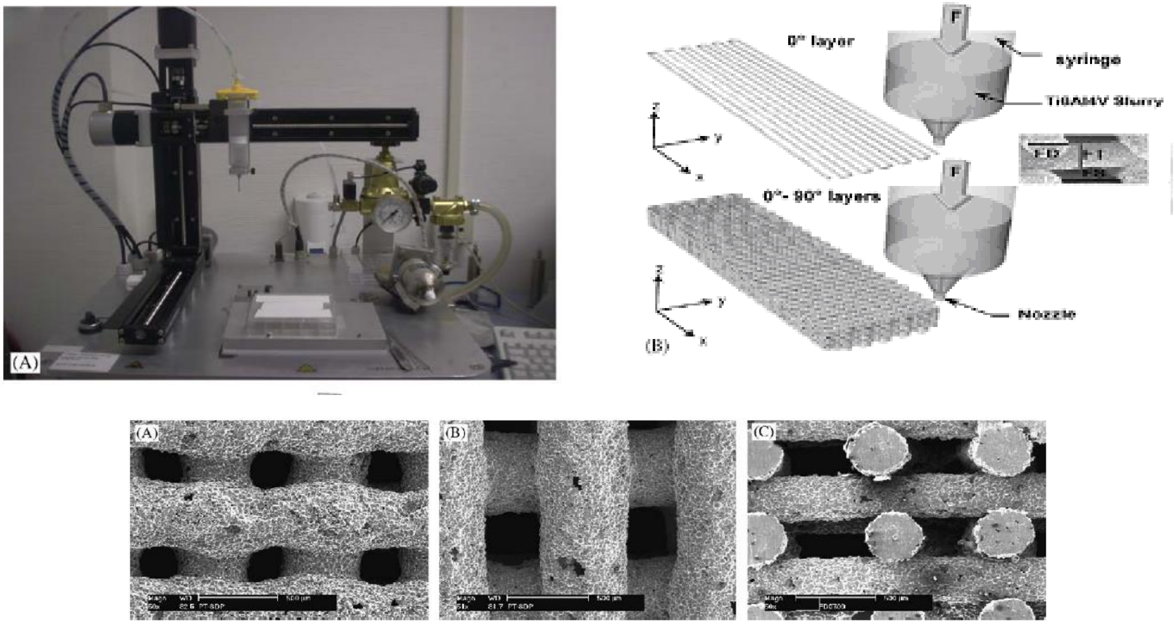

Figure 2-7 Bioplotter.[36]

2.2 Overview of experimental Procedures

In this section the experimental procedures used for the characterisation of foams are briefly described.

2.2.1 Structure analysis

Micro structural analysis is commonly used to derive information on the geometrical characteristics of foam structures. Sections from polished specimens are randomly chosen for analysis. Each section is photographed and the images are converted to binary black and white in order to measure the coordinates of the centroids of pores. [38]

2.2.2 Pores size distribution

The Soltykov area analysis is a method of constructing a 3D inclusions distribution from 2D area distribution analysis. Section areas in 2D images are studied and the pores in these sections are divided to n size groups. It is assumed that the largest diameter of 2D pore is equivalent to that of a 3D spherical inclusion in the microstructure. Based on this assumption the 3D pore size distribution can be projected from 2D images. The distribution can then be fitted to a statistical formula with specifically assigned parameters that would best describe the observation [38]. The assumptions of this method are not always true and can lead to errors.

2.2.3 X-ray tomography

X-ray tomography is a non-destructive method which provides 3D information of materials. It is often used for a wide range of materials in order to obtain information regarding geometrical features or perform in situ experiments (Figure 2-8). The specimen is placed between an X-ray source and a sensor (Figure 2-9). The specimen is rotated and the 2D images of the projections are collected by the censor. The images are then reconstructed and a stuck of images form a 3D representation of the specimen [39]. X-ray tomography may also be used for in situ testing to perform interrupted quasi static tests [7]. The use may be limited by the attenuation of the material in comparison to the source energy.

Getting 3D information can be performed at a great variety of experimental setups as well as sample configurations and size. Often it is achieved by performing a large number of radiographs while rotating a specimen between 0 and 180$^{o.}$ Tomography can be performed using different sources. Beams may be produced by a micro focus X-ray tube (divergent white beam spectrum) or synchrotron radiation. (high intensity monochromatic parallel beam often used to obtain higher resolution)

There different approaches in performing tomography. Some of these are:

Absorption tomography: Contrast is given as a result of the difference between the linear attenuation coefficient which corresponds to the atomic number of the elements and the density. The larger the difference the better the contrast. [39]

Phase contrast tomography: This contrast is observed when the beam is partially coherent and the distance between the sample and the detector is increased in comparison to the absorption mode. This contrast is superimposed to conventional absorption and it is efficient for edge detection. [39]

Holography: Images are taken at several samples to detector distances. The quantitative distribution of the optical phase can be retrieved. This approach requires more scans at various distances but it can obtain contrast when conventional absorption fails. It allows quantitative analysis in 3D of the density in the material. [39]

There are four main approaches to calculating the slice image given by the acquired views. These are called reconstruction algorithms. The first method is based on solving many simultaneous linear equations where one equation is written for every measurement. A particular sample in a particular profile is the sum of a particular group of pixels in the image. To calculate unknown variables there must be independent equations. This method is limited by computational time as it usually requires solving several hundred thousand simultaneous linear equations. [40]

The second uses iterative techniques that can be algebraic reconstruction technique (ART). The pixels in an image are set to some arbitrary value and an iterative process is then used to gradually change the image array to corresponding profiles. Similar methods are the simultaneous iterative reconstruction technique (SIRT) or iterative least squares technique (LIST) depending on how the successive corrections are made (ray by ray, pixel by pixel etc.). [40]

Filtered back projection is the evolution of the older back projection method which is formed by smearing each view back to the image in the direction it was originally acquired. The image pixels along the ray pointing to the sample are set to the same value. Simple back projection may result in blurry images. Filtered back projection corrects the blurring effect by filtering each view. Each of the one dimensional views is convolved with a one dimensional filtered kernel to create a set of filtered views. The views are back projected to provide the reconstructed image. [40]

The Fourier reconstruction involves the relationship between a two dimensional image and its set of one-dimensional views. The two dimensional Fourier transform of the image and the one dimensional Fourier transform of each of its side-views make it possible to examine the problem in the frequency domain. The frequency domain analysis of the problem is called the Fourier slice theorem. [40]

Limitations of the sensor or its environment may result to blurring which causes a point to spread out. The impulse response is often called point spread function [40]. The point spread function is used in image de-blurring techniques. [41], [42]

Some of the most common artefacts in tomography are:

- Streak artefacts are often seen around materials that block most X-rays, such as metal or bone. Numerous factors contribute to these streaks: under sampling, photon starvation, motion, beam hardening. [43-45]
- Beam hardening artefacts result from the preferential absorption of low energy photons from the beam. It is more pronounced in areas of large attenuation. [43, 44]
- Ring artefact results as the image of one or many "rings" appears within an image. This can be due to a detector fault, or miss-calibration. [43, 44]
- Noise may appear as grain on the image and is caused by a low signal to noise ratio. [43, 44]

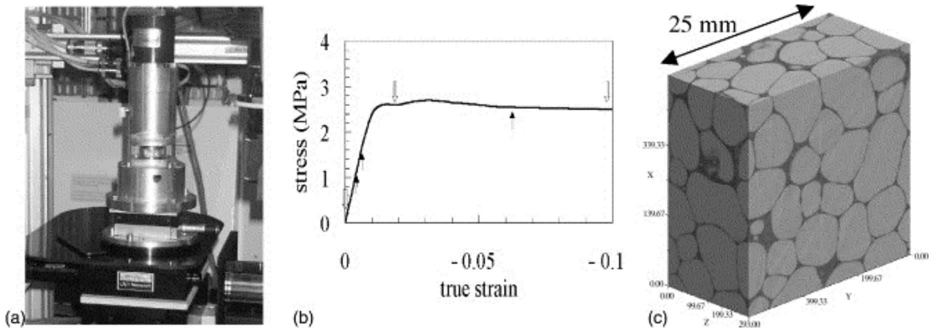

Figure 2-8. X ray micro tomography is often used to derive pore size distribution. [39]

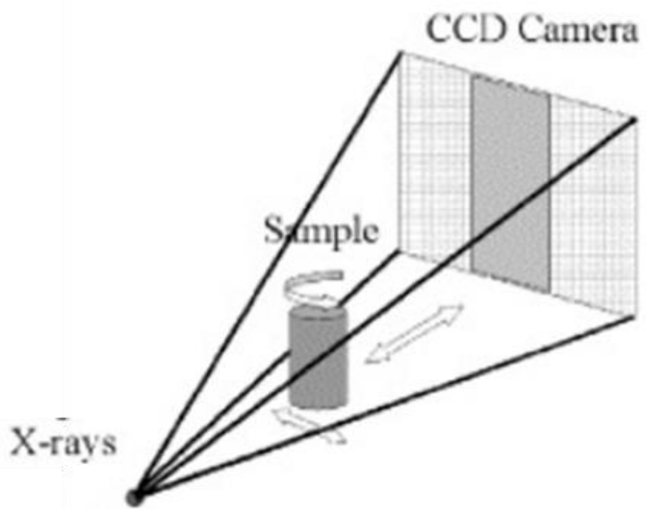

Figure 2-9 Typical x-ray scanner. [39]

2.2.4 Sample preparation

Compression foam samples are often cylindrical and are produced by low speed rotary saw with diamond coated blade, water jet cutting, or electrical discharge machining. Size effects usually depend on the specimen to cell size ratio. Ashby et al [46], found that the size effects in measured Young's modulus and Yield stress, tend to minimize as the ratio approaches D/d=7 (where D: specimen size and d: cell size) while the height to the diameter ratio is close to 1-1.5 Figure 2-10. [46]

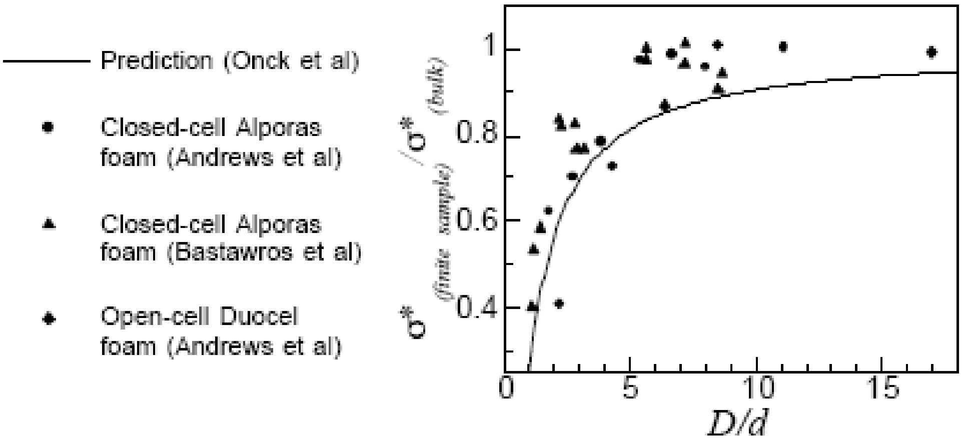

Figure 2-10 The effect of specimen dimension on the yield stress of a specimen normalized by that of the bulk foam where D: specimen size and d: cell size. [46]

2.2.5 Uniaxial compression testing

Several examples of uniaxial compression testing of foams are found in literature [47-49]. Force data are collected by resistive load cells and displacements can be measured by an external LVDT (linear voltage displacement transducer) placed between the loading platens or laser extensometer quasi statically and wave analysis in the case of high strain rate tests [50]. Greasing the surface of the specimen that are in contact with the loading platens reduces the frictional effect and can give a compressive strength that is up to 25 % higher than that of dry specimens [46], (Figure 2-11).

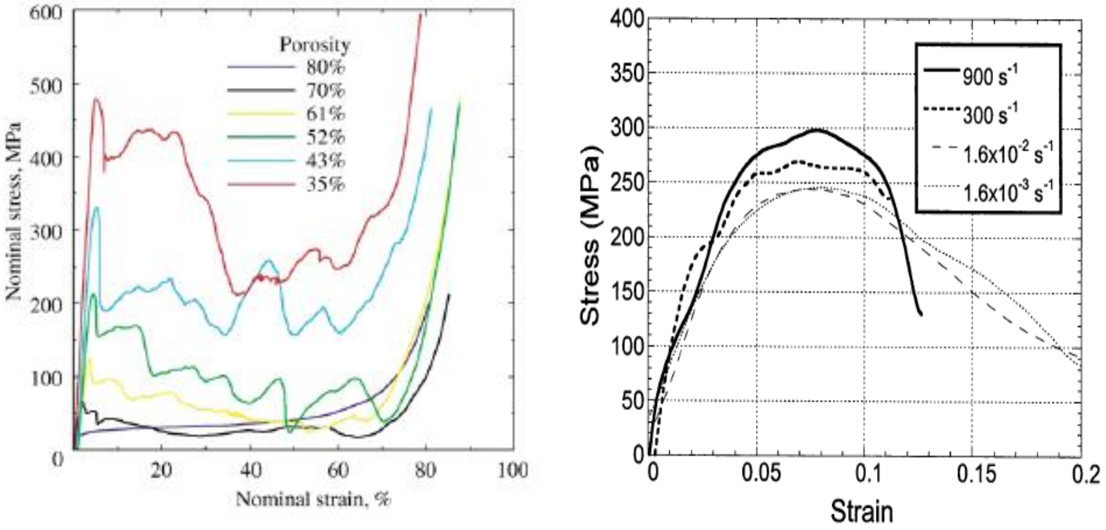

Figure 2-11 Nominal stress strain curve for pure Ti foam of different porosities made by the space holder method (left) [51] and Sintered powder of Ti6Al4V with 37 % porosity tested at different strain rates (right). [50]

2.2.6 Uniaxial tension

Uniaxial tension tests are usually performed on either waisted cylindrical or flat, dog bone specimens. The minimum dimension of the specimen should be at least 7 times the cell size to avoid size effects. Gripping is achieved by using grips with sandpaper or by adhesive bonding. Displacement can be measured by an extensometer attached on the specimen, a laser extensometer or image processing. Young’s modulus is measured by the unloading portion of the stress strain curve as in uniaxial compression. [48, 49]

2.2.7 Shear

Shear tests on metal foams are usually done by bonding a foam strip on two rigid plates attached to fixtures that load the specimen along its diagonal.[49, 52]. I-beam shaped specimens of rectangular cross-section allows reduction of stresses at the interface between the foam and the metallic fixture used to load it, reducing the risk of specimen failing by delamination. Bonding of the specimen to the rigid plates can be achieved by adhesive bonding.

2.2.8 Hydrostatic Compression

Foams can deform by hydrostatic loading therefore multiaxial and hydrostatic tests can provide with information about the material behaviour under complex loading regimes. Deshpande and Fleck [53] investigated PVC foams under multiaxial loading. The apparatus consisted of a pressure cell with hydraulic fluid as the pressurising medium and a piston for the application of axial force. The specimens were encased in a rubber membrane and sealed to achieve satisfactory isolation at pressures in excess of 2 MPa.

Marau et al, covered the free surface of specimens with a thin film and dipped it into a fluid. However this would result in the development of shear stresses on the surface and also a buckling effect of the film surface. The general behaviour of the film is a factor that might affect the derived data (Figure 2-12). [54]

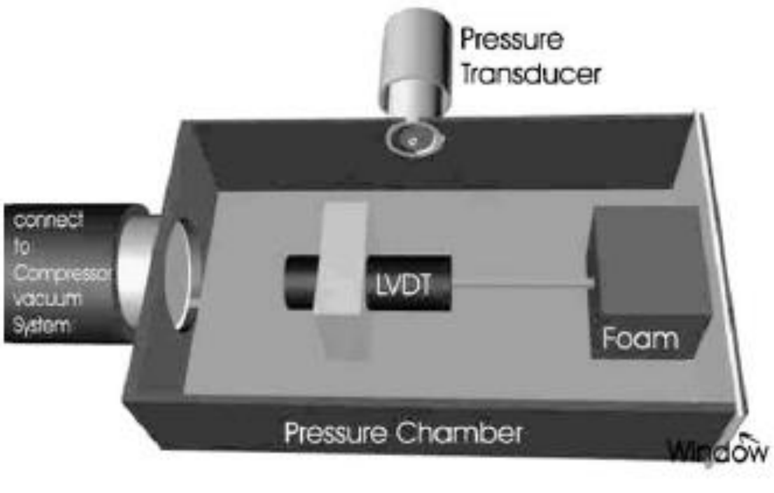

Figure 2-12 Hydrostatic compression apparatus. [54]

2.2.9 Split Hopkinson Bar

The use of the split Hopkinson bar is a way of obtaining a strain stress curve for a material sample at a high strain rate. A typical SHPB consists of two long bars (input and output) and an impactor often called incident bar. The bars are designed to only deform elastically during testing. The specimen is placed in between the input and output bar (Figure 2-13). The free end of the input bar is impacted by a projectile (incident bar) of the same diameter and material. The impact initiates an elastic stress wave that propagates through the input bar to the specimen. Part of the input wave is reflected at the interface between input bar and specimen and another part goes through the specimen and propagates into the output bar. A diagram of a typical (SHPB) wave propagation is shown in (Figure 2-14). [55], [56]

More robust setups include two strain gauges in the first bar (incident bar) allowing longer pulses, a strain gauge at the output bar (measuring the transmitted wave) and high speed cameras that allow the combination of wave analysis and optical data. High speed optical means can assist in verifying and compliment the results of the wave analysis. [30]

High speed photography is commonly used in combination to split Hopkinson setups to ensure that the material deformed in a uniform manner and to identify and correlate the mechanisms of deformation to the material response. Displacements and strains can be obtained via high speed photography while failure modes and damage evolution, can be recorded and correlated with the stress curve. However the number of data points that can be obtained via photography is limited by the available frame rate. The quality of images is subjected to the frame resolution. [57-59]

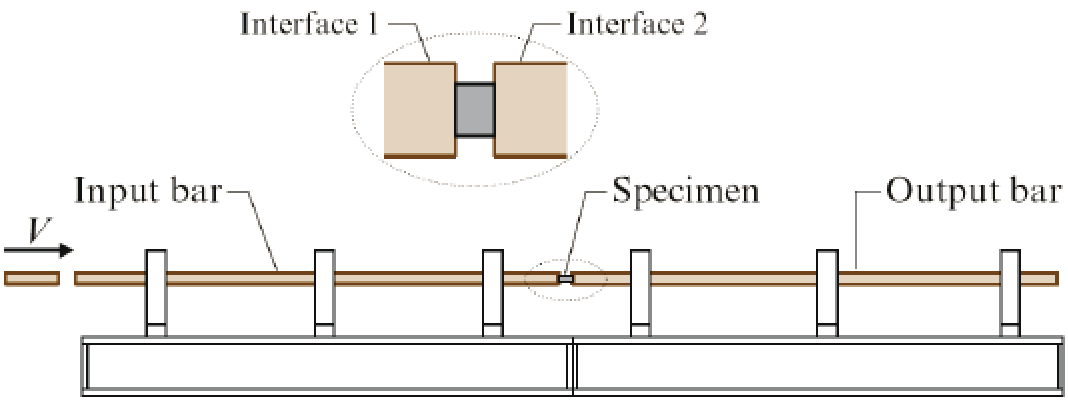

Figure 2-13 Schematic of a basic split Hopkinson bar apparatus. [60]

Strain gauges are used to measure the input, output and reflected waves. Ideally the gauges and bar lengths are such that the waves do not overlap. However certain setups with shorter bars might result in overlapping waves. Wave separation routine is usually used during analysis with two sets of gauges on the input bars. [55] [56]

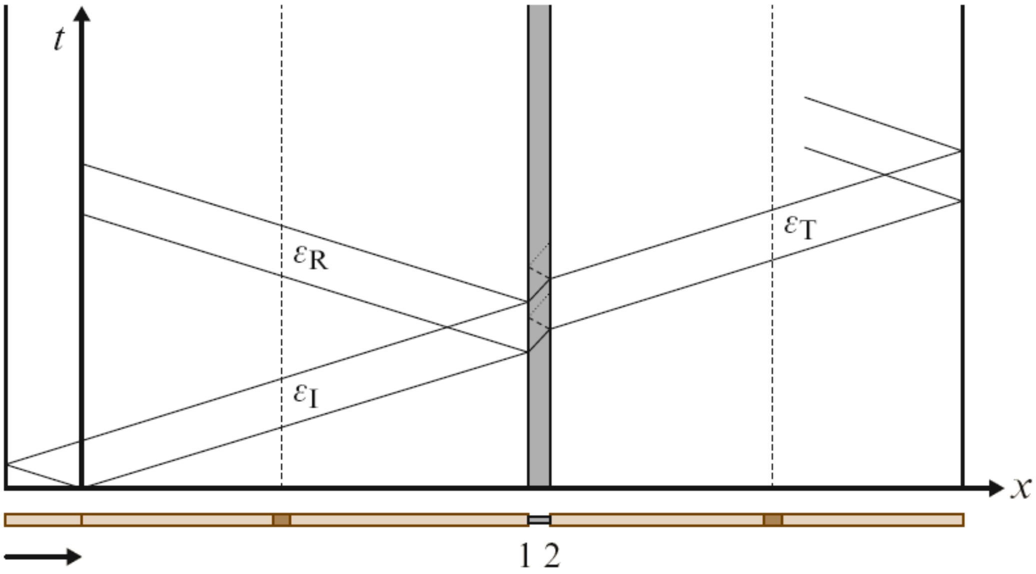

Figure 2-14. Langrangian diagram of a typical SHPB wave propagation. [60]

The signals from strain gauges were recorded using a Wheatstone bridge and an amplifier inputted in commercial software (labview). The bars were calibrated quasi statically using a conventional electromechanically driven crosshead device.

Assuming the stress wave propagates through the bars as one dimensional elastic wave. The strain of the bars is known through the strain gauges and Young's modulus is known for the material of the bars. The stresses in the bars and the normal forces at the interface between the specimen and the input bar are given by analysis [60], [61]:

$$\dot{\varepsilon} = \frac{d\varepsilon}{dt} = \frac{V_1(t) - V_2(t)}{L} \qquad (2\text{-}1)$$

Where V_1, V_2 are the velocities at the interface between specimen and bars, L is the length of the specimen, ε is strain, t is time and $\dot{\varepsilon}$ is strain rate.

We can express the velocities as a function of strains in the strain gauges (C is wave velocity, C_0 is wave velocity in the bars, U_p is velocity of particles within the rod, ρ is density).

$$\sigma = \rho U_p C \qquad (2\text{-}2)$$

$$\frac{\sigma}{E} = \varepsilon \qquad (2\text{-}3)$$

$$C = \sqrt{\frac{E}{\rho}} \qquad (2\text{-}4)$$

Substituting E of eq. (2-4) and σ of (2-2) in (2-3)

$$C\varepsilon = U_p \qquad (2\text{-}5)$$

At the interfaces we have

$$1 \rightarrow V_1 = C_0 \varepsilon_I \,(\text{at } t = 0) \tag{2-6}$$

$$2 \rightarrow V_2 = C_0 \varepsilon_T \tag{2-7}$$

At t>0, V_1 is decreased because of the reflected wave. Thus

$$V_1 = C_0 \left(\varepsilon_I - \varepsilon_R \right) \tag{2-8}$$

Where $\varepsilon_I, \varepsilon_R, \varepsilon_T$ are the incident, reflected and transmitted pulses respectively defined as in (Figure 2-14).

By substitution we have

$$\frac{d\varepsilon}{dt} = \frac{C_0 \left(\varepsilon_I - \varepsilon_R \right) - C_0 \varepsilon_T}{L} \tag{2-9}$$

Thus

$$\dot{\varepsilon}(t) = \frac{C_0 [\left(\varepsilon_I - \varepsilon_R \right) - \varepsilon_T]}{L} \tag{2-10}$$

The strain is found by integrating the strain rate from 0 to t:

$$\varepsilon(t) = \frac{C_0}{L} \int_0^t \left[\varepsilon_I(t) - \varepsilon_R(t) - \varepsilon_T(t) \right] dt \tag{2-11}$$

In order to obtain the stress in the specimen we assume equilibrium

$$\sigma = \frac{P_1(t) + P_2(t)}{2A} \tag{2-12}$$

Where $P_1(t)$ and $P_2(t)$ are the forces acting on the two interfaces 1 and 2. These forces are

$$P_1 = E_o \left(\varepsilon_I + \varepsilon_R \right) A_o \tag{2-13}$$

$$P_2 = E_o \left(\varepsilon_T \right) A_o \tag{2-14}$$

$$\sigma = \frac{A_0 E_0}{2A}[\varepsilon_I(t) + \varepsilon_R(t) + \varepsilon_T(t)] \tag{2-15}$$

E_0 is the elastic modulus of the bars A_0 is the area of the cross section

For equilibrium

$$P_1(t) = P_2(t) \text{ and } \varepsilon_I + \varepsilon_R = \varepsilon_T \tag{2-16}$$

$$\sigma(t) = E_0 \frac{A_0}{A}\varepsilon_T(t) \tag{2-17}$$

$$\dot{\varepsilon}(t) = -\frac{2C_0}{L}\varepsilon_R \tag{2-18}$$

$$\varepsilon(t) = -\frac{2C_0}{L}\int_0^t \varepsilon_R \, dt \tag{2-19}$$

Even though a lot can be found about aluminium foams at high strain rates not much is written on the impact performance of Titanium foams. The main scope in literature is quasistatic experiments done in order to examine the suitability of Titanium foams for bone implants. However some high rate tests can be found on sintered powders. [50]

2.2.10 Taylor Impact

The papers of Taylor [62], Carrigton and Gayler [63] and Whiffin [64] describe the method called Taylor impact experiment. A cylindrical specimen is impacted at a high velocity against a rigid anvil. The specimens deform plastically over a segment forming a cone towards the impacted end. (Figure 2-15)

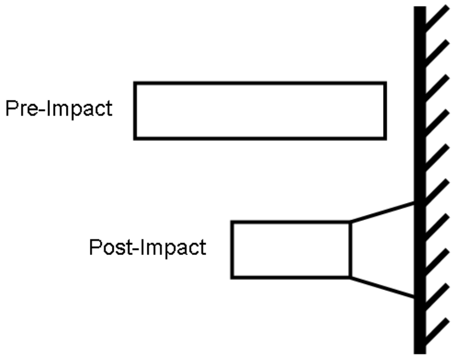

Figure 2-15 Classic Taylor impact experiment

The analysis is based on the assumption that the materials are either rigid or perfectly plastic. One dimensional analysis is to determine the material's dynamic yield stress by measuring dimensions before and after the impact. Various methods are currently used for determining the dynamic characteristics of materials. However the Taylor impact tests are widely used as validation of finite element material models for rate dependent materials due to combinations of stress states. It is also used to exhibit anisotropy at textured materials. [65]

More elaborate setups may include the combination of high speed photography or X-ray tomography performed on samples prior or after tests in order to assist in material models validation. [66-68]

2.3 **Overview of modelling strategies for metal foams**

There are a number of analytical and numerical modelling strategies used to investigate and capture the mechanical properties of porous Titanium. In this section these methods are briefly discussed.

Gibson and Ashby [69], investigated the structure of cellular materials such as honeycombs, metallic and polymer foams and developed relationships between the macroscopic behaviour of these foam materials and the solid (parent) material of the cell walls. By modelling these structures as a repeating array of unit cells they derived scaling laws to predict the mechanical response of these materials under various loading conditions. For example, Gibson & Ashby used the geometric properties of the cell to show a relation between the cell shape and dimensions and the relative density (i.e. the density of the cellular material divided by the density of the raw solid material from which the cell walls are made). By using the cell edge-length (*l*) and the cell wall thickness (*t*), where *t*<<*l* (i.e. the relative density of the foam is small), they developed the following equation for all closed-cell foams with faces of side *l* and uniform thickness *t*:

$$\frac{\rho_f}{\rho_s} = C\frac{t}{l}, \qquad (2\text{-}19)$$

where ρ_f and ρ_s are the densities of the foam and cell-wall material, respectively, and C is a numerical constant that depends on the details of the cell shape. Once the properties are calculated in terms of t and l and converted to the relative density using equation (2-19), a single numerical constant C remains which is determined by an experimental measurement and calibrating the results for all densities.

The development of these scaling laws can be found in [70] where unit cell geometries were idealised to resemble the cellular microstructure. The macroscopic behaviour of the material as a whole was then explained by extrapolating the deformation of the unit cell and developing theoretical equations which relate the mechanical behaviours, such as strength and stiffness, to the relative foam density. An example of such equations is a simple power law model for Young's modulus of foam materials, described in (2-20), where E_f and E_s are the stiffness of the foam and cell wall material respectively, ρ_f and ρ_s are the densities of the foam and cell-wall material and n is a numerical constant which differs depending on whether the foam is open or closed-cell.

$$\frac{E_f}{E_s} = \left(\frac{\rho_f}{\rho_s}\right)^n \tag{2-20}$$

This type of models is based on analysing a simplified geometry that is considered as a representative unit cell. The assumptions made in these models are that the walls are thin or that the porosity is above ~70 % and that the unit cell is representative to the whole structure and therefore is without defects. One of the simplest structural models is that of the 2D honeycomb with a hexagonal unit cell. It is used to approximate more complicated solids.

To model 3D open cell materials Gibson and Ashby proposed a unit cell in the shape of hexahedral with extended vertical beams in the middle of edges (Figure 2-16) in addition to semi empirical relations for scaling the properties of foams to those of the bulk material, depending on the relative density of the foam. Nevertheless, the honeycomb model gives unrealistic predictions for materials with porosity less than 20 %. The 3D open unit cell can provide with better predictions but it is designed for high porosity foams. The assumptions made and the unit cell shape provides space for improvement as for different foams these assumptions are unsuitable.

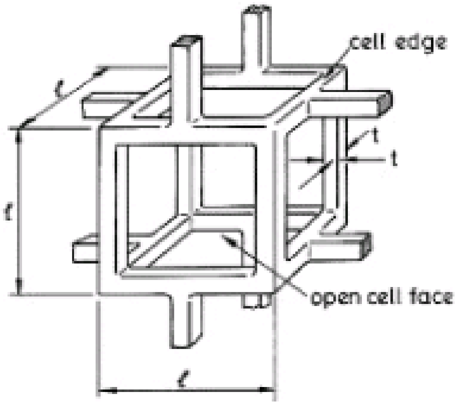

Figure 2-16 Gibson Ashby representative cell. [71]

2.3.1 Mori –Tanaka

The Mori Tanaka [72] method was originally intended for composites with random inclusions of any shape. In the case of foam, the pores are treated as inclusions with zero stiffness. This method was developed for low volume ratios but it has been used for porosities up to 50 %. The basic assumption of this method is that the average strain in the pores can be approximated by that of a single closed pore in the matrix subjected to the average matrix strain.

Using this approach and assuming the absence of any internal pressure within the pores the expression of the effective bulk modulus is a function of the porosity.

2.3.2 Homogenization method

S. Demiray et al, used a strain energy homogenisation procedure where a representative volume element of a foam (with a given microstructure) and the volume element of the homogeneous medium have equal average strain energy density (for the same macroscopic deformation). [73]

2.3.3 Constitutive modelling of metal foams

Various authors modified the theory for fully dense materials in order to account for the effect of porosity on the yield criterion and strain hardening law [74]. Foams can yield under both hydrostatic and deviatoric stresses. The criteria for foam yield must include terms to account for the effect of mean stress. [75]

The produced yield surface is often of elliptical shape in mean and deviatoric stress space with a pressure sensitivity coefficient obtained experimentally [76] to define the aspect ratio of the ellipse [46].

Gibson and Ashby, used a structural model to define the Yield stress and the beginning of the plateau (high porosity foams), by scaling the yield stress of the bulk material and the relative density. The assumption is that the plateau initiates when the moment at the joints exceeds the plastic moment limit of the material of the beams (Figure 2-17).

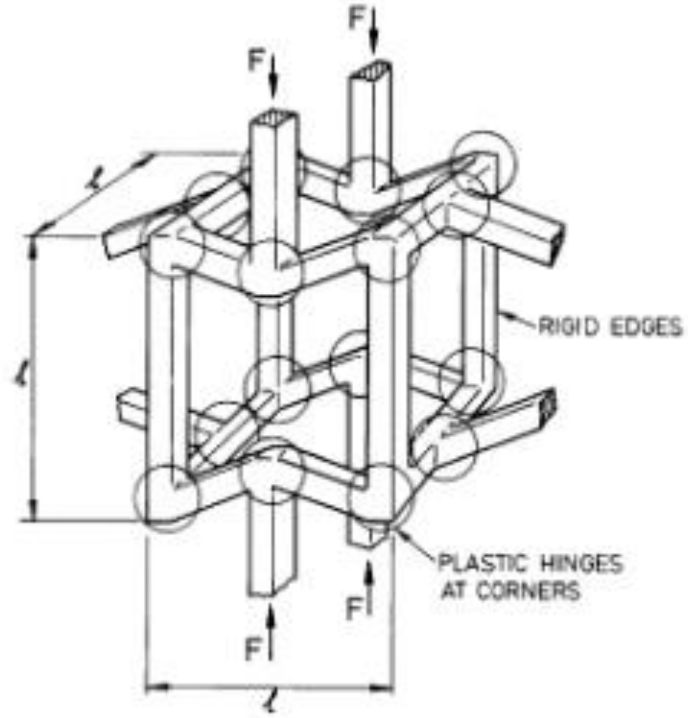

Figure 2-17 Yield stress for the Gibson Ashby representative cell. [71]

2.4 **Motivation**

2.4.1 Experimental

Powder sintering routes allow production of cellular solids [46] made from Ti and Ti alloys [77-79]. These materials are of interest to the aerospace and defence industry due to their good dynamic specific energy absorption, and attract the attention of the bio-medical industry due to good mechanical properties combined with biocompatibility. While the static and dynamic mechanical response of Ti and Ti alloys have been investigated by many authors (see for example [47, 80]), less work exists on the response of Ti and Ti alloy foams. Several authors conducted quasi-static compression, tension and bending tests experiments on open-cell [51, 81] and closed-cell [48] Ti foams manufactured by the space-holder method, which consists in compacting and sintering a mixture of Ti powder and a polymeric space-holder in order to obtain pores of controllable size. Experiments revealed that the foams can be anisotropic as a consequence of the compaction process, and that the mechanical properties of these foams were similar to those of cancellous and cortical bone, for the lower and higher relative densities, respectively.

Tuncer and Arslan [82] tested in compression Ti foams of relative density $\bar{\rho} = 0.2 - 0.7$, produced by optimizing the space-holder method. The materials were deformed at low and medium strain rates ($10^{-3} - 6 \cdot 10^{2}\ \mathrm{s}^{-1}$) and the foams were found to be mildly strain rate sensitive in this range.

Thelen et al. [83] worked with sintered foams obtained from both commercially pure Ti and TiAl6V4 powders. Compressed argon gas was used as a foaming agent to obtain relative densities in the range $\bar{\rho} = 0.5 - 0.8$. Specimens were subjected to quasi-static mechanical loading in order to determine their elastic properties and the variation of these with the foam relative density. It was found that several analytical models (e.g. Mori and Tanaka [72], Ashby and Gibson [84]) were able to predict accurately the foam stiffness.

The fragmented existing experimental studies suggest that Ti foams can be mildly sensitive to strain rate when loaded in compression. This is in contrast with the results reported by other authors on different metallic foams, see for example Deshpande and Fleck [85], [86] on aluminium foams; these authors tested aluminium foams of low relative density ($\bar{\rho} = 0.1$) and found that the compressive response was strain rate insensitive.

In this study, we focus on the compressive properties of pure Ti foams produced using a powder metallurgy process [87], and the measured responses are compared with those of Ti powder sintered under similar conditions to the foams. In order to understand the dependence of the material response on the relative density and the imposed strain rate, foams with density in the range 1577-2478 Kgm^{-3} ($\bar{\rho} = 0.35 - 0.55$) are tested in compression at strain rates ranging from 10^{-2} to $2x10^{3}$ s^{-1}, and results are compared with those obtained for sintered Ti powders of relative density 4100 Kgm^{-3} ($\bar{\rho} = 0.9$).

Figure 2-18 compares the range of relative densities and strain rates for Ti foams found in literature and the range that is examined throughout this work. The foams in literature were manufactured by a variety of processing methods. [7, 82, 88-91]

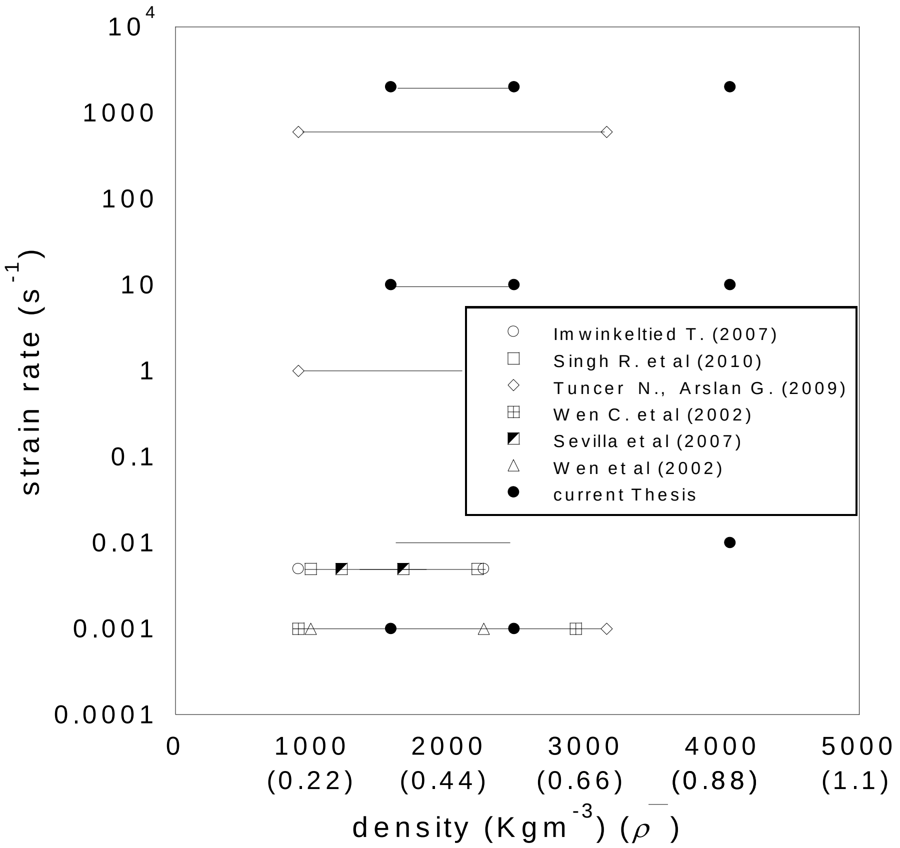

Figure 2-18 Comparison of the range in relative densities and strain rates of Ti foams (manufactured by a variety of methods) found in literature and the foams in this study.

Data on mechanical properties of foams for different densities are fitted to power laws using the least squares method. The least squares method minimizes the square of the error between the original data and the values predicted by the equation. The Pearson's correlation coefficient (R) is used to indicate how well the calculated curve fits the data points. [92]

2.4.2 Modelling

Various authors have investigated cellular materials for use in medical implants [93, 94] [95], [96]. Methods such as powder sintering in combination with space holder techniques are often used to produce metallic foams tailored to mechanical requirements of porous bone substitutes [10, 97]. The produced cellular structures are commonly characterised experimentally to provide information towards optimisation and ensure compliance to requirements. [98, 99], [100, 101]

The geometries of open cell irregular foams are usually complex and difficult to create or replicate for finite element analysis. Some commercial software packages are able to reproduce foam geometries using x-ray micro tomography (XMT) scans [102] but these are usually expensive and tomography equipment is not always accessible. This study is focused in virtually generating realistic foam geometries with desirable microstructural characteristics. The foam features are statistically controlled and their effect to the macroscopic response of the structure is investigated using FE modelling. Results are compared with experimental data [101] on Titanium foams manufactured for use as biomedical implants. Yield surfaces are produced for different densities. The aim is to provide with a method for virtually generating, and examining foams with statistically controlled microstructural features.

Shen et al [103] simulated structures of foams based on a method of growth of pressurised pores. Pores were represented by spheres that grew to achieve desirable density for foams up to 15 % of porosity. The results present reasonable agreement with experimental data for low porosity foams. The pores result from spheres or combinations of spheroids and therefore the method does not take in to account the irregularity in the pore shapes that may result to stress concentrations and complex contact interactions.

Borovinsek, et al, [104] modelled high porosity lattice structures 88-97 % based on the Voronoi tessellations. The foams were subjected to quasi static and dynamic loading. The effect of irregularity to the material response was studied. The study was purely numerical.

Vesenjak et al [105] modelled aluminium alloy and polymer open cell regular foam structure (relative density of 0.16-0.37) and examined the influence of a viscous fluid within the foam, in failure and energy absorption. The structure was made by a network of interconnecting cylinders at regular positions through the material.

Demiray [73, 106] modelled open cell foam consisting of a body- centred cubic package of tetrakaidecahedral cells. The yield surface was formed by following radial loading paths in the macroscopic space. The study concludes that the microstructure has a significant effect on the hardening effects of the foam. Structures of this type tend to be of high porosity but limited information is given regarding porosity and no comparison to experimental data.

Hohe and Becker [106], studied the mechanical behaviour of two dimensional low density honeycombs and foams and proposed a homogenisation strategy based on strain energy.

Singh et al, [7] tested Ti foams of porosities of 51-78 % and modelled the structure using FE methods. The geometry of the foam was obtained using X-ray micro tomography from which the structure was reconstructed and directly produced mesh (5000000 elements) using commercial software (Simpleware). The methods and software used were expensive and FE predictions had significant difference (up to 40 %) from the tested samples.

Gibson-Ashby [69] developed a widely used model for porous materials. The model was developed based on a hexahedral lattice cell with extended beams in the middle of the edges which assumes very high porosity. Fleck et al, [46, 107] developed constitutive laws for bonded metal powders that mainly apply for relative densities of 64-90 % of the fully dense material. The yield surface is obtained from the plastic dissipation at necks between the particles.

However there is currently limited work on continuum models for medium porosity foams that account for the irregularity of the foam as to the type, shape and orientation of pores within the structure. This work is focused in capturing and investigating the microstructural characteristics that affect the macroscopic response of highly irregular foams. The method for virtually generating and modelling foam geometries can potentially be used in optimising foams for application requirements.

3 Experimental characterisation of Ti foams

Summary

Sintered titanium powder and titanium foams of relative density ranging from 1577-4100 Kgm^{-3} ($\bar{\rho} = 0.35 - 0,9$) were produced by powder metallurgy routes and tested at low, medium and high rates of strain. At all strain rates, the foams deform by plastic collapse of the pores, accompanied by micro-cracking at compressive strains exceeding 0.2. The foams investigated are strain rate sensitive, with both the yield stress and the strain hardening rate increasing with applied strain rate. The strain rate sensitivity is more pronounced for foams of lower relative density.

3.1 **Material manufacturing**

Sintered Ti powders and sintered Ti foams were produced using the process described in [87]. Briefly, titanium powder is mixed with a binder and a chemical foaming agent. The resulting mixture is poured into a mold and heated in order to foster the foaming process; subsequently, the material is de-binded and sintered. During foaming the binder melts and forms a suspension with the Ti particles. The foaming agent then decomposes and generates a gas that expands the suspensions; after foaming, the binder is eliminated by thermal decomposition.

Specimens with different porosity levels are produced by modifying the composition of the mixture. The resulting material is cut into circular cylindrical specimens which are then sintered at high temperature to consolidate the material. Sintered Ti powder specimens were produced by a similar route to that described above, absent the foaming agent and the binder.

3.2 **SEM analysis of the material microstructure**

Scanning electron microscopy (SEM) was used to examine the microstructure of the sintered Ti foams. The surfaces of the examined samples were not subjected to any cutting or polishing in order to not distort the texture resulting from the process [87]. The manufacturing processes used for producing implant materials aim at homogeneity of porosity throughout the sample. The choice of process and foaming agents ensure the consistency in the structure [11, 108, 109]. SEM and XMT performed on foams show agreement in the order of pore sizes between surface and specimen interior [7].

Two levels of porosity are clearly visible in the foam: (i) a macroporosity which results from the foaming process and (ii) a micro-porosity resulting from incomplete consolidation of the Ti powder during sintering, as shown in Figure 3-1. The microstructure of the sintered powders 4100 Kgm^{-3} ($\bar{\rho} = 0.9$) comprised well sintered particles and only small micropores of diameter around 10 µm were observed. On the other hand, all foams 1577-2478 Kgm^{-3} ($\bar{\rho} = 0.35 - 0.55$) displayed macroscopic pores of diameter ranging from 100 to 1400 µm. The micro-porosity was also higher in the foams, due to the effect of the binder and foaming agent on the inter-particle spacing after sintering. Observations are in agreement with literature on foams made by similar processes. [7, 22, 97]

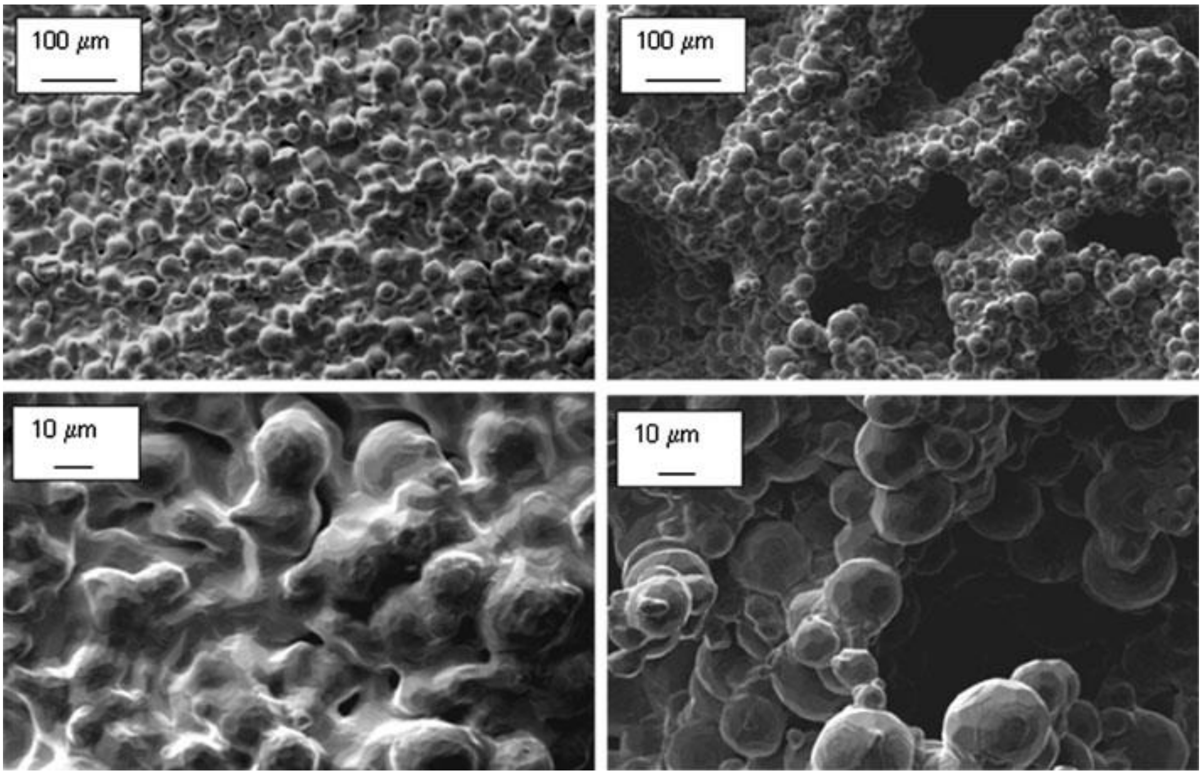

Figure 3-1 SEM images of high relative density 4100 Kgm^{-3} ($\overline{\rho} = 0.91$) (left) and low-density (2027 Kgm^{-3} ($\overline{\rho} = 0.45$) (right) materials at two different magnifications. Micro-pores of diameter around 10 µm are seen in the sintered powder (high density material); larger macro-pores of diameter on the order of 100 µm are observed in the low-density foam. Consolidation (i.e., degree of sintering) is higher for the sintered powder

3.3 X-ray tomography analysis

In order to examine the foams microstructure, X-ray tomography analysis was performed on circular cylinders (5 mm diameter and height) of different relative densities, ranging from 0.35 to 0.55. A 40 W SkyScan (Kartuizersweg 3B, 2550 Kontich, Belgium) X-ray tomographer of spatial resolution of 9µm, source voltage 50 kV and current 800 µA, was used to produce two-dimensional cross-section images

(Figure 3-2) of the foam microstructure, which allowed automated reconstruction of the three-dimensional foam structure (Figure 3-3).

Each specimen was subjected to 183 projections by rotating the sample by an angular step of 1°. The detector was digital of 1280x1024x12 bit resulting to a 1024x1024 pixel images in projections with 16 bit depth in acquisition. [110]

The projections were reconstructed using the Feldkamp algorithm [111] commonly used to reconstruct images from cone beam projections. The commercial software (NRecon) [110] allows for previewed fine tuning of post alignment, ring artefacts reduction and beam hardening correction.

Segmentation was done by a histogram based method. A brightness distribution (gray scale) reveals peaks and valleys that can be used to cluster and segment. This allows for a range of brightness to be used for binary selection between ‘’solid’’ and ‘’space’’. The sum of voxel volume within the intensity range for pores should correspond to the percentage of macroporosity for the specimen of a known density.

Microporosity of about ~10 % in-between the powder particles was not included to the analysis, as micropores and powder particles were very close to the length scale of the tomographic resolution (9 μm). Micropores and powder particles that would blend in voxels would appear to have a lower absorption than fully dense material but higher than ‘’space’’. The foam’s solid structure of powders particles and micropores was taken as a pseudo-solid (foam parent Figure 3-1 left). As a result of the limited resolution and powder particle size (~10 μm) the equipment was unable to capture the roughness of pores on the pore boundaries bellow that order (9 μm). However it was still able to provide an inside as to the irregularity and order of magnitude of macropores.

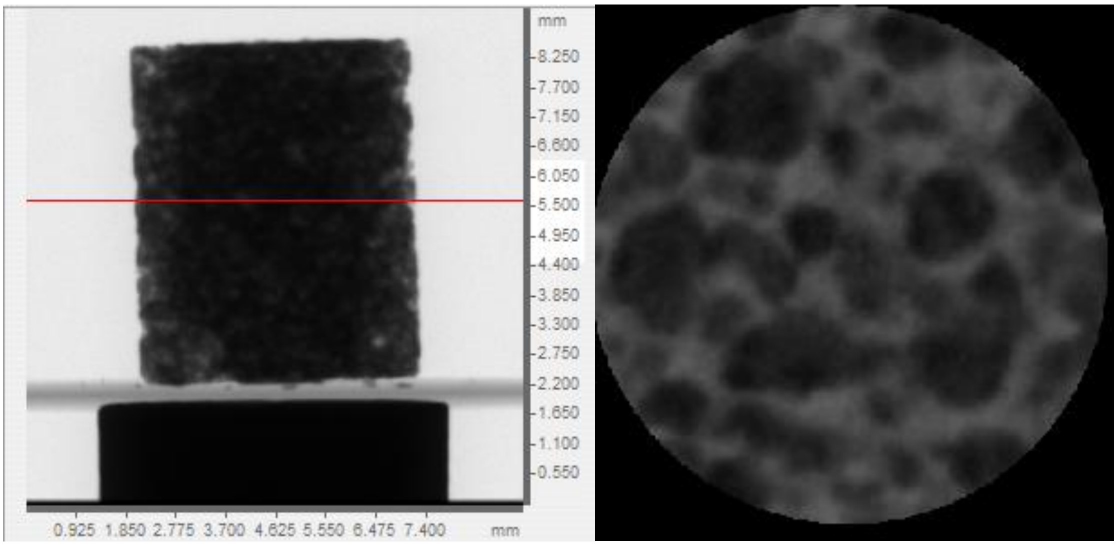

Figure 3-2 XMT images of a Ti foam specimen microstructure in a noninvasive or destructive way.

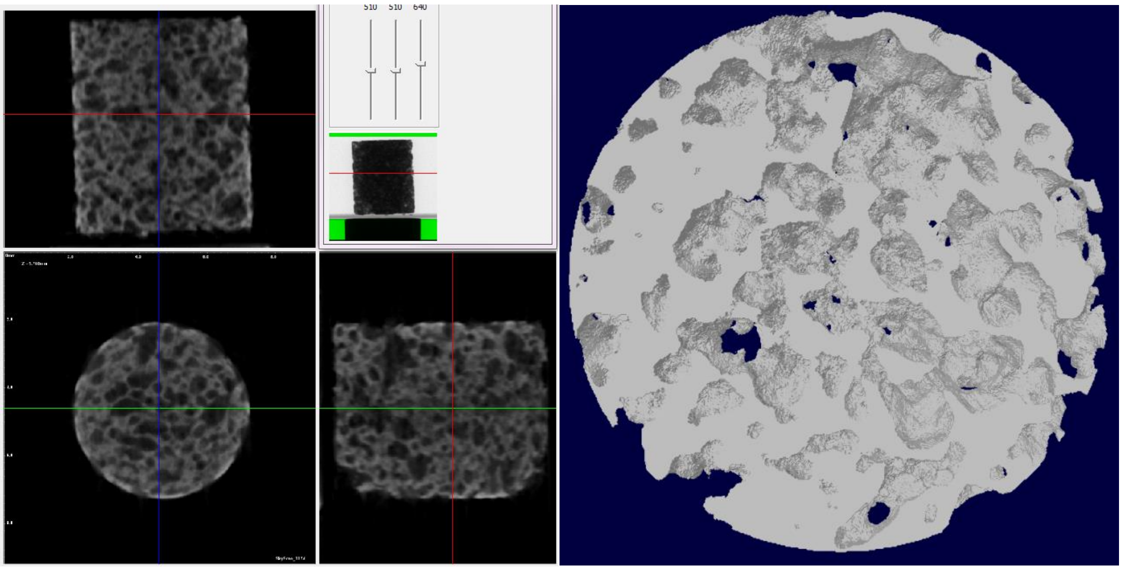

Figure 3-3 3D reconstruction from the XMT images

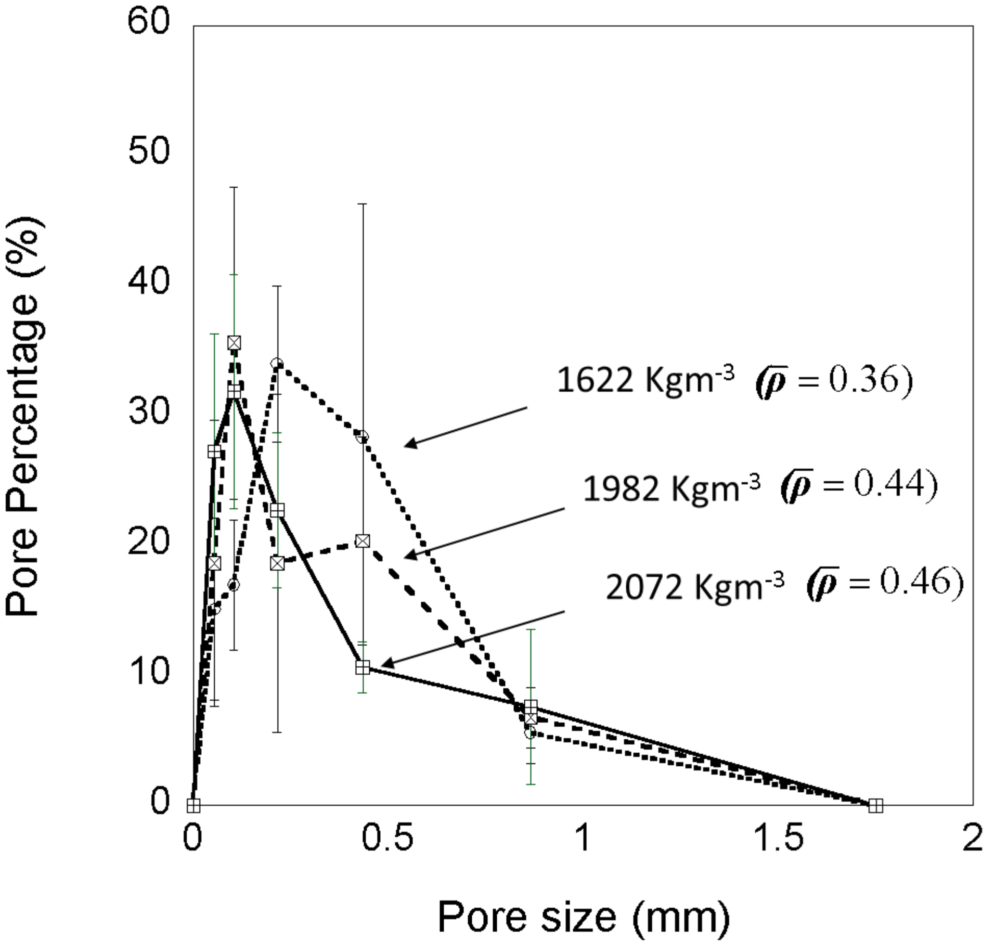

Figure 3-4 Pore size distributions for Ti foams of three different densities. The peak of the distribution occurs at smaller pore diameters as the density increases 1577 Kgm^{-3} ($\bar{\rho} = 0.35$), 1982 Kgm^{-3} ($\bar{\rho} = 0.44$), 2072 Kgm^{-3} ($\bar{\rho} = 0.46$).

For all foam densities, the microstructure comprised a network of sintered particles surrounding a random distribution of pores of irregular shape, with no preferential orientation. X-ray tomographer software (Skyscan CTan) methods were employed to measure the pore size distribution in each sample, as presented in (Figure 3-4) for three different foam densities. The volume of the foam samples was analysed. Pores were defined as ''solid objects'' within the 2D images (based on the chosen pore intensity range during segmentation). Pore diameters were calculated as the diameter of spheres of volume equivalent to the volume of the pores. Foams of higher density are associated with a smaller average pore size, as shown by the different peaks in the three measured pore size distributions.

3.4 Quasi-static uniaxial compression tension and shear

3.4.1 Quasi static Compression

Porous specimens of density 1577-4190 Kgm^{-3} ($\bar{\rho} = 0.35 - 0.93$) were tested in uniaxial compression at a strain rate of 10^{-2} s^{-1}. Preliminary compression experiments revealed that the material response was approximately isotropic. Then, circular cylindrical specimens of diameter 11 mm and height of 13 mm were compressed in the axial direction. Specimens were manufactured in that size and therefore no cutting was required.

A screw driven commercial Housfield machine was used in displacement control to conduct the experiments. The compressive force was measured by a resistive load cell, and the shortening of the sample was measured by a high precision and frequency laser extensometer and was used to calculate the compressive strain. Experiments were interrupted when an axial strain larger than 0.5 was achieved.

An optical system was used to monitor deformation, crack and failure propagation on the surface enabling the correlation of the stress strain points with the specimen status. The cameras were lid by filtered LED lights so that to avoid extensometer and cameras interference. Figure 3-5 shows photographs taken during a quasi-static compression test, at different levels of imposed axial strain. The figure shows that the plastic deformation of the foam is initially uniform, with negligible barrelling. At axial strains larger than 0.2, barrelling of the sample is observed in conjunction with formation of small cracks. These cracks coalesce at high compressive strains to give catastrophic failure of the sample.

Figure 3-6 represents the measured stress versus strain curves for samples of four different densities. For all densities, the material response comprises an initial linear phase followed by a strain hardening response.

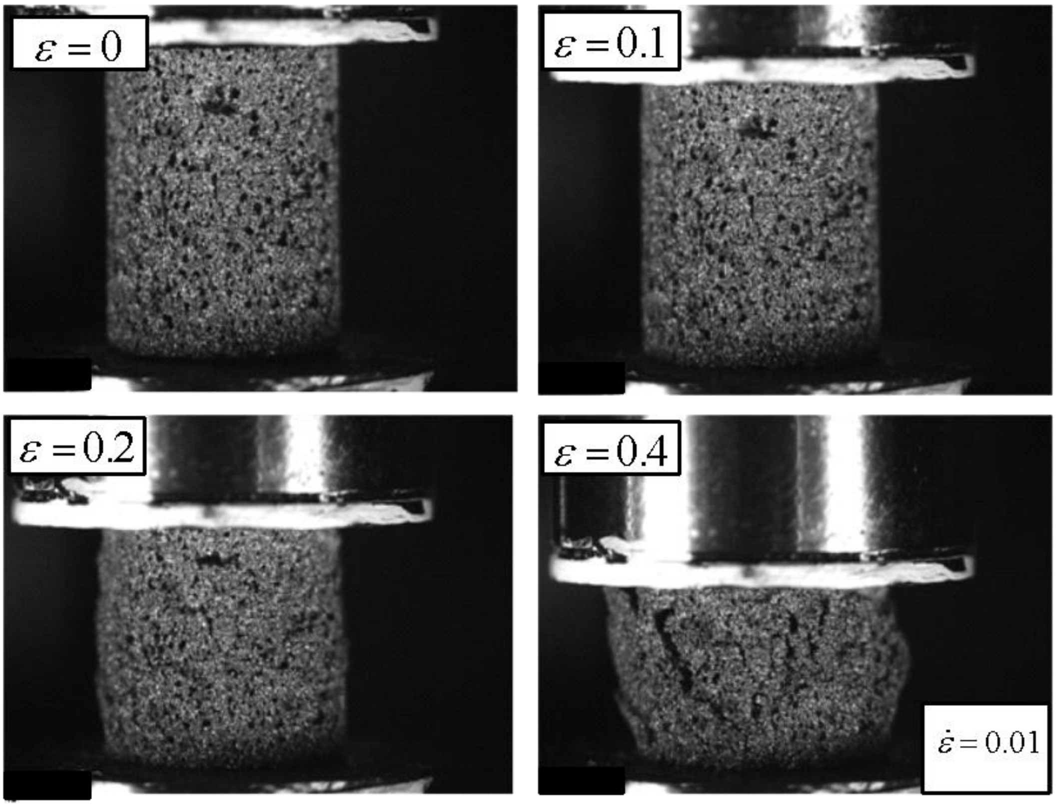

Figure 3-5 Photographs of a foam specimen of density 1667 Kgm^{-3} ($\bar{\rho} = 0.37$) subject to a quasi-static compression experiment. Deformation is initially uniform; micro-cracking intervenes at axial strains higher than 0.2

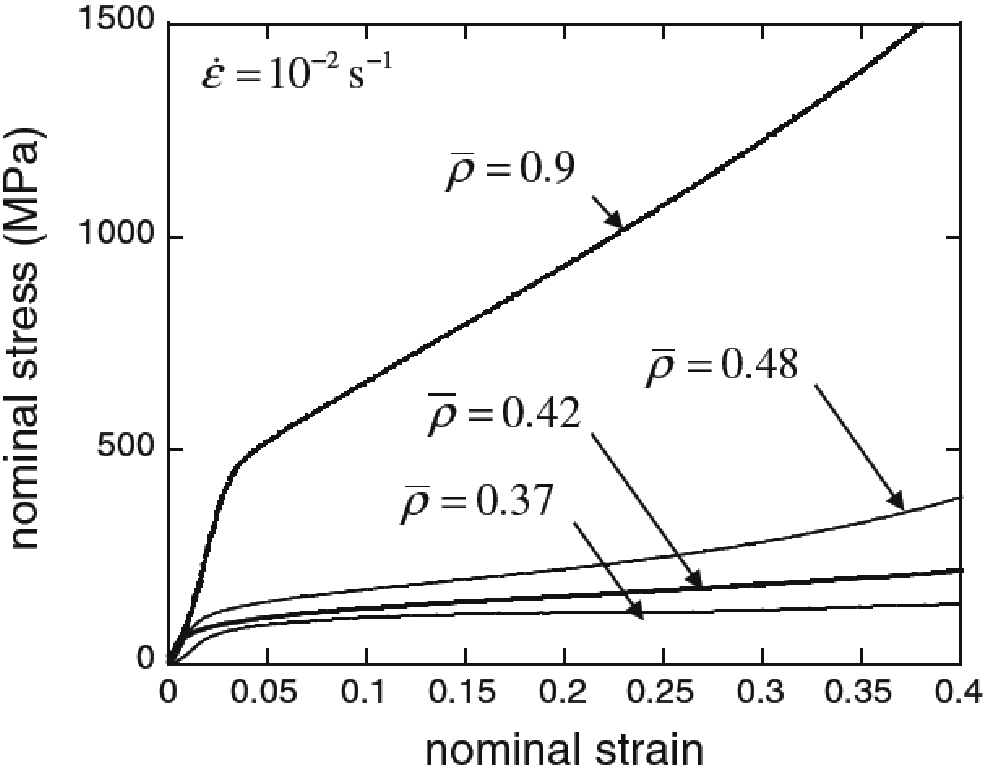

Figure 3-6 Quasi-static compressive response of the Ti foams and sintered Ti powder 1667 Kgm^{-3} ($\bar{\rho} = 0.37$), 1892 Kgm^{-3} ($\bar{\rho} = 0.42$), 2162 Kgm^{-3} ($\bar{\rho} = 0.48$), 4100 Kgm^{-3} ($\bar{\rho} = 0.9$).

The elastic modulus of the material was measured using unloading and reloading foam specimens (Figure 3-7) at a plastic compressive strain of 0.1, and the modulus was found to increase with increasing density. The material yield stress was recorded for each test; this was defined as the flow stress at a nominal compressive plastic strain of 0.2. The strain hardening rate was higher for foams of higher density. Selected compression tests were also repeated on specimens of different dimensions (11 mm diameter and 5 mm height). The measured response was found to be independent of the specimen height.

An in-house developed image correlation software was used to measure transverse deformation of the sample; the ratio of this transverse strain to the imposed compressive axial strain is defined here as the material Poisson's ratio.

Figure 3-8 shows the evolution of this ratio with increasing imposed axial strain, for a range of foam densities. This data are shown for axial strains less than 0.25. Beyond this value of imposed strain, material cracking intervened in the experiments, invalidating Poisson's ratio measurements.

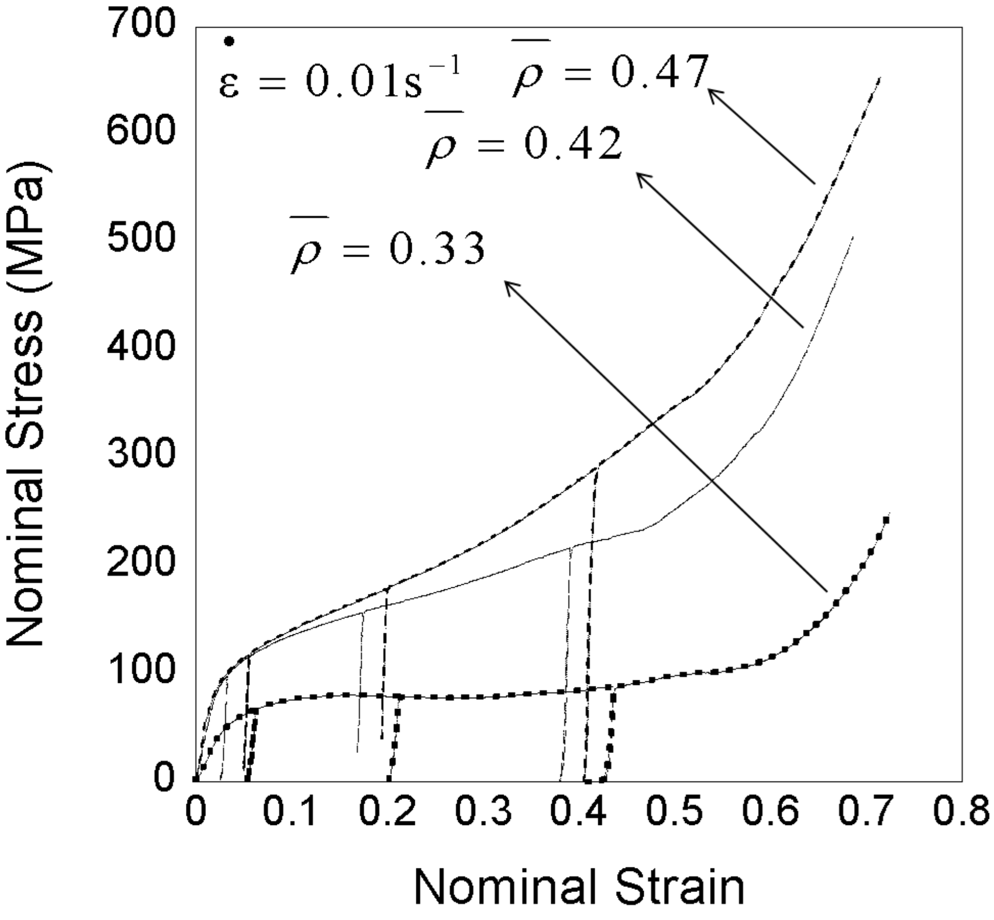

Figure 3-7 Loading and unloading stress strain curves for compression specimens 1512 Kgm^{-3} ($\bar{\rho} = 0.33$), 1892 Kgm^{-3} ($\bar{\rho} = 0.42$), 2117 Kgm^{-3} ($\bar{\rho} = 0.47$).

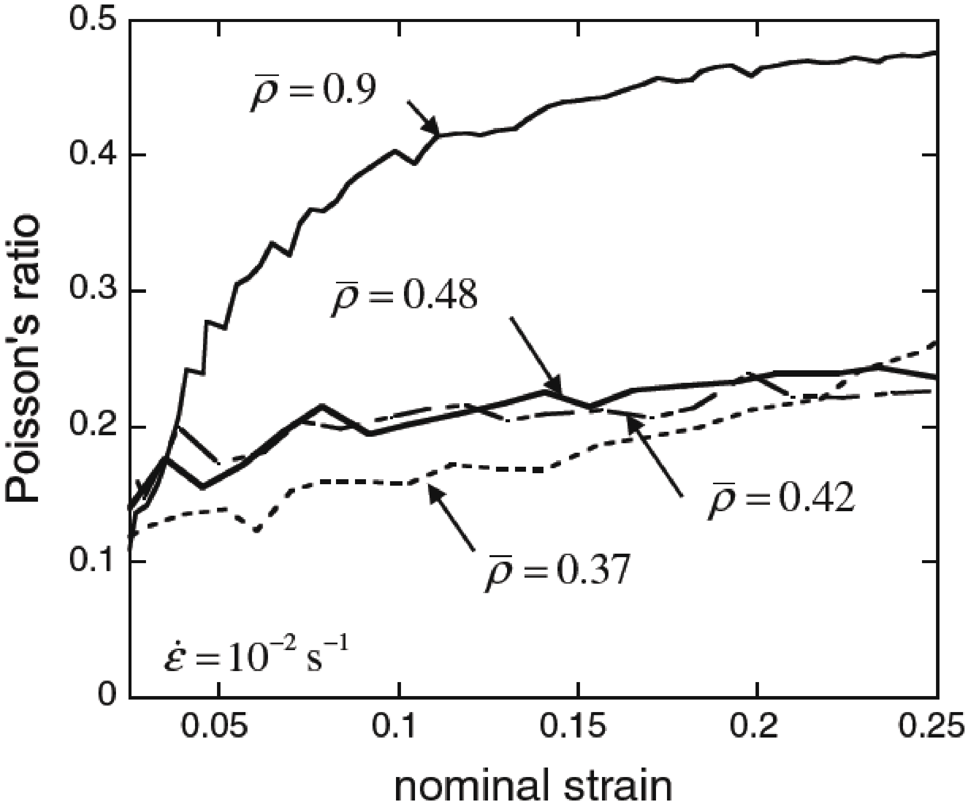

Figure 3-8 Measured Poisson’s ratio as a function of the applied axial strain, for foams of four different densities 4100 Kgm^{-3} ($\bar{\rho} = 0.9$) 2162 Kgm^{-3} ($\bar{\rho} = 0.48$), 1892 Kgm^{-3} ($\bar{\rho} = 0.42$), 1667 Kgm^{-3} ($\bar{\rho} = 0.37$)

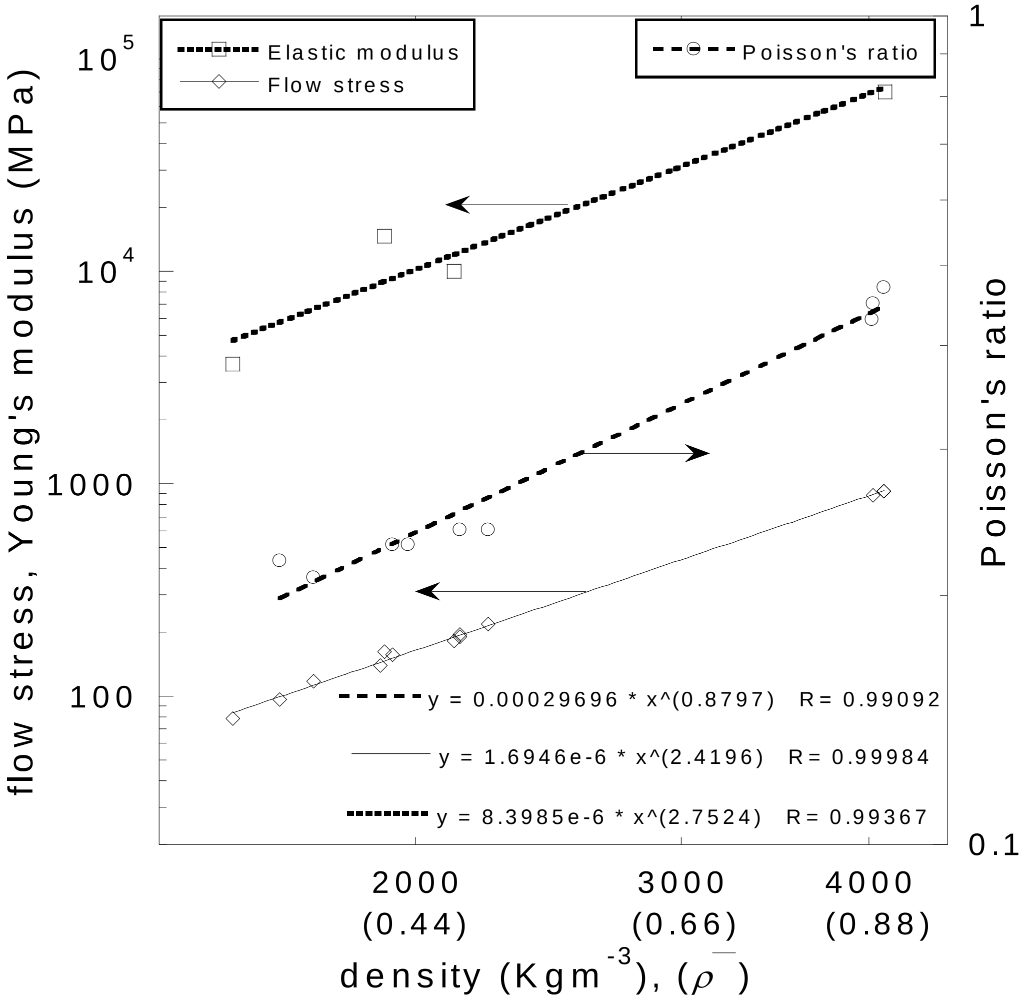

Figure 3-9 Variation of elastic modulus, flow stress (at 0.2 axial plastic strain) and Poisson's ratio (at 0.2 axial plastic strain) as a function of relative density. The graph includes power-law fits of the experimental data.

The initial value of the Poisson ratio (corresponding to elastic axial strains) is in the range 0.1–0.15 for all foam densities; these values are a little bit lower than those measured by other authors [77] by laser ultrasonic probing on foams produced under slightly different processing conditions. As the axial strain increases, the Poisson's ratio also increases at a rate depending on the foam density. For the foams tested, the Poisson's ratio shows a mild increase with strain, attaining a value of 0.2 when the axial strain reaches 0.2; in contrast, for the sintered powders, the increase of Poisson's ratio with axial strain is more pronounced and tends to approach the theoretical limit of 0.5 (for a plastically incompressible material) at large imposed axial strains Figure 3-8.

Figure 3-9 represents the dependence of compressive elastic modulus, yield stress and Poisson's ratio (at an axial strain of 0.2) on the foam relative density; experimental data are accompanied by least-square power-law fits. The exponent of the power laws describing the dependence of Young's modulus and yield stress on relative density are 3.28 and 2.44, respectively (Ashby and Gibson [15] predict coefficients of 2 and 1.5, respectively, for low-density open-cell foams). The Pearson's correlation coefficient (R) is used to indicate how well the calculated curve fits the data. [92]

3.4.2 In situ SEM compression experiments

With the aim of visualizing the microscopic compressive deformation and failure mechanisms for the foams under investigation, cubic specimens of 5 mm side were cut from foams of density 1577-1982 Kgm^{-3} ($\bar{\rho} = 0.35 - 0.44$) and loaded in compression in a SEM. A 5 kN miniature loading rig was used to compress the specimens at a strain rate of 10^{-2} s^{-1}; the tests were periodically interrupted to allow a scan to be taken. Part of the sequence of SEM micrographs produced, is presented in (Figure 3-10) and allows to visualize deformation and failure mechanisms of the foam in uni-axial compression.

It was observed that macro-pores (of diameter on the order of 100 μm) progressively collapsed by flattening along planes perpendicular to the loading direction. At compressive strains exceeding 0.2, micro-cracking was observed, with cracks of length of the order of 50 μm initiating and propagating. Propagation of these micro-cracks occurred both at the sintering necks between powder particles. The observed deformation mechanisms were independent of foam relative density in the range investigated.

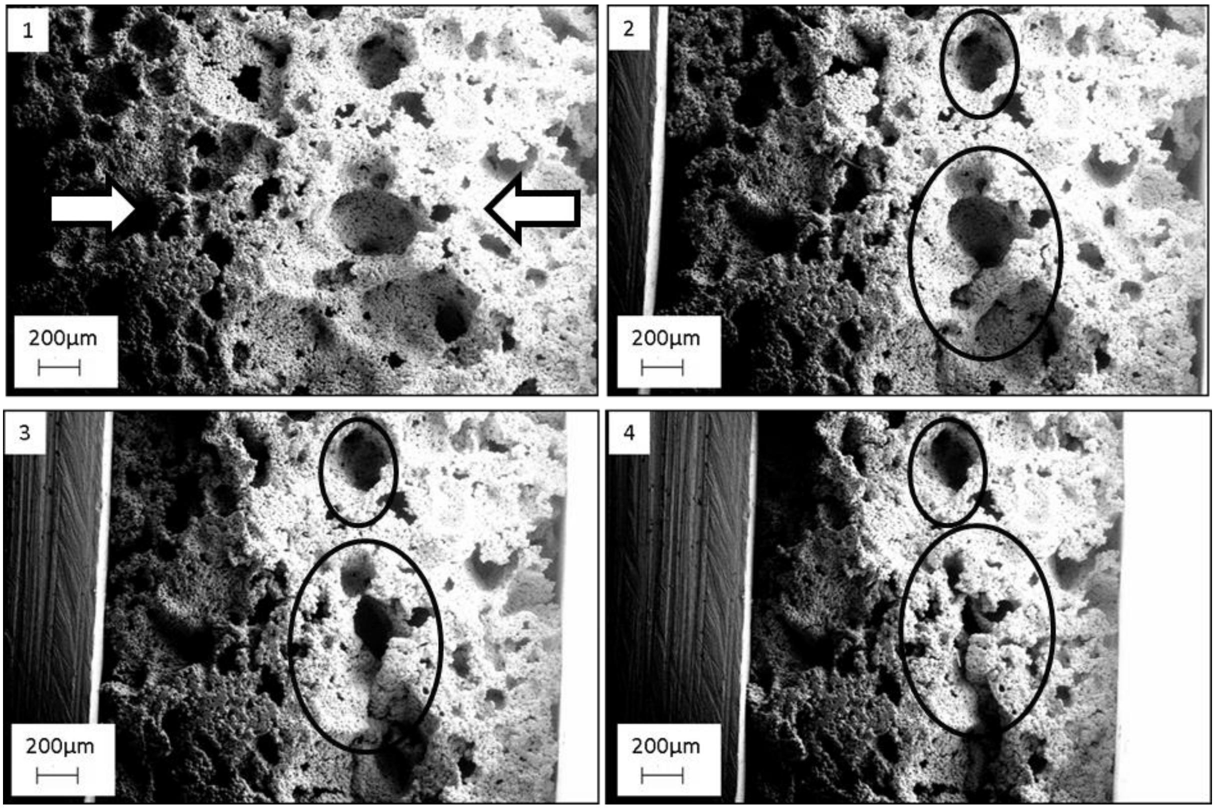

Figure 3-10 Sequence of SEM micrographs of foam under uniaxial compression

3.4.3 Quasi static tension

Quasi static tensile tests were performed for sintered Ti powders 4100 Kgm^{-3} ($\bar{\rho} = 0.9$) at rates of (0.001-0.01 s^{-1}). Dog bone specimens were of gauge length of 8mm and diameter 3 mm (Figure 3-11). Gripping was achieved by using conventional grips with rough surface to increase friction. A screw driven machine in displacement control was used to conduct the experiments. The tensile force was measured by a resistive load cell, and the displacement of the sample was measured by a laser extensometer and a high resolution camera that was used to calculate the tensile strain.

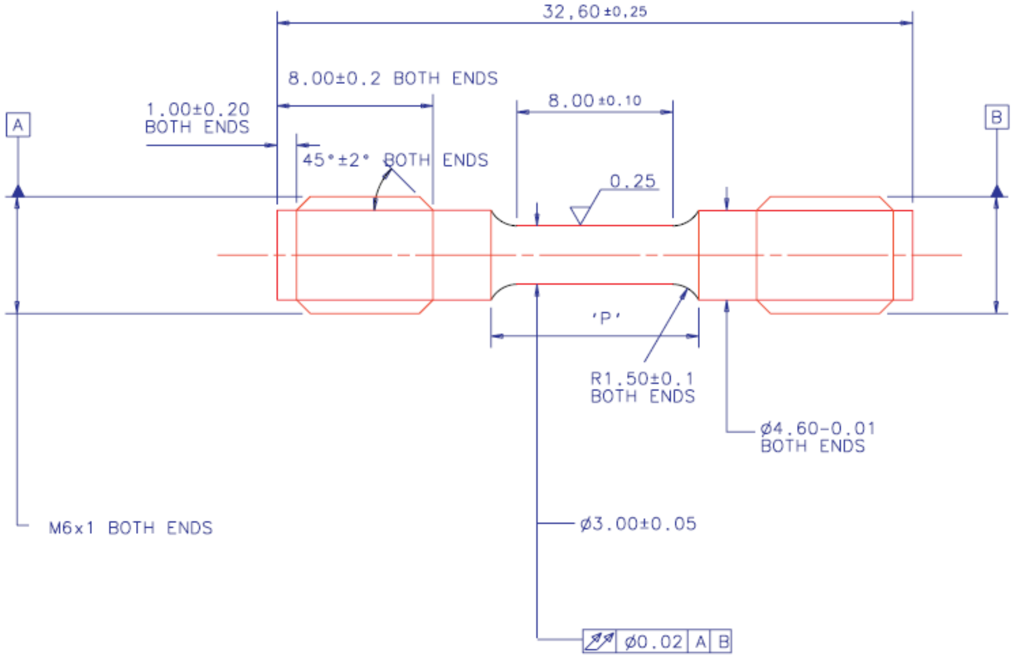

Figure 3-11. Design of tension specimen used for sintered Ti powders 4100 Kgm^{-3} ($\bar{\rho} = 0.9$) at strain rates of 0.001-2500 s^{-1}

Ti foam specimens of 1577 Kgm^{-3} ($\bar{\rho} = 0.35$) were tested in quasi static tension. The specimens were machined from rectangular prismatic foam samples. Tensile tests were limited to one density due to material availability. Flat dog bone specimens of gauge length 8 mm, width of 5 mm (similar to [88]) and shoulder radius of 12 mm (Figure 3-12) were tested using a screw driven machine in displacement control was used to conduct the experiments. Specimens were held using standard rough surfaced grips. The tensile force was measured by a resistive load cell, and the displacement of the sample was measured by a laser extensometer and a high resolution camera that was used to calculate the tensile strain.

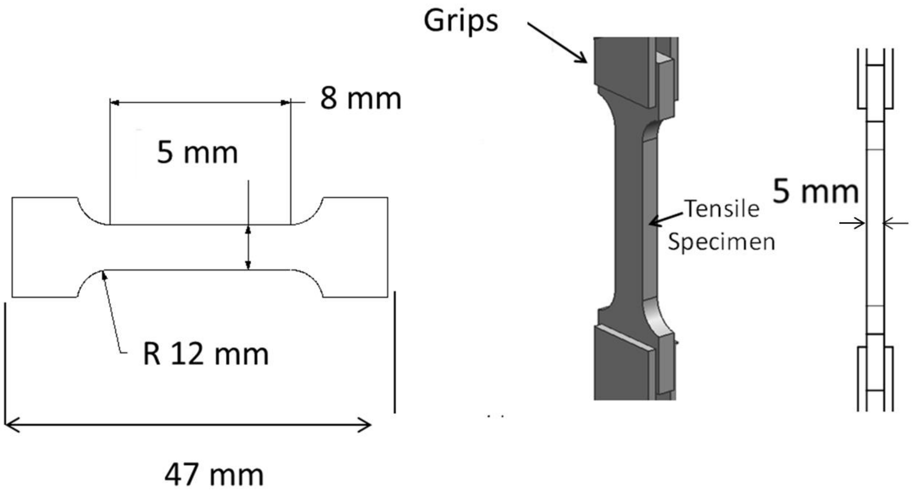

Figure 3-12 Foam tensile specimen.

Failure for low density foams occurred shortly after elastic region for strains less than ε=0.01 (Figure 3-13). Similar behaviour of Ti foams of higher porosity is also found in literature [114]. Elastic modulus was found to increase in tension rather than in compression in agreement with [88].

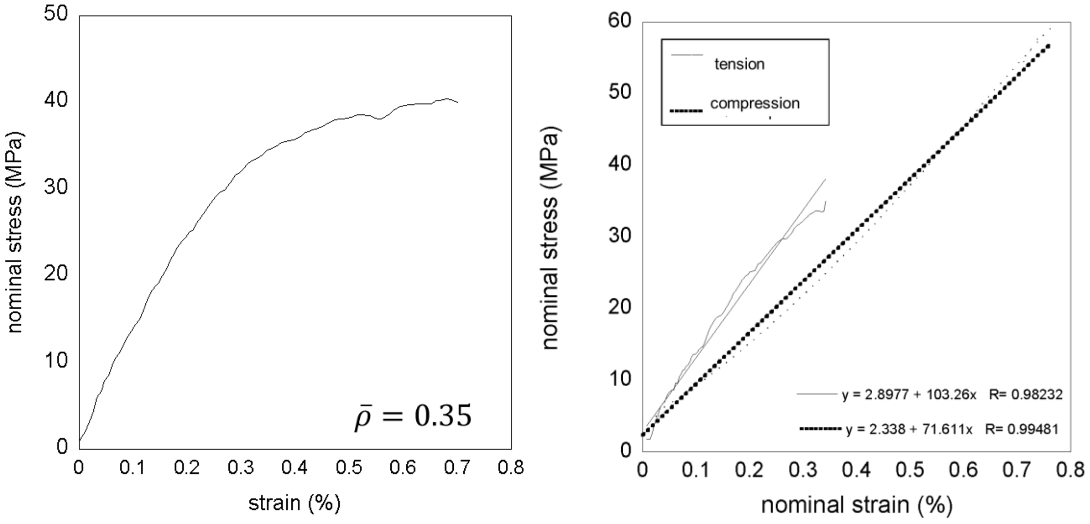

Figure 3-13. Quasi-static tensile response of the Ti foam 1577 kgm^{-3} (left) ($\bar{\rho} = 0.35$) (left) and comparison of the linear part in the response between tensile and compression quasi static test (right).

3.4.4 Quasi static shear

Shear experiments were conducted using prismatic foam specimens with an I-shaped cross-section. Shear deformation occurred only in the web of the I-beam. The specimen geometry was preferred to a prismatic beam of rectangular cross-section as an I-shaped cross-section allows reduction of stresses at the interface between the foam and the metallic fixture used to load it, reducing the risk of specimen failing by delamination. The web of the I-shaped cross-section, representing the gauge section of the specimen, had a height and width of 3 mm, whereas the length was 45 mm to ensure a high depth to height ratio, in order to minimise edge effects. The thickness and width of the I-beam flanges was of 4 mm and 23 mm, respectively. The web was connected to foam flanges by fillets of radius 1 mm. The I-beam was sandwiched between two steel plates. The specimen was bonded to the plates by a structural adhesive. Additionally a step of 2 mm deep and to the length of the specimen was machined on the plates to offer extra support to the adhesive; the plates were connected to a screw-driven test machine by pin joints (Figure 3-14). A screw driven machine in displacement control was used to conduct the experiments. The compressive force was measured by a resistive load cell (Figure 3-15). During the experiment, the test machine reduced the spacing between the pin-joints, therefore applying a compressive force on the steel fixture, resulting in a shear action on the I-shaped foam core. A non-contact laser extensometer and a high resolution camera were employed to record the relative displacement between the two flanges of the I-beam, thereby determining the engineering shear strain (Figure 3-16).

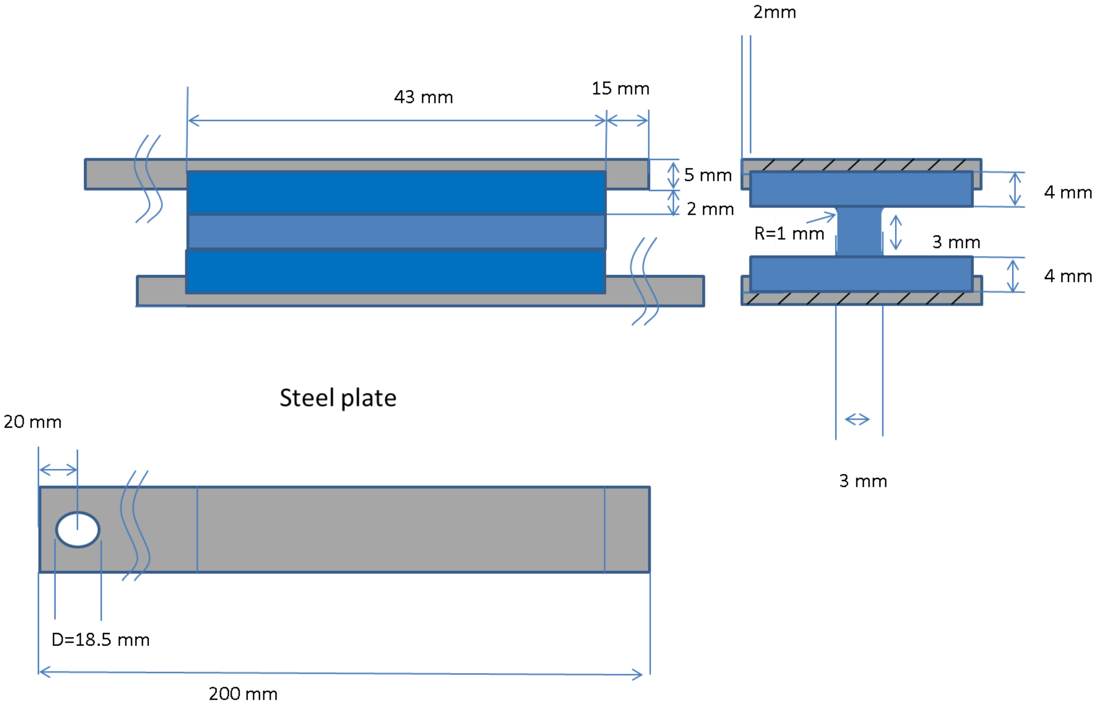

Figure 3-14 Shear specimen.

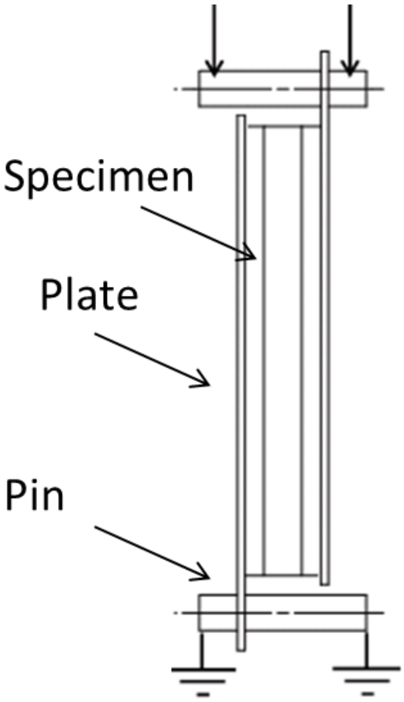

Figure 3-15 Shear fixture arrangement.

Foam behaviour under shear loading consisted of an elastic phase followed by brittle failure (Figure 3-16).

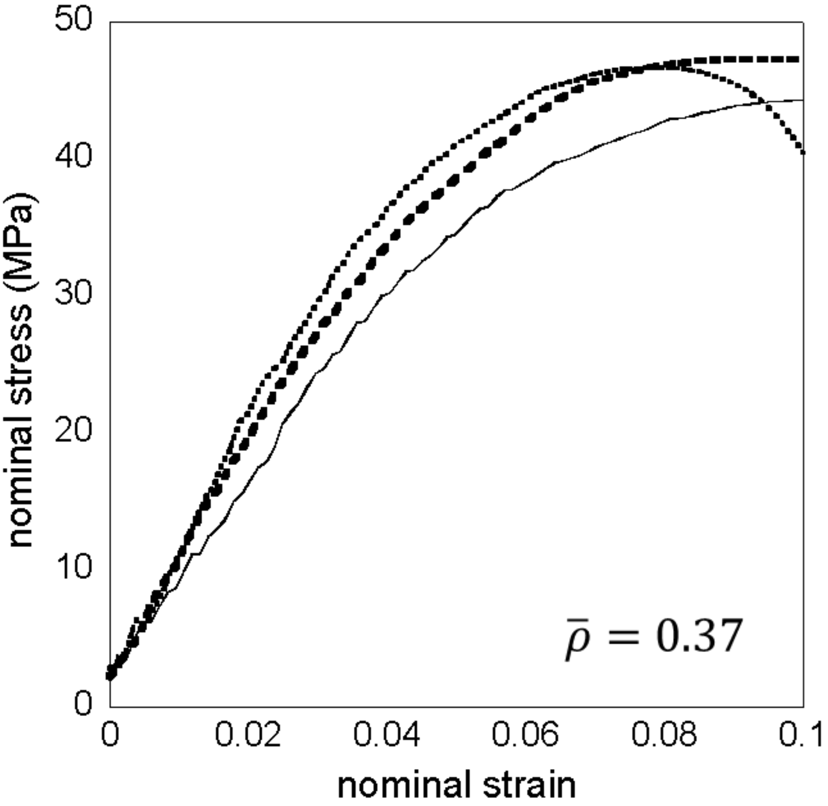

Figure 3-16 Quasi-static shear response of the Ti foams of density 1667 Kgm^{-3} ($\bar{\rho} = 0.37$)

3.5 **Dynamic compression and tension experiments**

In order to measure the dependence of the material response upon the rate of strain, dynamic uniaxial compression and tension tests were performed. Two different loading systems were employed to obtain strain rates of the order of 10 s^{-1} (medium) and 2 x 10^{3} s^{-1} (high), respectively, as detailed below.

3.5.1 Medium rate compression experiments

A hydraulic loading machine was used to load the sample. A light steel piston compressed the foam specimens (cylindrical specimens of diameter 11 mm and height 5 mm) by moving at velocities of the order of 0.05 ms^{-1}, corresponding to impose strain rates of the order of 10 s^{-1} with negligible acceleration times. The maximum achievable axial strain was limited to a maximum of 0.3 by the capacity of the loading system. High-speed photography was employed to observe the experiments during deformation. The load was measured by a resistive load cell while the shortening of the sample was measured by both LVDT transducers as well as by optical methods (Vision Research, Phantom model 7.1 and image analysis software). Equipment noise was filtered using a 10 point moving average filter [115]. The material response (Figure 3-17, Figure 3-18) was similar to that observed in quasi-static tests, comprising an elastic phase followed by a strain hardening regime. For all materials, the measured flow stress was significantly larger at this strain rate than that measured in the quasi-static tests.

3.5.2 Medium rate experiments tension

The same basic apparatus was used for tensile tests of sintered Ti powders of 4100 Kgm^{-3} $\bar{\rho} = 0.9$ at rates of (10-20 s^{-1}). Specimens were designed as in figure (Figure 3-11) and were held by threaded ends attached to the fixtures and piston. Similar to compression the elastic region was followed by plastic deformation.

Figure 3-20 represents a comparison of the stress versus strain tensile response of the sintered powder 4100 Kgm^{-3} ($\bar{\rho} = 0.9$) at different strain rates. The strain hardening rate was insensitive to imposed strain rate. However the plastic region was in the form of a plateau leading to material failure at nominal strains of around 0.15.

3.5.3 High rate experiments compression

In order to achieve a strain rate of 2 x 10^3 s^{-1}, a split pressure Hopkinson bar (SPHB) setup was used [55], with all bars made from hardened steel. The forces acting on the specimen ends were recorded by the strain gauges on the input and output bars, and the sample shortening was estimated via both stress wave analysis and high-speed photography. Force equilibrium was typically reached after 10 µs, corresponding to an axial strain around 0.03, and the imposed strain rate was approximately constant after this time.

Figure 3-18 shows a similar comparison of the stress versus strain responses for a foam of density 1892.5 Kgm^{-3} ($\bar{\rho} = 0.42$), which was shown to contain pores of diameter of the order of 100 µm. While the material stiffness seems independent of the strain rate, the yield stress increases with increasing strain rates. In contrast with what was observed for the sintered powder the strain hardening rate also displayed a mild increase with increasing strain rate.

Cracks were found to propagate through both the necks in-between sintered powder particles and through the powder particles (Figure 3-19). Stress concentration and defects within the material can determine the route of cracks during the fracture process. Sheared material and large cracks around pores were found after both quasi static and dynamic tests. However the micro cracks through powder particles (Figure 3-19 c, d) were mainly located on high strain rate test specimens.

Figure 3-17 represents a comparison of the stress versus strain response of the sintered powder (4100 Kgm^{-3} $\bar{\rho} = 0.9$) at different strain rates. Recall that the microstructure of this material was associated with pores of diameter of the order of

10 µm. The initial apparent stiffness was independent of strain rate, whereas the yield stress increased as the strain rate increased from 10^{-2} - 10^{3} s^{-1}. The strain hardening rate was insensitive to imposed strain rate. Figure 3-19 shows the post-test SEM examination of the compression specimens at low and high strain rates.

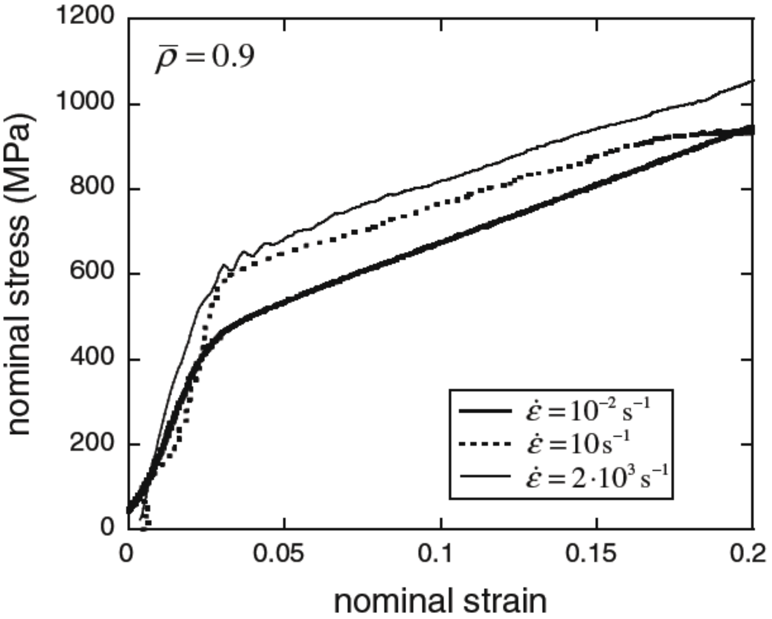

Figure 3-17 Compressive nominal stress versus strain response of sintered powder of density4100 Kgm^{-3} ($\bar{\rho} = 0.9$) at low, medium and high strain rates.

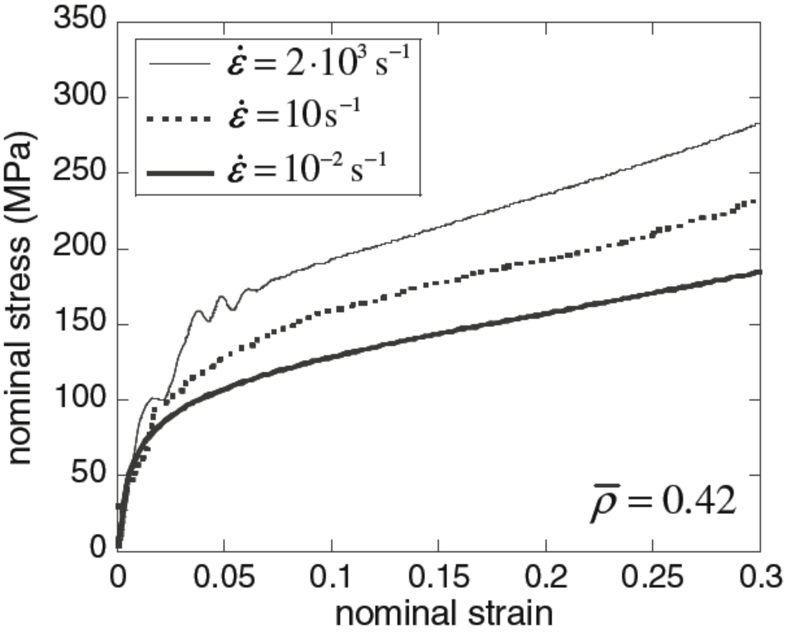

Figure 3-18 Compressive nominal stress versus strain response of a foam of relative density 1892.5 Kgm^{-3} ($\bar{\rho} = 0.42$) at low, medium and high strain rates

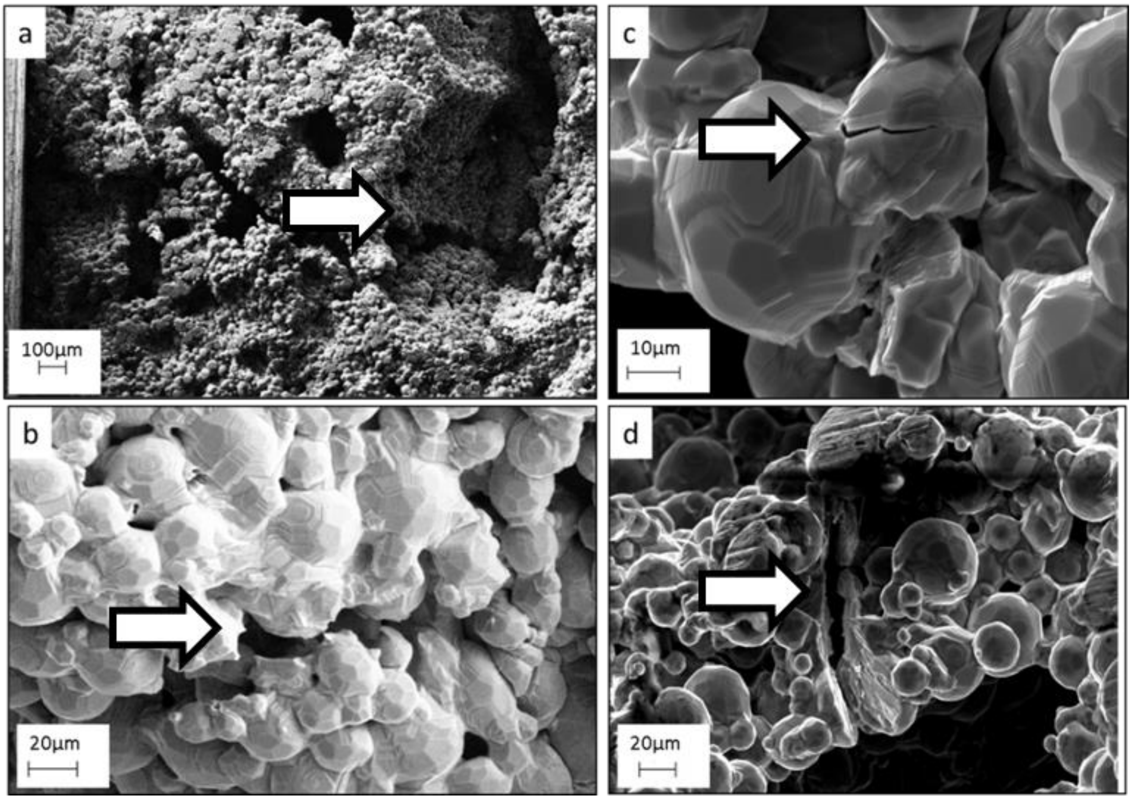

Figure 3-19 Failure modes of foams under compression at high and low strain rates. Arrows show propagated cracks.

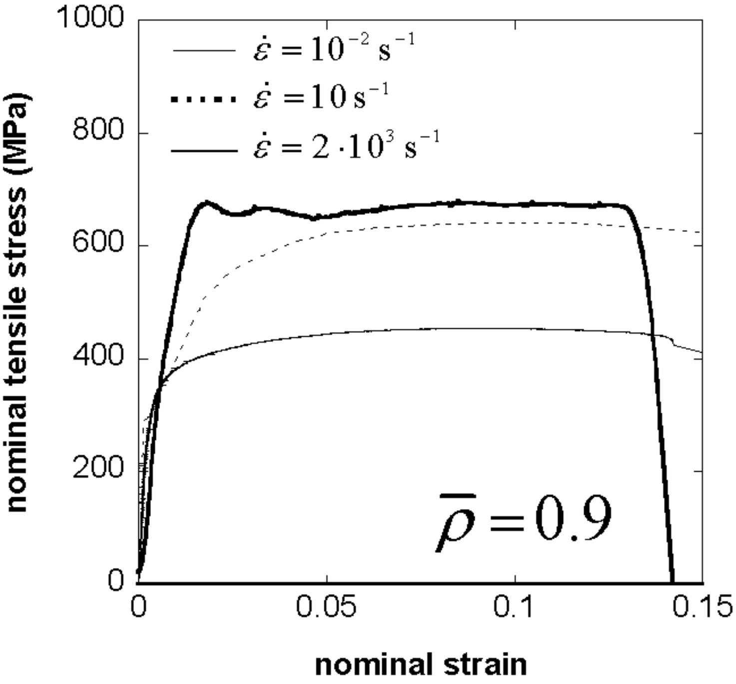

Figure 3-20 Nominal stress versus strain response of sintered Ti powder of relative density 4100Kgm^{-3} ($\bar{\rho} = 0.9$) at low, medium and high strain rate of deformation in tension.

Similarly to high rate compression, a tensile split Hopkinson bar was used for testing sintered Ti powders of density 4100 Kgm^{-3} ($\bar{\rho} = 0.9$) at high strain rates (up to ~2500 s^{-1}). Specimens were of the same design used for quasi static and medium rate tests. The threaded end of the specimens was attached to the bars.

Figure 3-20 shows a comparison of the stress versus strain tensile response of the sintered powder 4100 Kgm-3 ($\bar{\rho} = 0.9$) at different strain rates. The strain hardening rate was insensitive to imposed strain rate. However the plastic region was in the form of a plateau leading to material failure at nominal strains of around 0.15.

Figure 3-21 shows post-test SEM examination of the failure surface. The material around the micro pores is elongated at the direction of deformation. Macroscopic necking of specimen and microscopic necking of the material around the micro-pores is followed by failure.

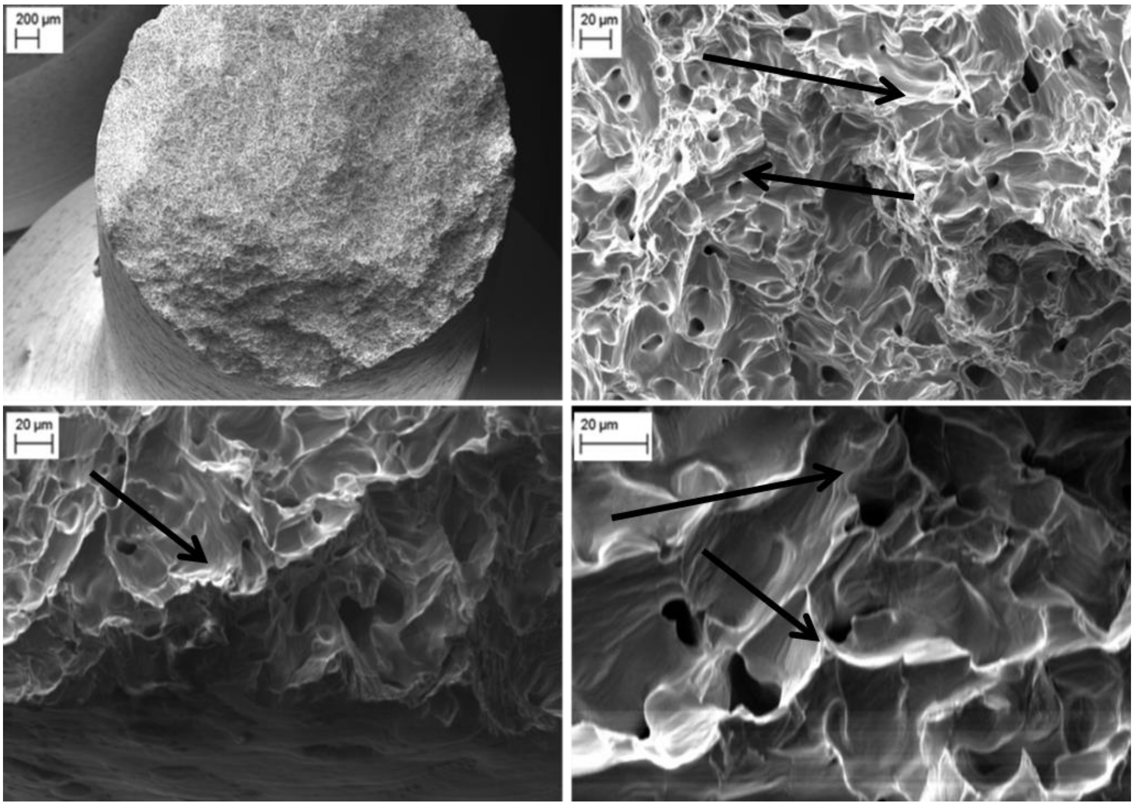

Figure 3-21 Fracture surface of sintered Ti powders 4100 Kgm^{-3} ($\bar{\rho} = 0.9$) under tension

3.6 **Taylor impact**

A nitrogen gas gun was used to accelerate cylindrical foam projectiles of diameter 12 mm and length of 47 mm. The foam projectiles were targeted at a rigid bar with hardened steel end cup. The forces were measured using strain gauges and strains on the specimen, using high speed photography (Figure 3-22).

Figure 3-23 represents a typical stress versus time response of a Taylor impact test. The material progressively widens toward the contact surface forming a cone that grows as the plastic wave moves in the direction of the free end (Figure 3-22). The speed of the projectile was 189 ms^{-1} and the average speed for the deformed cone front was 136 ms^{-1}. The deformed cone (Figure 3-22) is formed by a complex strain field were plastic deformation is dominant. Stress at a strain of 0.34 appeared lower than expected possibly due to crack forming by the lateral deformation at the bottom of the cone. Taylor impact tests are commonly used for validation purposes of material models.

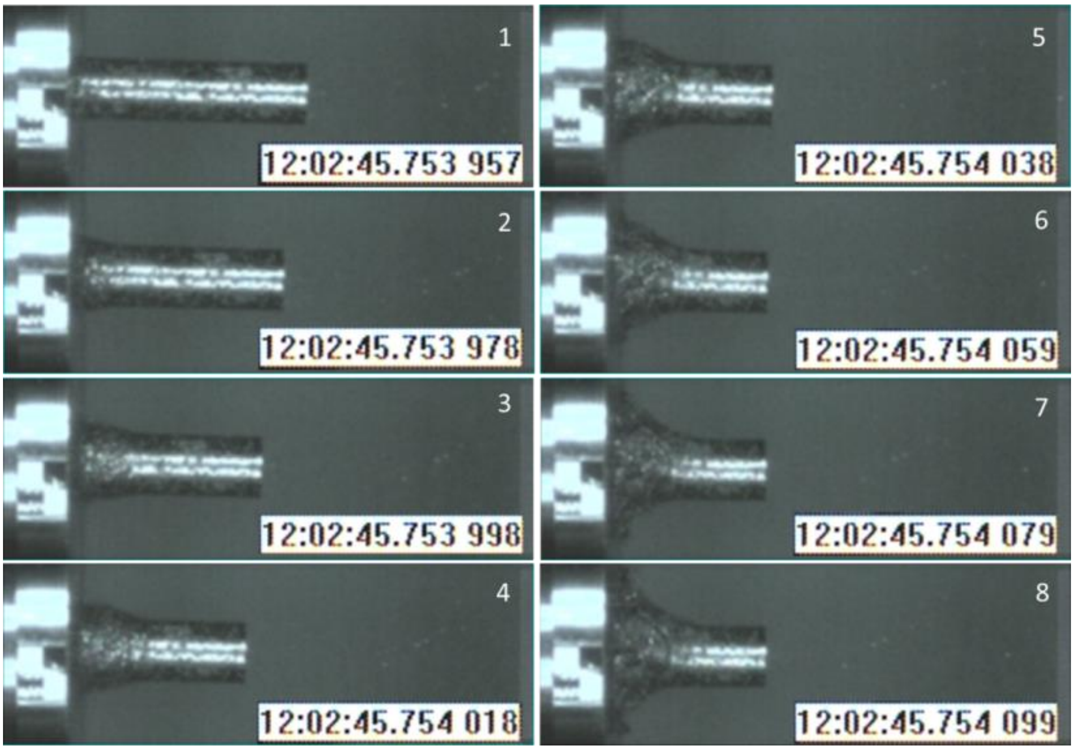

Figure 3-22 Frame sequence of a Taylor Impact test on foam of relative density 1802 Kgm^{-3} ($\bar{\rho} = 0.4$)

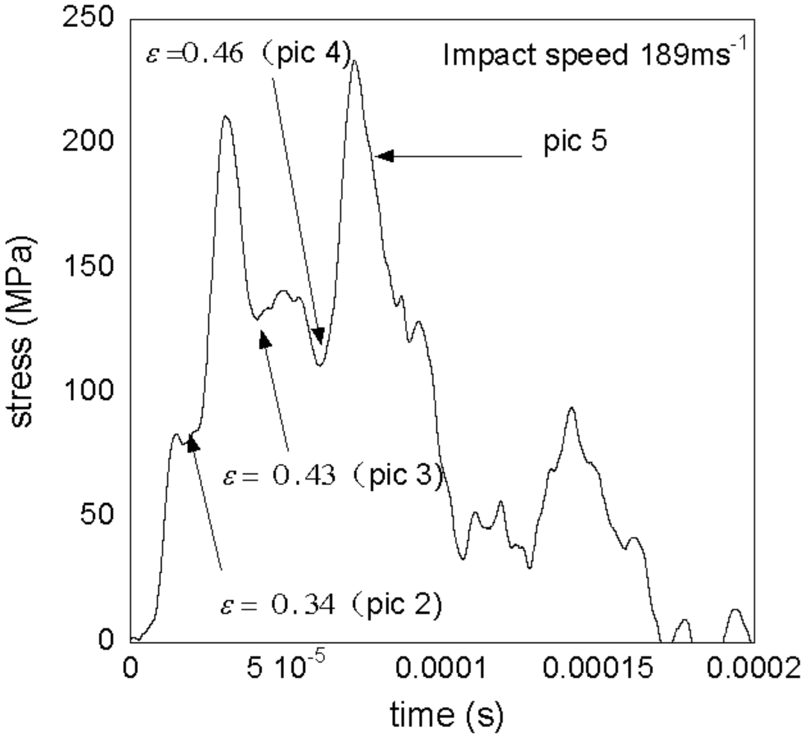

Figure 3-23 Stress in time for a Taylor impact test of a foam of relative density 1802 Kgm^{-3} ($\overline{\rho} = 0.4$)

Both quasi-static and dynamic experiments were repeated at least three to five times for each strain rate and each foam density considered. Results of the stress response were fitted by a power law curve in scaling with density (Figure 3-24).

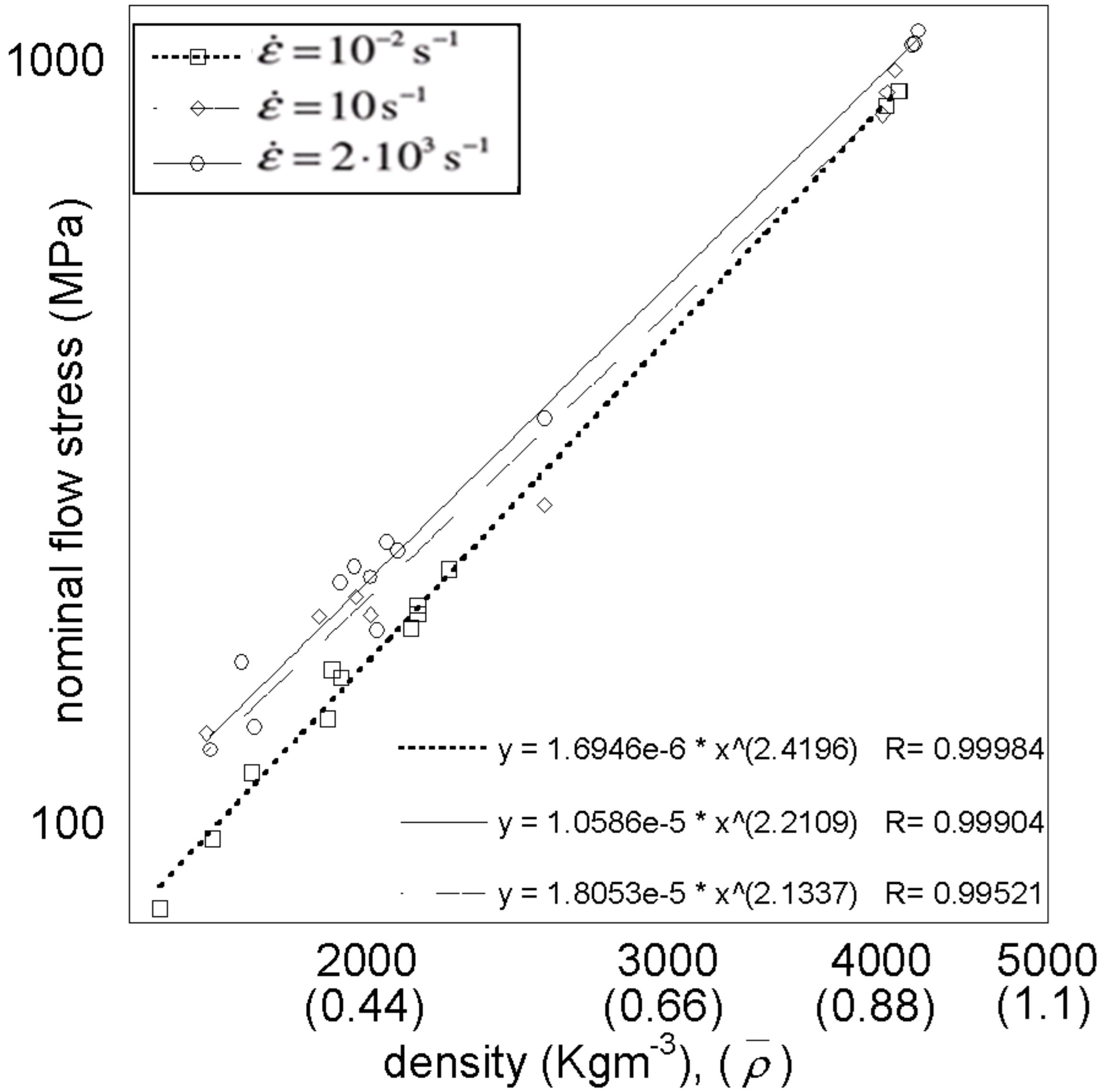

Figure 3-24 Measured flow stress (at a plastic strain of 0.2) as a function of foam density, in low, medium and high strain rate experiments

The variation of the flow stress as a function of density and strain rate is presented in (Figure 3-24). At each strain rate, the yield stress varies with foam density according to a power- law with exponent and intercept depending on the imposed strain rate. It can be deduced from Figure 3-24 that for low-density foams the yield stress increases by about 30 % as the strain rate is increased from 10^{-3} to 2 x 10^3 s^{-1}. For sintered powders, the material strain rate sensitivity seems to be lower: the yield stress increases by only 13 % with the same increase in strain rate.

3.6.1 Essential experimental data for modelling purposes

Table 3-1, includes basic experimental data expressed in power law fits that can be used for modelling Ti foams of these densities and type. The table includes the elastic modulus as a function of density (fit to experimental data points) and nominal stress values at a strain of 0.05 and 0.2 for foams of 1600 kgm^{-3} for quasi static (QS), medium rate (MR) and high rate (HR) compression (Figure 3-25). Additionally the nominal stress as a function of density (ρ) (fit to experimental data points) is included for nominal strain of 0.05 and 0.2 at quasi static and high strain rates. In-between values for various densities, strains and strain rates can be extrapolated based on the data presented below. The Pearson’s correlation coefficient indicates how well the calculated curve fits the data.

Elastic Modulus ρ=1600-4100 kgm^{-3}: E = 8.3709e-6 * ρ^(2.7527) R=0.99367

ε=0.05 (1600-4100kgm^{-3})	(MPa) $\sigma_{0.05}$ =f(1600kgm^{-3})	(MPa) $\sigma_{0.05}$ =f(ρ)	Correlation coefficient
Q S ($\dot{\varepsilon} = 0.01$)	70	$\sigma_{0.05}$ = 1.83e-5 * ρ^(2.0552)	R=0.99772
MR ($\dot{\varepsilon} = 10$)	70	$\sigma_{0.05}$ = 2.134e-6 * ρ^(2.3397)	R=0.97989
HR ($\dot{\varepsilon} = 2X10^3$)	97	$\sigma_{0.05}$ = 2.3868e-5 *ρ^(2.0566)	R=0.9983

ε=0.2 (1600-4100kgm^{-3})	(MPa) $\sigma_{0.2}$ =f(1600 kgm^{-3})	(MPa) $\sigma_{0.2}$ =f(ρ)	Correlation coefficient
Q S ($\dot{\varepsilon} = 0.01$)	98	$\sigma_{0.2}$ = 1.6937e-6 * ρ^(2.4196)	R=0.99984
MR ($\dot{\varepsilon} = 10$)	127	$\sigma_{0.2}$ = 1.8044e-5 * ρ^(2.1337)	R=0.99521
HR ($\dot{\varepsilon} = 2X10^3$)	134	$\sigma_{0.2}$ = 1.058e-5 * ρ^(2.2109)	R=0.99904

Table 3-1 Basic data on material compressive behaviour of Titanium foams in the range of ρ=1600-4100 kgm^{-3} ($\bar{\rho} = 0.35 - 0.9$) for low, medium and high strain rate.

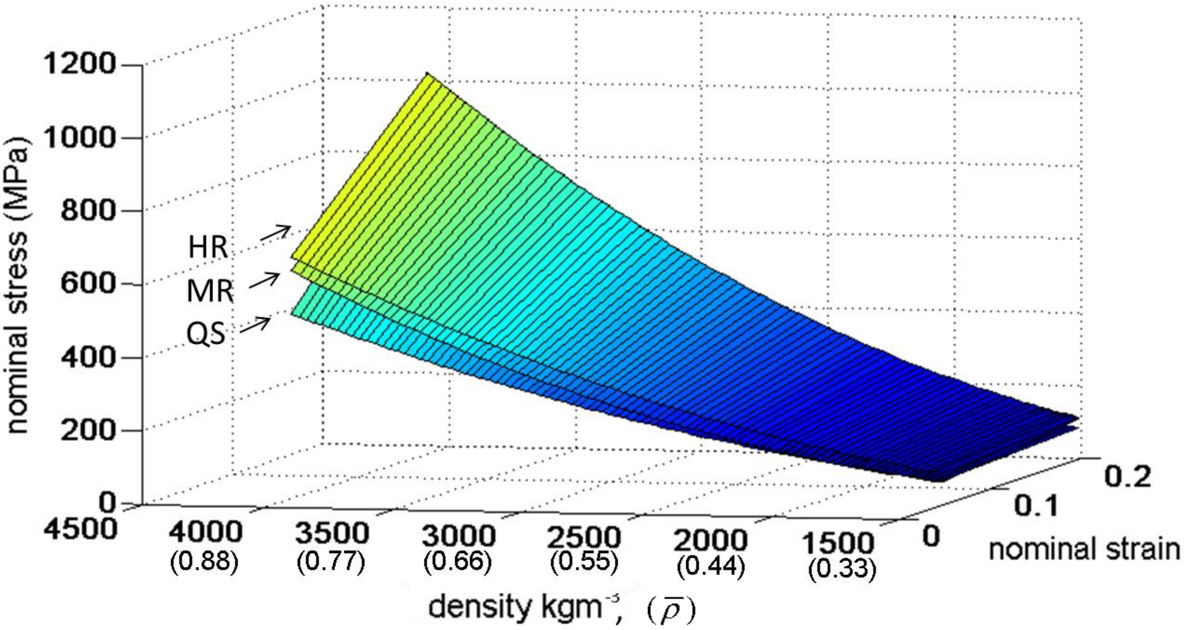

Figure 3-25 3D stress surfaces for compression as a function of density and nominal strain (ε=0.05--0.2) for 3 strain rates of deformation: quasi static (Q S $\dot{\varepsilon} = 0.01$ s^{-1}), medium rate (MR $\dot{\varepsilon} = 10$ s^{-1}) and high rate HR ($\dot{\varepsilon} = 2\text{X}10^{3}$ s^{-1}).

3.7 **Discussion**

Three densities ($\bar{\rho} = 0.35, 0.42, 0.48 \pm 0.5$) and the parent material ($\bar{\rho} = 0.9$) were examined in order to investigate the mechanical behaviour of the material and establish scaling laws. The range was restricted by financial limitations and was defined by the range that would be most suitable for biomedical implants [7, 88]. The manufacturing method may present limitations in higher porosities as Ti powder particles may be insufficiently bonded during the foaming procedure.

Compression specimens were manufactured in the diameter that was tested and therefore no machining was required. Foam tensile and shear specimens were machined to dimensions. The machining process resulted in a surface layer of smeared material that was significantly smaller in comparison to the specimen dimension. Specimen gauges (3-5 mm) were significantly larger than the order of pore size ($2X10^2$ μm). Recommendations in literature given by [46], suggest that the smallest linear dimension of the specimen should be at least seven times the cell size to assume homogeneity and avoid size effects. This recommendation comes from a study conducted by [112] where specimen size effects on the Young's modulus and the plastic collapse stress of a closed-cell Alporas and an open-cell Duocel foam were investigated. The outcome of their investigation shows that the strength and modulus measurements are independent of size when the sample dimensions exceed the cell diameters by about 7 times. This requirement is not confined to the specific foam materials and other authors quote similar measurements when calculating the minimum number of grains required across the diameter of a specimen, for specimen homogeneity in polymer or composite materials (Siviour 2005; Drodge 2011) [113].

Further experimental investigation would ideally include:

Tension and shear: Foams of at least two or more densities to be tested at least two or more strain rates. The specimens would ideally be machined by either water jet or electric discharge (wire) cutting. A larger range of specimen sizes would allow to investigate any potential size effect for the densities under examination and ensure better testing conditions such as approximating perfect shear in the case of the I-beam specimen.

In situ testing: X-ray micro tomography of higher resolution could be employed to investigate the deformation and failure mechanisms under different testing modes (interrupted compression, tension). The captured reconstructed geometry for different strains would assist in further understanding these mechanisms and also provide direct comparison between experiment and simulations at the mesoscale level. In situ SEM for tension testing of foams would also allow investigating failure modes.

3.8 **Conclusions**

Porous solids made from sintered commercially pure Ti powder were studied; the microstructure of these solids comprised (i) micro-pores (diameter 10 µm) of round, smooth shape, resulting from the incomplete sintering of the gaps between titanium powder particles and (ii) macro-pores (diameter >100 µm) of irregular shape and sharp corners, formed by the decomposition of the foaming agent. The sintered Ti powder tested presented only micro- porosity, while the sintered Ti foams presented both micro- and macro-porosity.

Upon loading in compression foams initially deform elastically and subsequently collapse plastically by flattening of the macro-pores perpendicularly to the loading direction. For the sintered powder (4100 Kgm^{-3} $\bar{\rho} = 0.9$), produced without binder and foaming agent, plastic collapse occurs by flattening of the micro-pores. The pore-flattening mechanism is accompanied by traverse strain; the Poisson's ratio is found to increase with the imposed axial strain at a rate depending on the foam density. At compressive axial strains in the range 0.15–0.3, micro-cracking is observed. At sufficiently high axial strains the strain hardening rate increases for these foams, due to material densification by complete closure of the pores. The densification strain increases as the foam relative density decreases.

The mechanical response of the foams is sensitive to relative density; elastic modulus, yield stress and the strain hardening rate increase with the foam relative density. Comparisons of the measured stress–strain responses at different strain rates revealed that the material response is sensitive to the applied strain rate.

Sintered Ti powder (4100 Kgm^{-3} $\bar{\rho} = 0.9$) displays an increase of the yield stress with strain rate comparable to those observed by other authors [6–8] for fully dense crystalline Ti alloys. This elevation in yield stress was measured to be of 13 % as the strain rate was varied from 10^{-2} to 2 x 10^{3} s^{-1}; for these sintered powders, the strain hardening rate is independent of the applied strain rates.

Foams ($\bar{\rho} = 0.3 - 0.5$) display an elevation of both yield stress and strain hardening rate with increasing applied strain rate. The strain rate sensitivity appears to be more pronounced for foams of lower relative density: foams with relative density 1486 Kgm^{-3} $\bar{\rho} = 0.33$ displayed an elevation of 32 % in flow stress (at a plastic strain of 0.2) as the strain rate was varied from 10^{-2} to 2 x10^{3} s^{-1}. Deformation mechanisms observed via quasi-static in situ testing for the foams were insensitive to relative density. However increased porosity in the foam microstructure in combination to the rough texture of the pores may result in inertial stress fields, affecting the deformation and failure mechanisms.

The surfaces of the examined foams are highly textured due to the sintered powder particles used during manufacturing (Figure 3-1). SEM in situ observations show that deformation mechanisms involve pore flattening that leads to opposing surfaces folding and interacting (Figure 3-10). In addition post test SEM reveals smeared powder particles as well as cracks through the particles and necks.

It could be conjectured that the ligaments and powder particles on the interacting surfaces are less constraint during quasi static interactions rather than in high rate.

During quasi static interactions powder particles on interacting surfaces are more able to slide on the periphery of each other; rather than during high rate. During high rate interactions the ligaments and powder particles are additionally constraint by the effects of inertia on the lateral directions. The inertial effects add rigidity to the ligaments restricting the interacting powder particles from sliding around and bypassing obstacles. Ligaments that are interacting by partially intercepting powder particles; that would otherwise shift or move quasi statically by deformation of the ligaments; may be blocked by inertial constraints subsequently increasing the stress response.

Higher porosity foams have larger open surfaces and therefore a larger number of surface interactions occurring during pore flattening and surface folding (e.g. $\varepsilon = 0.2$) (Figure 3-24). Therefore the effect is more pronounced in higher porosities and contributes positively to the relative strain rate sensitivity of the material. Quantifying the effect of surface roughness and strain rate on surface interactions for different densities will be a subject of future work.

This is not the only possible explanation for the enhanced strain rate sensitivity in foams compared to that observed in sintered Ti powders: further microscopic observations and modelling of the dynamic foam deformation and fracture should be conducted in order to aid interpretation of the observed strain rate sensitivity.

4 Modelling Ti foam structures

Summary

A method for generating realistic microscopic foam geometries is developed for modelling the structure of medium density foams 1622-2207 Kgm^{-3} ($\bar{\rho} = 0.36 - 0.49$). The method employs 3D Voronoi cells corresponding to a pore size distribution thus providing statistically representative (virtual) samples of given materials. The virtual geometries are meshed and imported into finite element software. A range of loading modes is simulated and predictions are compared against experimental data for open cell Titanium foams. Complex loading modes that could not be achieved in reality are investigated in order to establish the framework for determining the macroscopic properties of materials under consideration.

4.1 **Foam geometry.**

The pores of highly irregular foams form complex networks of random shapes and texture. Voronoi polyhedrals are suitable for replicating these random structural characteristics by using them either individually or in clusters of Voronoi cells. The Voronoi tessellation is a method by which a space is separated in cells [116]. Every point in the periphery of the cells is closer to its seed point than to any other. In 3D the Voronoi tessellations produce polyhedrals. Their size and shape depends on the amount and position of the initial seed points.

The microstructure of the foams was generated using random Voronoi 3D tessellations. The Voronoi polyhedrals were randomly placed within a cube. The cavity in-between the polyhedrals and the boundary of the cube was meshed and then the polyhedrals were deleted creating a network of pores (Figure 4-1).

The foam structure produced by this method is defined as follows:

A number of bounded $\mathrm{X_i}$ volumes (Voronoi cells), form a set called X where

$\mathrm{X} = (\cup \mathrm{X_i})$ and $\mathrm{X_1, X_2, X_3 .... X_n} \subseteq \mathrm{R}^3$.

The set X : is bounded by an external surface B that contains a volume V_B where $\mathrm{X_i} \subseteq V_\mathrm{B} \forall \mathrm{i}$

The Foam space Y is defined by equation 4-1 and demonstrated in (Figure 4-1)

$$\mathrm{Y} = V_\mathrm{B} - (\cup \mathrm{X_i}) \text{ where } \mathrm{Y}, V_\mathrm{B} \subseteq \mathrm{R}^3 \tag{4-1}$$

The foam's type (open or closed cell), inner structure and texture, can be changed by altering characteristics and criteria of the set X (of Voronoi polyhedrals) (Figure 4-3, Figure 4-4).

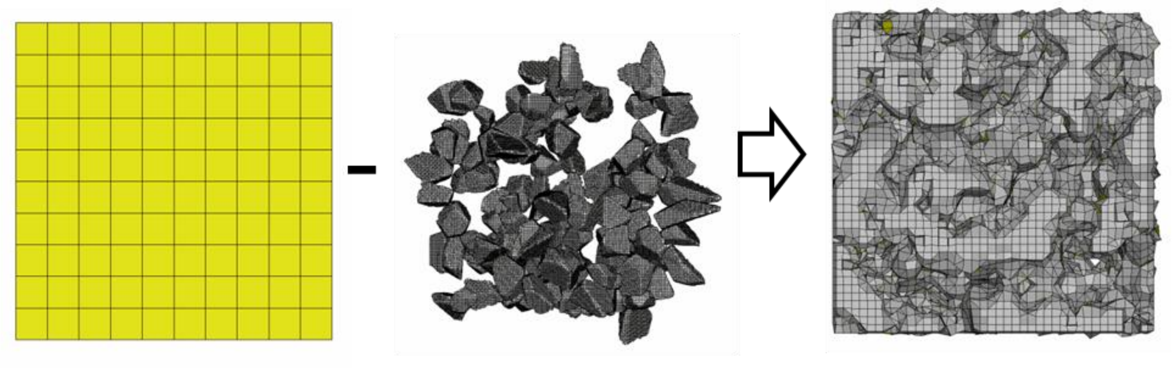

Figure 4-1 Graphic representation of the stochastic geometry generation. The randomly shaped Voronoi polyhedrals are used to form the pore network. The cavity in-between the polyhedrals (set of pores) and the boundary of the cube is meshed and then the polyhedrals are deleted creating a network of pores.

For each virtual specimen a set of pores was produced to form the structure. The size distribution of the set was based on XMT scans performed on this type of foams Figure 4-5 [101]. The volume ratio between the pore set and the specimen would give the macroporosity. The volume of the pore set (Voronoi polyhedrals) was kept constant and porosity was regulated by altering the size of the specimen. The representative volume element for the geometrical characteristics was defined as the volume that can enclose the set of pores from the distribution (Figure 4-5) and produce the desirable ratio of pore to specimen volume. The size of the surrounding cubic frame was then defined based on the needed cube volume that would produce the targeted pore to specimen ratio (porosity). The pseudo-code algorithm of the proposed methodology is summarised in (Figure 4-2). The individual steps are further explained throughout this chapter.

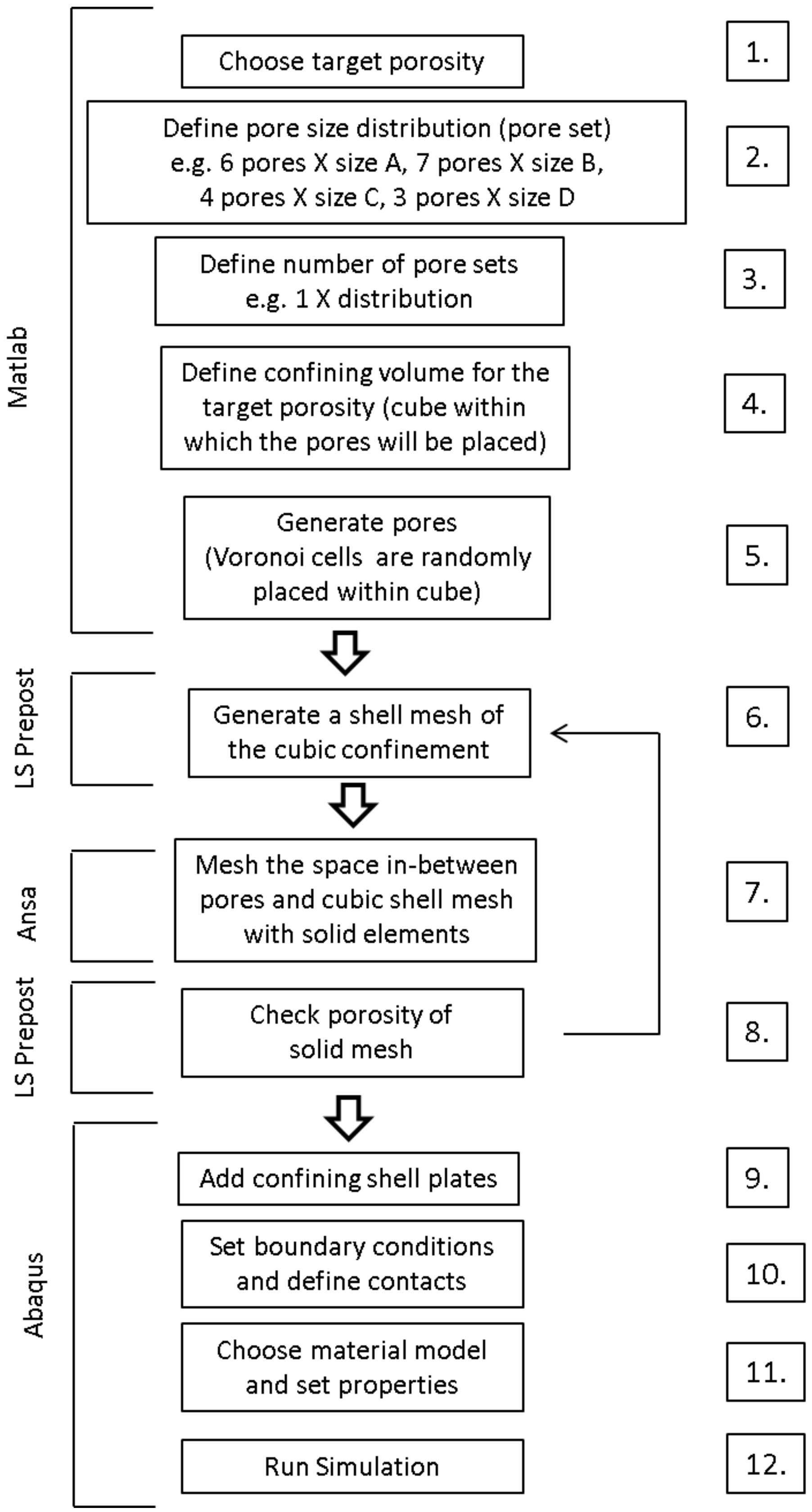

Figure 4-2 Schematic representation of steps for the proposed modelling methodology.

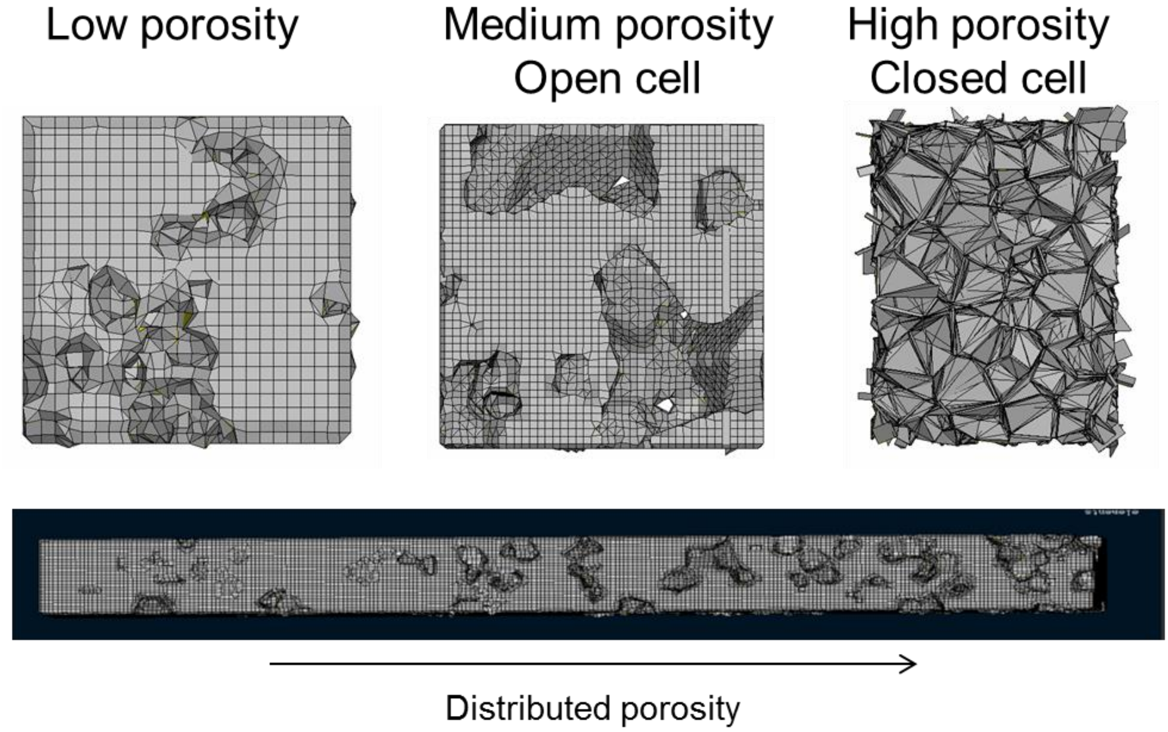

Figure 4-3 Geometries produced using Voronoi cells. Changing the statistical characteristics of the seed points results in different types of foam.

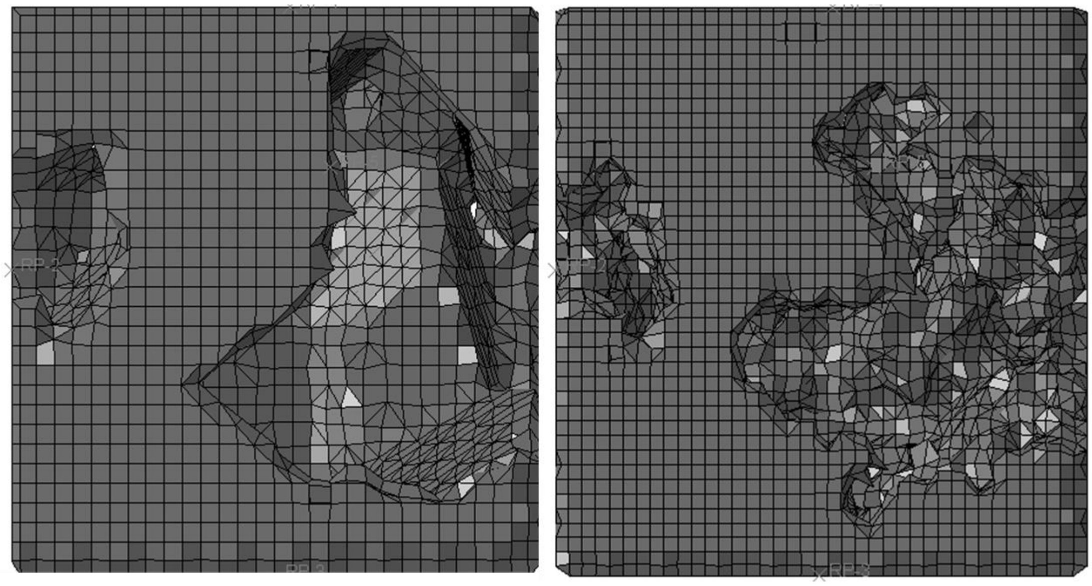

Figure 4-4 Comparison of a foam structures with smooth (left) and rough (right) cell walls. Clusters of Voronoi cells can form pores to replicate the texture of the sintered powders.

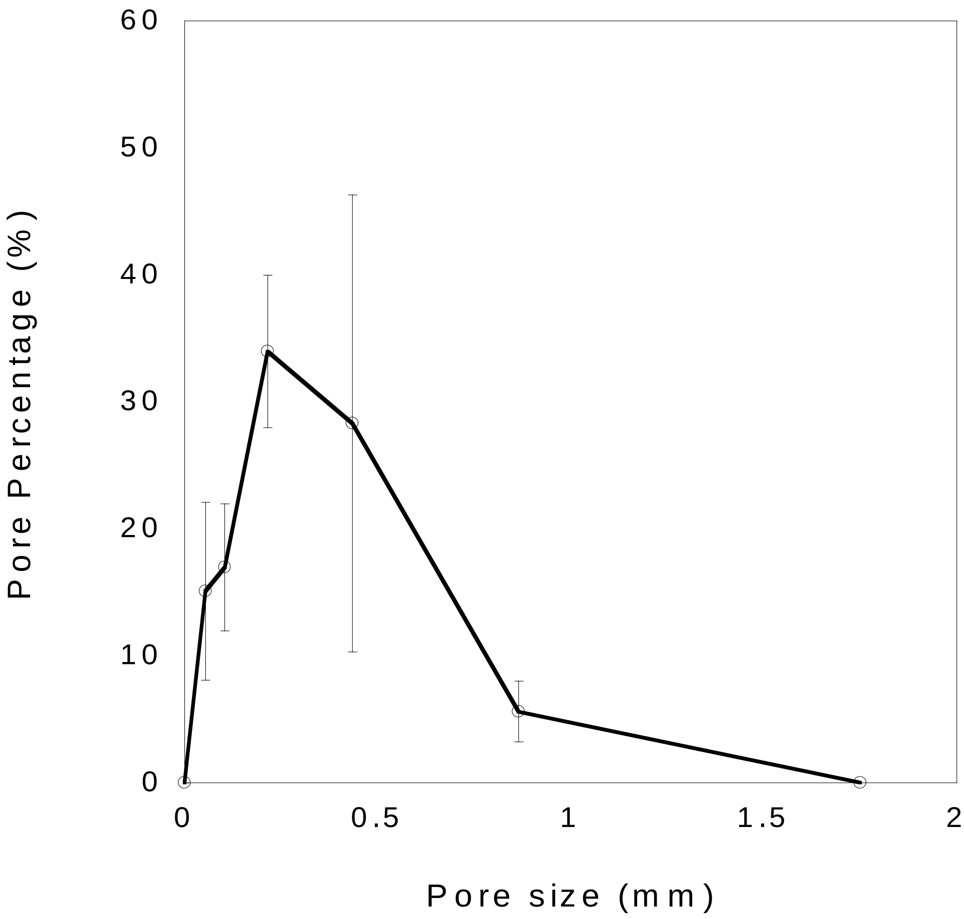

Figure 4-5 Pore size distribution obtained using X-ray micro tomography. [101]

The average polyhedral size was controlled by the number of points within the cube (eq. 4-2). The polyhedral sizes followed the target pore size distribution (Figure 4-5) [101]. The distribution curve was discretised to 4 intervals (Figure 4-6). For each interval of the pore size distribution (Figure 4-5) a number of points was randomly placed within the estimated cube volume. The number of points was calculated using (eq. 4-2) to achieve the desirable pore size. The volume was then separated to Voronoi polyhedral and a number of cells corresponding to the distribution was flagged as pores Figure 4-6. A proximity criterion was applied in choosing suitable pores so that pores of different size intervals would not completely overlap. The criterion was defined by considering a distance around the seed points that corresponded to the equivalent radius of a sphere of the same volume as the average polyhedral cell. Due to the irregular shape of the cells the criterion can allow for some overlapping therefore creating open cell structures (Figure 4-7)

$$\overline{V}_{\mathrm{p}} = \frac{V_{\mathrm{B}}}{\mathrm{i}} \tag{4-2}$$

Where $\overline{V}_{\mathrm{p}}$ is the average pore size, V_{B} is the specimen volume size, i is the number of seed points.

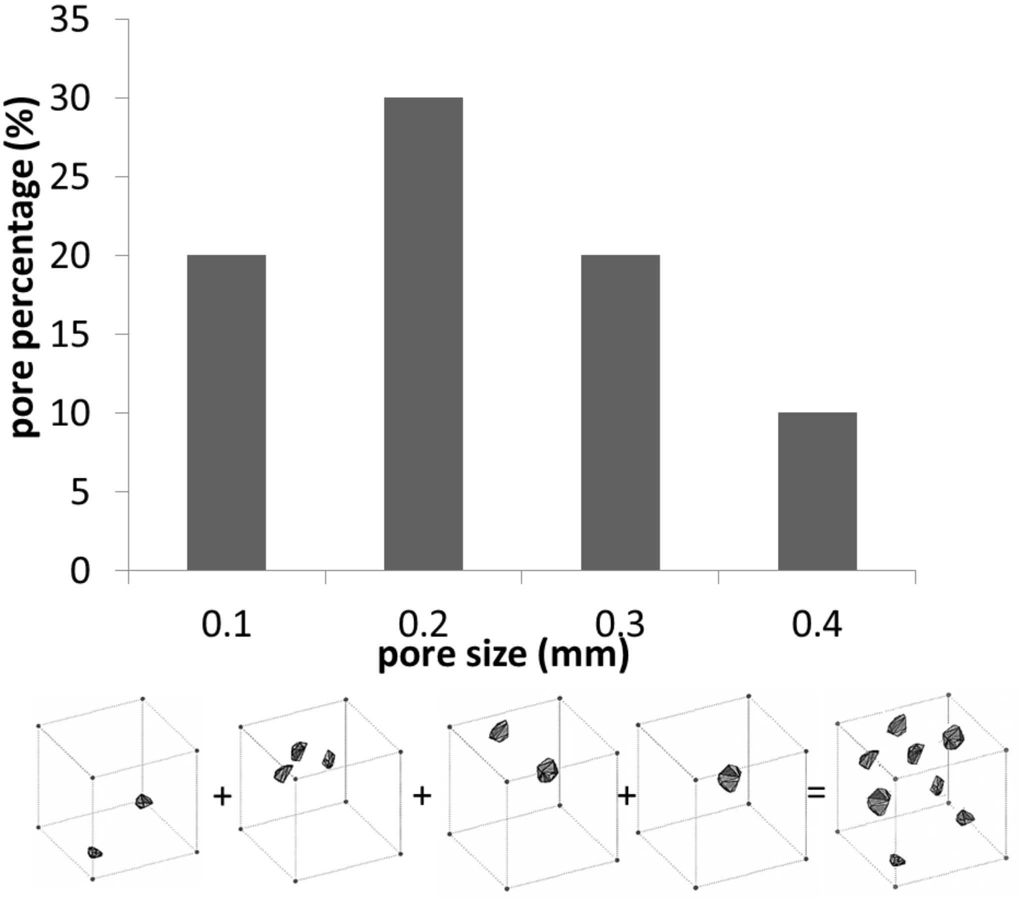

Figure 4-6 Graphic representation of the method used for discretising the pore size distribution and adding pores in the cubic confinement. The set of pores that corresponds to the distribution is added within the volume to achieve the desired porosity. A proximity criterion is applied.

The experimentally examined foams (see previous chapter) had two types of porosity. Macro-pores, given by the distribution (Figure 4-5), were of the order of 100 µm and micro-pores of the order of 10 µm at a percentage of 10 % within the parent material (see Figure 3-1). The parent material was formed by sintered Ti powders [101]. The Voronoi polyhedrals were used to generate the macroporosity. However the microporosity was taken into account in calculating the total porosity and the volume of the virtual specimen.

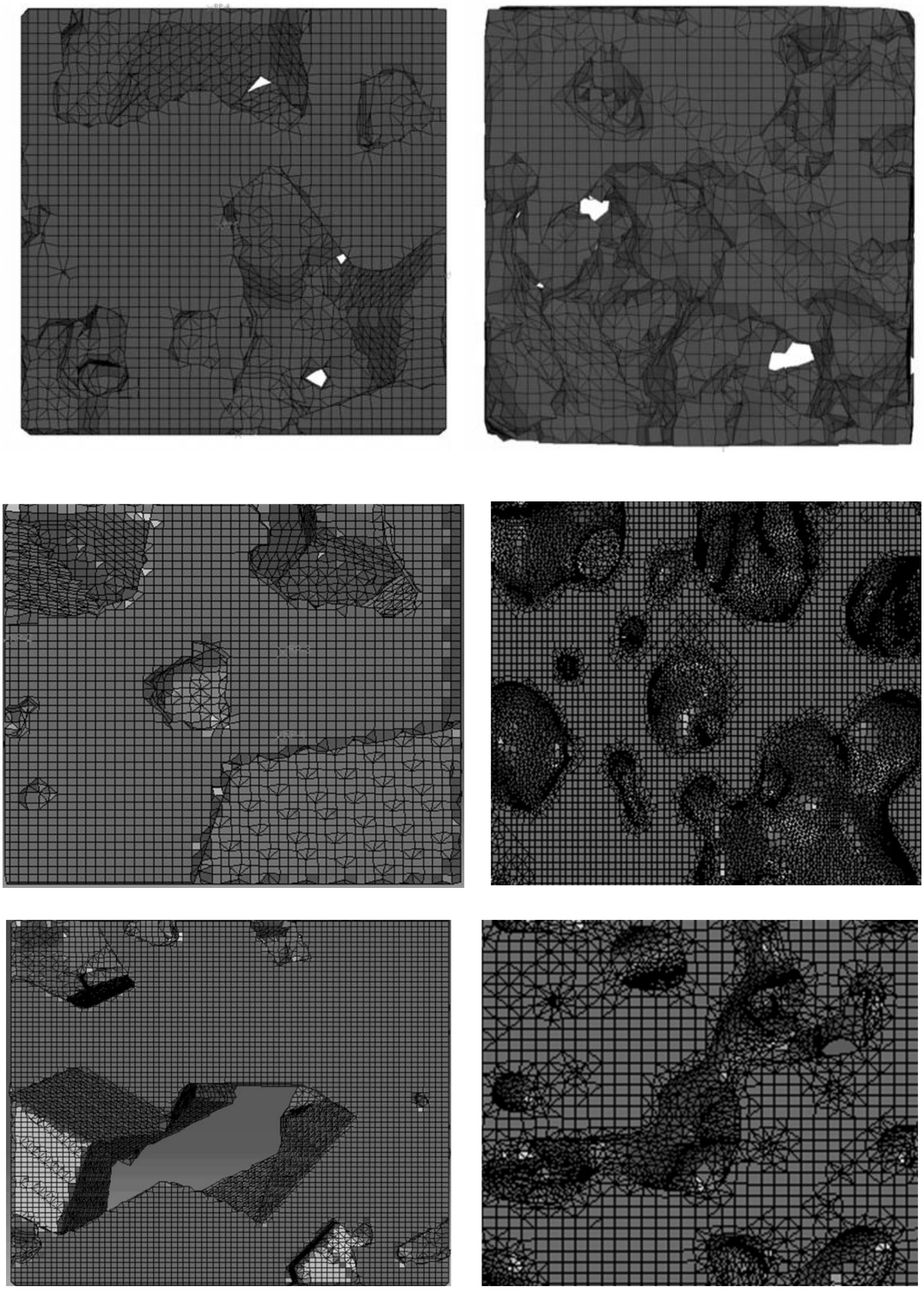

Figure 4-7 Foam meshes of relative density ρ=2072 kgm^{-3}, $\bar{\rho} = 0.46$ (top), ρ=1784 kgm^{-3}, $\bar{\rho} = 0.39$ (middle) and ρ=1982 kgm^{-3} $\bar{\rho} = 0.44$ (bottom). The foam geometries on the left are virtually produced with smooth surfaces using Voronoi polyhedrals and the geometries on the right are scanned specimens obtained via XMT (right).

The foam’s total porosity (volume of all pores to the volume of the specimen) is given by (eq.4-3). The total porosity for the virtual specimens was chosen to either replicate existing foam specimens or virtually generate densities of the same type and compare predictions with experimental data fit. The volume of macro-pores was given by the distribution. Macro-porosity (volume ratio) was calculated through (eq 4-3, 4-4). The volume of the cubic specimen V_B is then defined by solving (eq.4-5) in respect to V_B

An iterative process was followed to achieve good match of target porosity [101] and the porosity of the generated foam. The irregularity of the polyhedral cells results to some porosity loss that causes divergence between the final porosity from the originally targeted. The loss is mainly due to the partial overlapping amongst the pores and between pores and specimen boundary. Partial overlapping is necessary for creating the open cell structure. An average correction factor (c) was taken into account (eq. 4-5) for iteratively defining the specimen volume V_B. For the first attempt, equation (eq. 4-5) would be solved in respect to V_B considering c equal to zero. The factor (c) would then be determined as the difference of targeted macroporosity P_M and the actually achieved porosity. Based on the new (c) equation (4-5) would be solved again in respect to V_B so that to adjust the volume to the geometry irregularity and partial pore overlapping. The difference would commonly be very small in volume but due to the small specimen size it could produce a significant divergence in density.

$$P_t = P_M + P_m \tag{4-3}$$

$$P_m = 0.1(1 - P_M) \tag{4-4}$$

$$\mathrm{P_M} = \frac{1}{V_\mathrm{B}} P_\mathrm{N} \sum_{1}^{n} A_n V_n - \mathrm{c} \tag{4-5}$$

Where: $\mathbf{P}_\mathrm{t}$ is the total porosity, $\mathrm{P_M}$ is porosity due to macro-pores, $\mathrm{P_m}$ is porosity due to micro-pores, A_n is the probability of each pore size from the distribution curve, P_N is the number of all macro-pores (pore set), V_n is average size of each of the size intervals, V_B is volume of specimen, n is the number of size intervals from the distribution, c is a correction factor related to the irregularity of pores and degree of overlapping (c is defined through an iterative process).

The cavity between the cube and the Voronoi cells was meshed using commercial software [117] using linear elements.

The Voronoi cells on the boundary of the cubic space would often have sharp edges and extend their boundaries outside the cube. The quality of the Voronoi cells was improved by tessellating a larger cubic space than needed and only using cells from the interior core rather than the boundary Figure 4-8 (Left).

A combination of developed code and commercial software was used to produce the foam mesh. The Voronoi polyhedrals were produced using code developed in Matlab [115] that would export a shell mesh in (.key) LS Dyna format [118] (Figure 4-8). The confining shell cube would then be produced in LS Dyna-prepost software and then imported in commercial meshing software (Ansa Beta CAE) [117] where it would be meshed as a solid and exported for FE software in (.inp) Simulia Abaqus [119] format (Figure 4-9).

The produced meshes would have between 38000-83000 nodes and calculation required approximately 12-20 hours.

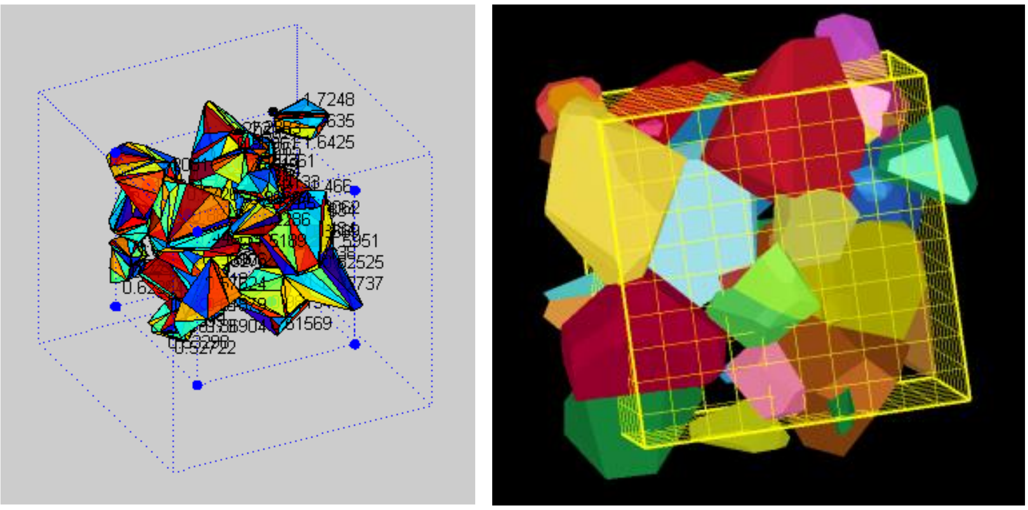

Figure 4-8 (Left) Voronoi polyhedrals forming a pore network. The pore sizes follow a specific distribution and the polyhedrals are produced using matlab code. (Right) The pores are confined within a cubic shell using LS-Dyna prepost software.

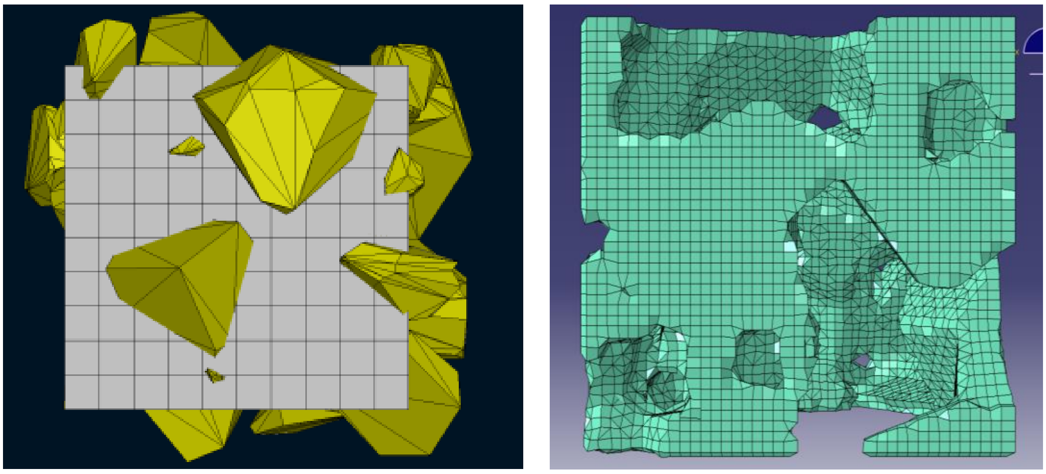

Figure 4-9 (Left) Pores are confined within a cubic shell mesh and imported to Ansa Beta CAE mesh generator. The cavity in-between pores and cubic shell is filled with solid. (Right) the pore shells and cubic confinement are deleted and a solid mesh of a foam structure is imported in Abaqus

4.2 **Boundary conditions**

The meshed specimens were imported to commercial explicit FE software [119]. Every side of the specimen was confined by shell plates (rigid bodies) (Figure

4-10) and loading was applied by imposing velocity and boundary conditions on the plates. In order to ensure plate to specimen contact a small compressive hydrostatic load was applied by the confining plates, prior to loading simulations. The contact settings (surface to surface contact algorithm) between the plates and foam would only allow for the specimen and plate nodes to slide tangentially and frictionless to the plates but separation was not allowed in the normal direction. The plates had no contact defined as to each other. General contact algorithm [120] was used for the internal interactions of the foam.

Loading was applied by imposing velocity on opposing plates. The velocity would correspond to the targeted strain rate in the order of 10^{-2}. The rest of the plates were constraint by imposing a linear relation for displacements of opposing faces. Boundary conditions were applied on lateral faces, imposing that opposite lateral faces moved by uniform displacements, perpendicular to the faces and of equal and opposite amount.

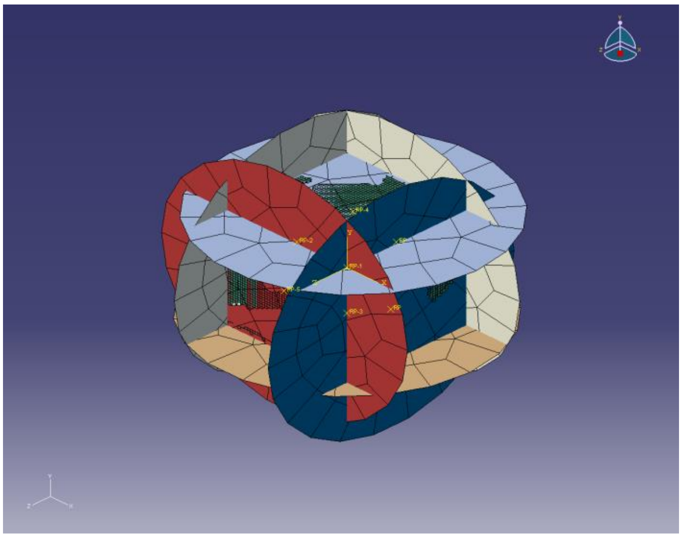

Figure 4-10 FE foam specimens were confined by shell plates to which boundary conditions were applied

4.3 **Material models**

The parent material of the structure was sintered Ti powder with 10 % micro porosity. The parent material was experimentally tested in quasi static compression and tension (Figure 4-11). A standard J_2 plasticity model was used to model the parent material behaviour. However two material models were compared for the simulations: the J_2 plasticity [121, 122] and the Gurson [123, 124], [125] model. The Gurson model accounts for some porosity embedded within the material matrix. To obtain the values for the fully dense material the yield condition equation of the Gurson model was reversely solved using commercial solving code [115]. The projected stress values for the fully dense material were increased by 12 % in comparison to those for the sintered powders [101] .

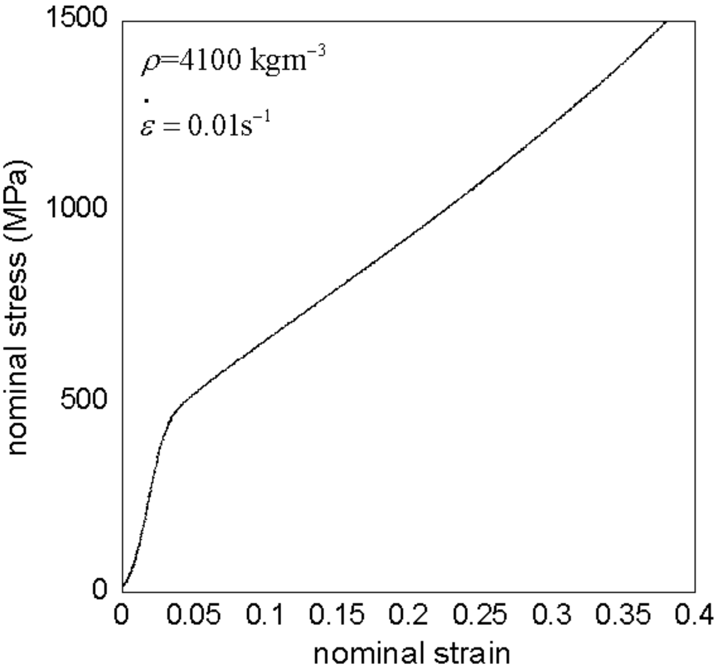

Figure 4-11 Compressive response of sintered Ti powders at strain rate of $\dot{\varepsilon} = 0.01\mathbf{s}^{-1}$ also included in (Figure 3-6) for 4100 Kgm^{-3} $(\bar{\rho} = 0.9)$. [101]

4.4 **Homogenised model**

Virtually generated foam structures were subjected to uniaxial, biaxial and triaxial loading modes. The macroscopic responses were used to calculate $\hat{\sigma}$, $\hat{\varepsilon}$ (eq 4-6 – 4-13) based on a model proposed by Deshpande and Fleck [74]. The proposed model accounts for the effect of porosity that consequently allows deformations with volume change. The produced shape is elliptic where α defines the aspect ratio of the ellipse. The case where α = 0 reduces $\hat{\sigma}$ το σ_{eq} and the J_2 theory for solids is recovered. The properties Y and α can be measured by a compression test.

$$\nu = 0.16 \tag{4-6}$$

$$\alpha = 3\left[\left(\frac{0,5-\nu}{1+\nu}\right)^{0,5}\right] = 1,624 \tag{4-7}$$

$$\sigma_m = \frac{\sigma_1+\sigma_2+\sigma_3}{3} \tag{4-8}$$

$$\sigma_{eq}^2 = \frac{1}{2}((\sigma_1-\sigma_2)^2+(\sigma_1-\sigma_3)^2+(\sigma_3-\sigma_2)^2) \tag{4-9}$$

$$\hat{\sigma}^2 = \frac{1}{\left(1+\left(\frac{\alpha}{3}\right)^2\right)}\left[\sigma_e^2+\alpha^2\sigma_m^2\right] = Y_u \tag{4-10}$$

$$\varepsilon_m = \frac{\varepsilon_1+\varepsilon_2+\varepsilon_3}{3} \tag{4-11}$$

$$\varepsilon_{eq}^2 = \frac{1}{2}\left((\varepsilon_1-\varepsilon_2)^2+(\varepsilon_1-\varepsilon_3)^2+(\varepsilon_3-\varepsilon_2)^2\right) \tag{4-12}$$

$$\hat{\varepsilon}^2 = (1+(\alpha/3)^2)[\varepsilon_e^2+\frac{1}{\alpha^2}\varepsilon_m^2] \tag{4-13}$$

Where ν is the Poison’s ratio, σ_{eq} = equivalent stress, σ_m = mean stress, σ_1, σ_2, σ_3 = principal stresses, ε_{eq} = equivalent strain, ε_m = mean strain, $\varepsilon_1, \varepsilon_2, \varepsilon_3$ =

principal strains, the parameter α defines the aspect ratio of the ellipse and Y_u is the uniaxial yield strength.

The data needed for the model were obtained from FE predictions for a foam of density ρ=1625 kgm^{-3} $(\bar{\rho} = 0.36)$.

4.5 Results

FE specimens of different size were modelled to investigate the effect of size to scatter in the compressive response. Each cubic specimen was subjected to compressive loading in FE simulations, from 3 different directions.

Each virtual cubic compression specimen was subjected to three simulations each corresponding to a different direction. The scatter in the response of different directions from the average value is shown in comparison to the experiment results (from the previous chapter) in Figure 4-12 as a function of cell size. The cell size was defined by the amount of pore sets following the selected distribution (step 3 Figure 4-2). The average value in the response of each specimen was in good agreement with experiments. Scatter was reduced and agreement was improved with increasing specimen size. However the increase of computational cost was disproportionally higher to the amount of improvement.

Elements of different size were used to mesh foam specimens. The specimens were subjected to quasi static compressive loading using FE and the predictions for the maximum Von Mises stress at a location on the specimen was compared for a strain of 0.03. Convergence was achieved for element sizes smaller than ~0.03 mm

(Figure 4-13). The element size of 0.03 mm corresponds to a ratio of active volume to nodes of 2.12e-05 mm^3/node. Active volume is the solid part of the foam specimen.

Figure 4-14 shows the predicted elastic modulus and poisons ratio at $\varepsilon = 0.2$ axial strain. The model results are compared with logarithmic fits of experimental data scaling with density. The exponent of the power law describing the dependence of Young's modulus on relative density is 3.28 [101]. Predictions agree well with the experiment data fits.

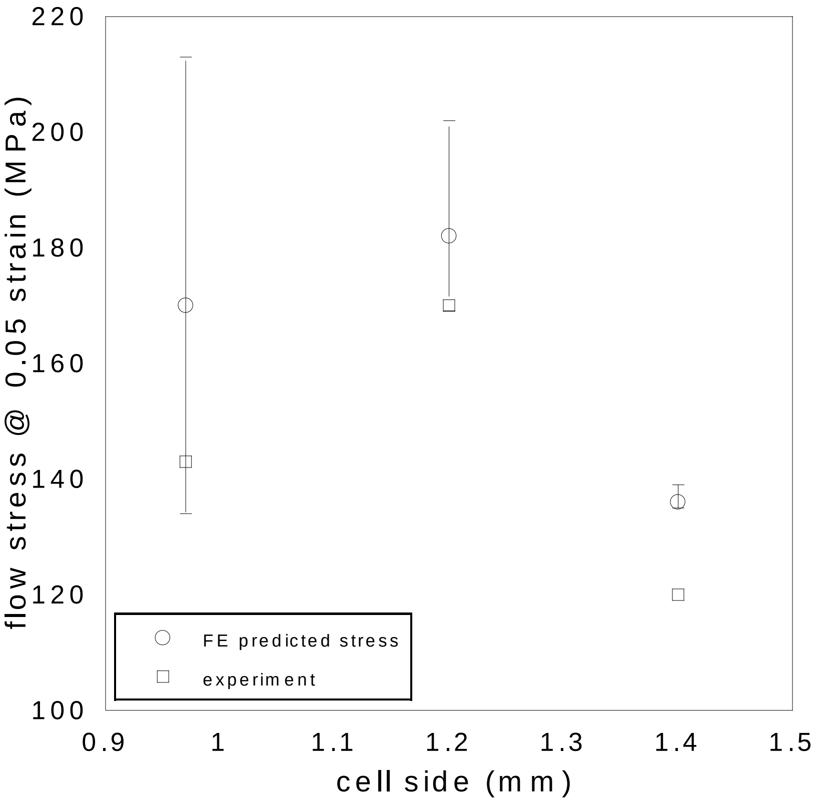

Figure 4-12 Cubic specimens of different sizes were subjected to FE predictions for compressive loading in three directions. A comparison is shown between different directions and the average value in the predicted response of virtual specimens as a function of specimen size. The average values are also compared against compression experiments. .

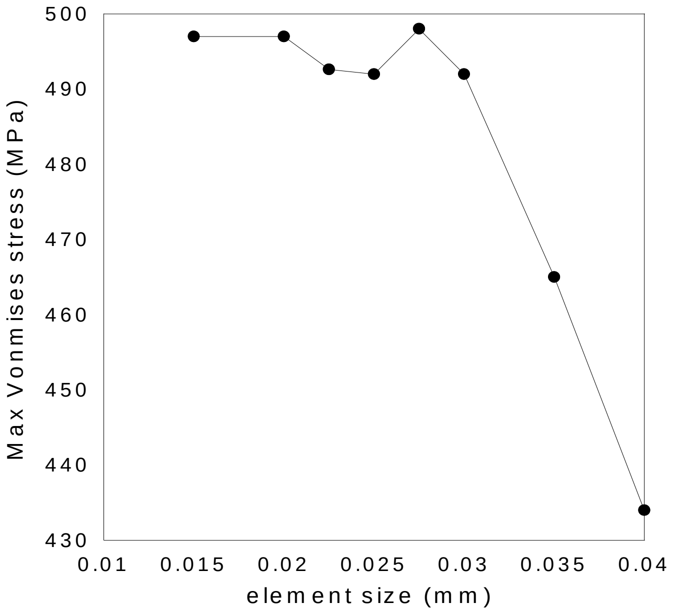

Figure 4-13 Mesh convergence is studied using different element sizes to mesh a foam specimen under compressive loading. The maximum Von Mises stress is taken at a certain point.

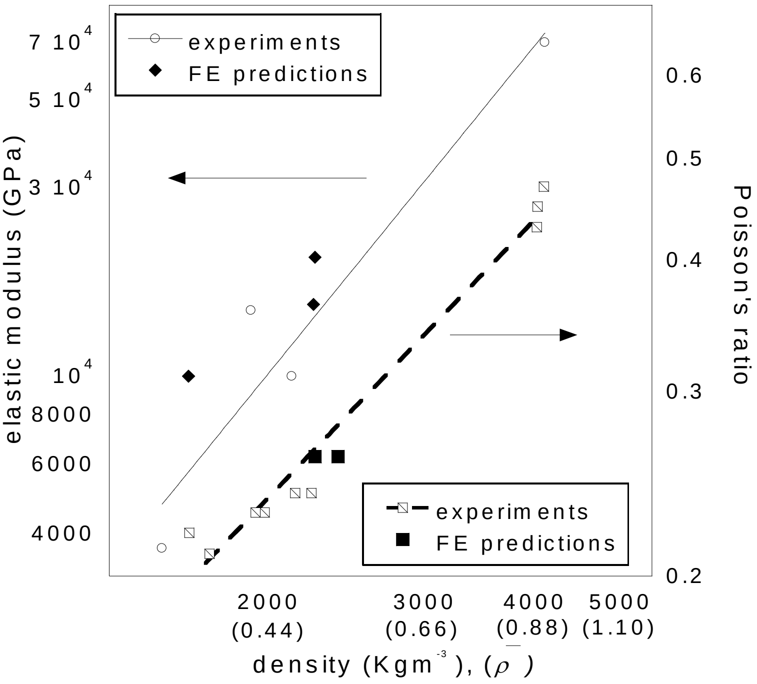

Figure 4-14 Experimental results of elastic modulus and Poisson's ratio (at 0.2 axial strain) in comparison with prediction for virtual foam simulations.

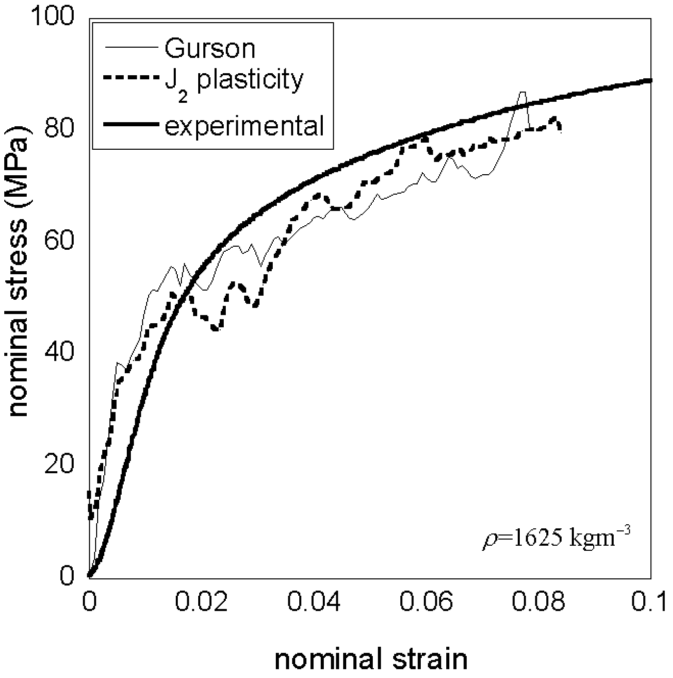

Figure 4-15 Comparison of uniaxial compression experiment with model predictions for virtual foams of density ρ=1625 kgm^{-3} $(\bar{\rho} = 0.36)$ using a standard J_2 plasticity and the Gurson [120] material model for the parent material of the structure.

Figure 4-15 compares the compressive response of foam of density ρ=1625 kgm^{-3} between two plasticity models used for the parent material of the foam and experimental data. The Gurson model and a standard J_2 incremental plasticity model are used for the parent material of the structure. The response in all cases is an elastic region followed by plastic deformation and densification with hardening. All three cases do not present with quantifiable difference up to the strain of interest $\varepsilon = 0.05$. The J_2 plasticity model was used for all of the following cases.

Biaxial compression-tension loading was applied on virtual specimens. Compression and tension loads were simultaneously applied on vertical sides of the specimen Figure 4-16. The response on both directions is elastic followed by a plastic region. The compressive plastic region is characterised by hardening while the tensile plateaus up to a strain of 0.14.

Figure 4-17 compares uniaxial and hydrostatic compression and tension simulations of a virtual foam of density of ρ=2244 kgm^{-3} $(\bar{\rho} = 0.49)$. The material response consists of a linear elastic section and a plastic region. Under compressive loading the material densifies with hardening. Under tensile loading the material hardening occurs only up to strains of $\varepsilon = 0.05$-0.06.

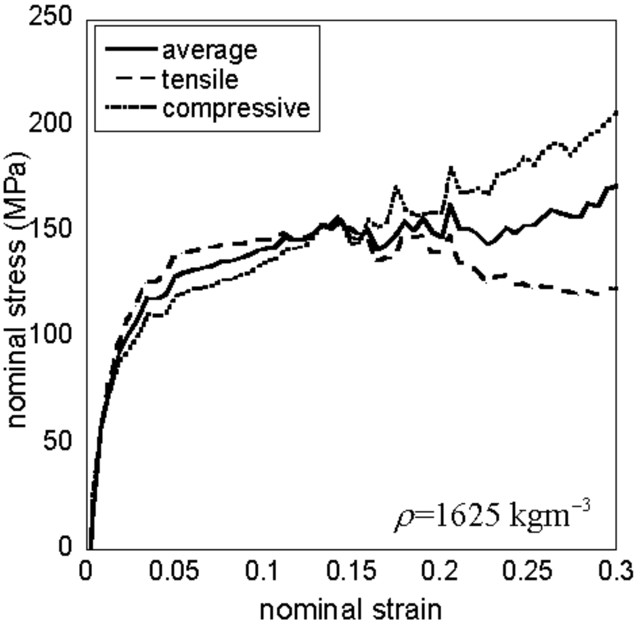

Figure 4-16 Tensile and compressive loading were simultaneously applied to vertical sides of the virtual specimen ρ=1625 kgm^{-3} $(\bar{\rho} = 0.36)$

Figure 4-18 shows the flow stress surface probed for the basic loading regimes. The stress response is taken at strain $\varepsilon = 0.05$ for foam of density of ρ=1625 kgm^{-3} $(\bar{\rho} = 0.36)$. The specimen was of side of ~1 mm. Each loading mode was repeated for each direction of the cubic specimen. The scatter is compared with the average response. The material presents higher stress response under compressive loading in comparison to tensile.

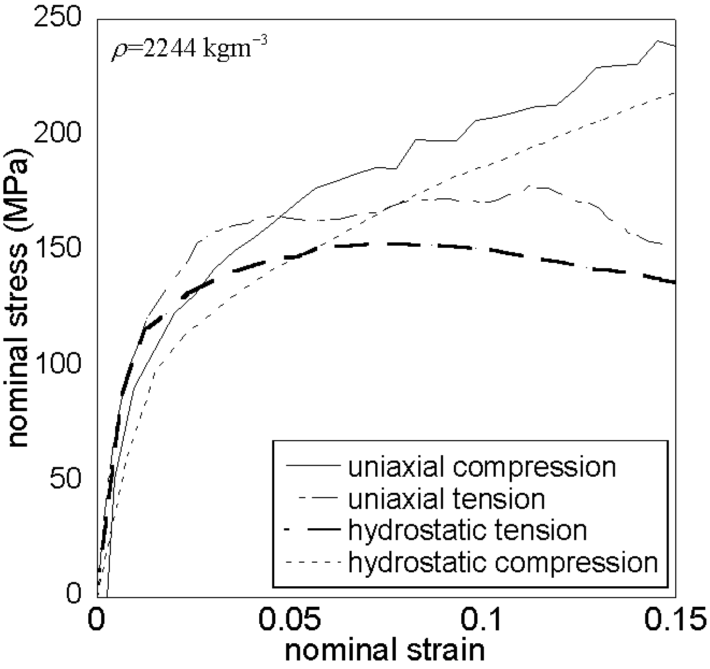

Figure 4-17 Comparison of uniaxial and hydrostatic loading modes for virtual foam of density ρ=2244 kgm^{-3} $(\bar{\rho} = 0.49)$.

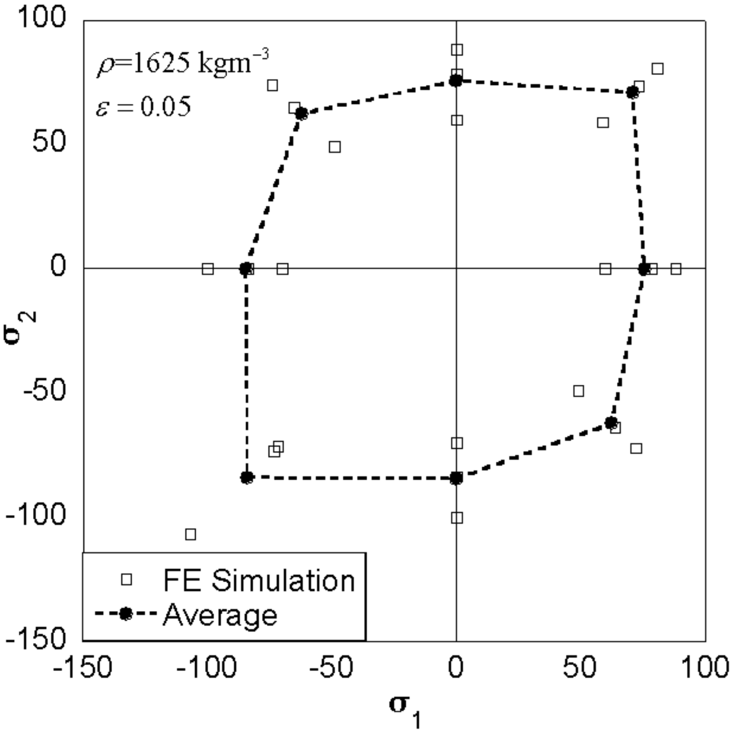

Figure 4-18 Stress surface in principle stresses space, predicted by modelling virtual foam specimen of density ρ=1625 kgm^{-3} $(\bar{\rho} = 0.36)$, the stress response scatter for each loading mode is compared.

Figure 4-19 (a) compares the compressive stress response of virtual specimens of various densities to experimental data fitted by a logarithmic law. The virtual specimens were cubic of sides 0.97-1.4 mm and were subjected to uniaxial compressive loading. Each cubic specimen was subjected to uniaxial compression simulations by applying the load on opposing sides. The simulation was repeated for each axial direction of the specimen to investigate the effect of scatter in the response. Figure 4-19(a) shows the average response for each density. The scatter did not significantly vary with specimen density but only with specimen size (Figure 4-12). The exponent of the power law describing the dependence of Yield stress on relative density was found 1.98 for the virtual foams and in good agreement with the experimental values that was 2.

Figure 4-19 (b) compares the response of two virtual foam specimens of densities ρ=1625 kgm^{-3} $(\bar{\rho} = 0.36)$ and ρ=2244 kgm^{-3} $(\bar{\rho} = 0.49)$ at strain of $\varepsilon = 0.05$. The stress surfaces were probed by simulating different loading modes for each of the densities. The effect of density in the stress response at different modes is investigated. The flow stress surface scales with density in all modes. The compressive response remains higher than the tensile regardless of density. Experimental data for compression tension and shear for a foam of density ρ=1625 kgm^{-3} $(\bar{\rho} = 0.36)$ are compared with predictions. The agreement is less for tension and shear rather than in compression. The models did not include any failure criterion. The cubic specimen side size was of ~1 mm Figure 4-12

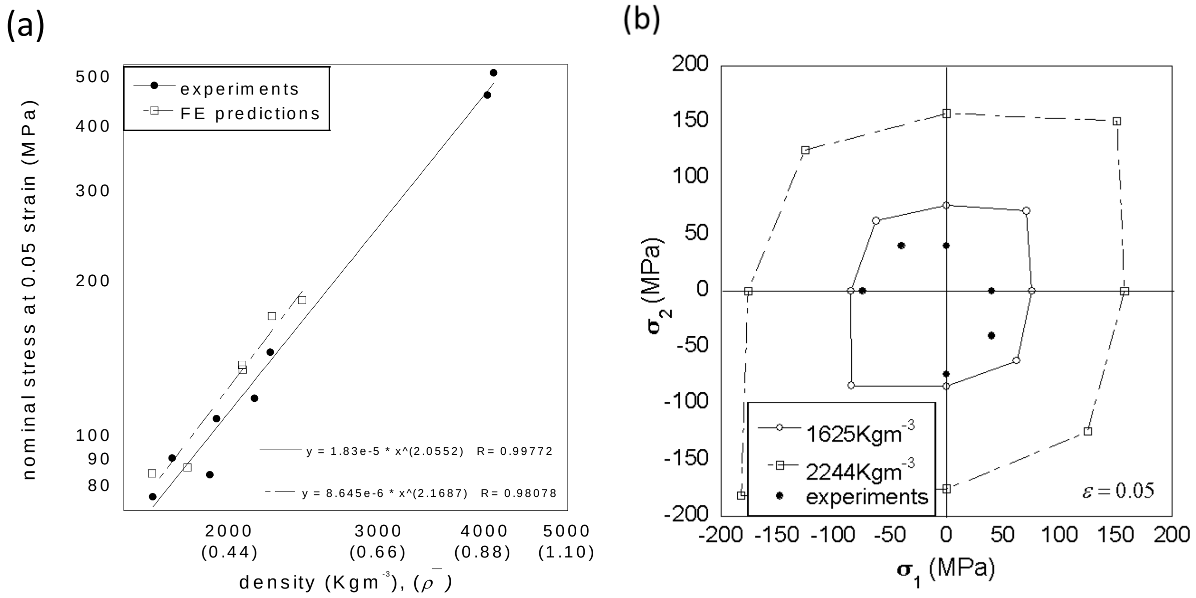

Figure 4-19 (Left) Comparison of experiments data at flow stress as a function of density and FE predictions of cubic specimens of side sizes of 1-1.4 mm. (Right) Averaged predicted stress surfaces for two densities of virtual foams corresponding to ρ=1625 kgm^{-3} $(\bar{\rho} = 0.36)$ and 2244 kgm^{-3} $(\bar{\rho} = 0.49)$ FE simulations for the basic loading modes were conducted. Experiment values for tension compression and shear are included for a foam of density ρ=1625 kgm^{-3} $(\bar{\rho} = 0.36)$ at strain of $\varepsilon = 0.05$.

Figure 4-20 shows the macroscopic stress response in (σ_m, σ_{eq}) space based on a model proposed by [74] for a strain $\hat{\varepsilon} = 0.01$. The data points were confined in an envelope using an elliptic function (4-10) for values of Y_u and α, 120 MPa, 70 MPa and 1.6 respectively. Data for simulations under uniaxial, biaxial and triaxial loading modes are included for a foam of density of ρ=1625 kgm^{-3} $(\bar{\rho} = 0.36)$. Specimen size was of ~1 mm. The data points are included in the region bounded by the two ellipses for the chosen values of Y_u and a.

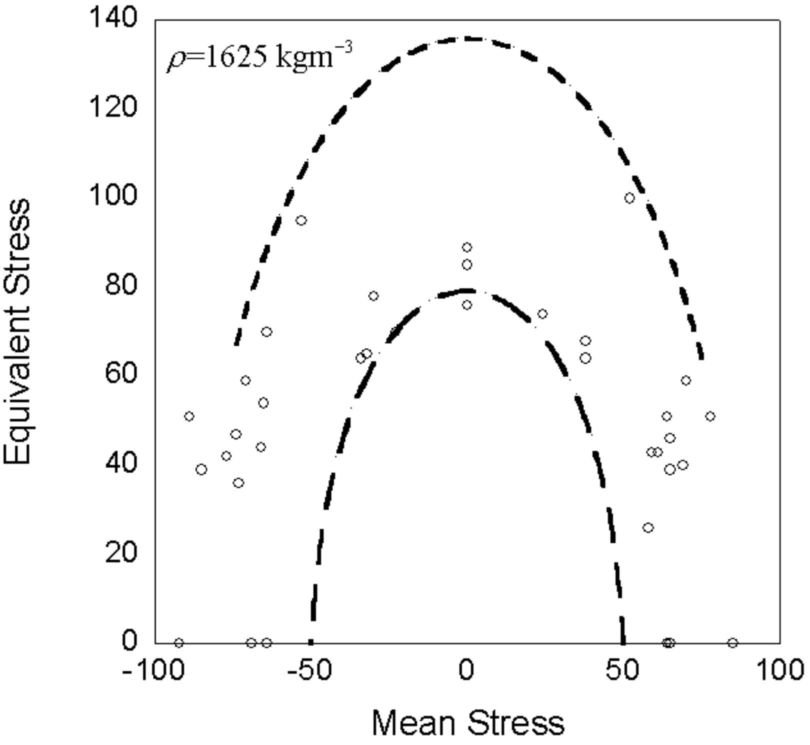

Figure 4-20 Stress response for uniaxial, biaxial and triaxial loading modes for virtual foam of density ρ=1625 kgm^{-3} ($\bar{\rho} = 0.36$) at strain $\hat{\varepsilon} = 0.01$. The FE prediction data points are fitted using the [74, 84] constitutive relations.

4.6 **Discussion**

Voronoi polyhedrals were used for the generation of irregular foam geometries. Voronoi polyhedral are usually used as shell cells of closed-cell high porosity foams [126, 127]. However this chapter presents the use of 3D Voronoi polyhedrals as space-holders around which the material forms open cell geometry. The method allows for statistical control of various foam features and is able to capture microstructural effects such as irregularity and texture of real foams. The method was employed to replicate Ti foams of densities ρ=1625-2244 kgm^{-3} ($\bar{\rho} = 0.36$ - $\bar{\rho} = 0.49$). A pore size distribution was followed [101] (Figure 4-5) for the polyhedral sizes so that to replicate existing foam structures. Various densities of virtual specimens were produced and modelled.

The geometrically representative specimen size was defined as the required volume around a given set of pores that would result to the target porosity (pore to specimen volume ratio) (eq.4-5). Scatter in macroscopic response of FE predictions reduced with increasing virtual specimen sizes. Effects such as deformation induced anisotropy [106] due to internal structure interactions are less pronounced in larger cell sizes. Computational time significantly increased with increasing volume. In the current study the FE specimen side to average pore diameter ratio (250 μm) was chosen to be at least 3. Drugan and Willis [128] suggests two inclusion diameters at most are sufficient for an RVE for modelling composites while Ostoja-Starzewskiin analysis shows that this ratio is problem-dependent in heterogeneous materials. [129]

Singh R. et al modelled foam geometries of similar geometry and density using meshes produced directly from XMT scans. Pore diameter was of d=350-400 μm and performed a study on the influence of size to yield stress and Youngs modulus. Past the specimen size of 1.1 mm and a ratio of 3 the values stabilized. The specimens used for simulations were of pore size to specimen edge ratio of 4-5. However a variation in properties in different directions was still observed and was assigned to preferential direction of pores. [7]

H. Shen et al modelled low density foams using spherical voids and suggested that ‘’a set of small domain RVEs can be used instead, as long as the average of the small domains provides a convergent result’’ This suggestion was based on a definition of RVE by Drugan and Willis 1996 [98], which defines it as “the smallest material volume element of the composite for which the usual spatially constant 'overall modulus' macroscopic constitutive representation is a sufficient accurate model to represent mean constitutive response." [130, 131]

A combination of displacement and contact constraints was imposed on the plates. The contact algorithm did allow for tangential movement between material and shell plate nodes but no separation in the normal direction. Additionally; boundary conditions were applied on lateral faces, imposing that opposite lateral faces moved by uniform displacements, perpendicular to the faces and of equal and opposite amount. The proposed introduction of boundary conditions through confining plates allows for applying boundary conditions on opposing faces without node readjustment (4.1 Boundary conditions).

Two material models were examined for use in modelling the parent material. Standard J_2 plasticity model was used that accounted only for deviatoric response while the Gurson model accounted for both the hydrostatic loading and deviatoric dependent responses. Results (Figure 4-15) suggest that for medium porosity foams strained up to $\varepsilon = 0.05$, hydrostatic effects within the parent material have insignificant influence to the macroscopic response.

Macroscopic elastic properties and Poisson ratio were captured by the mesoscale model and compared well with experimental results. The stress response surface was probed for various loading regimes (Figure 4-18). The chosen specimen size was of the minimum representative volume (~1 mm^3) in order to save on computational time. Therefore scatter effects were observed (Figure 4-12). Values of the predicted stress response are in increasing agreement to experiments with increasing specimen size.

Compression simulations were performed to predict stress scaling with density at a strain of ε=0.05. Six virtual foam specimens were produced and each was subjected to 3 compression simulations (one for each side). The stress response was then averaged for each specimen. Small cell size specimens responded with large scatter in comparison to their average stress value. However their average value was in good agreement with experiments Figure 4-19. Ideally more virtual specimens of larger cell size would be considered for each density. Computational time was a significant restriction.

The compressive stress response scaling with density compares very well with the experimentally obtained data. The exponent of the power law describing the dependence of Yield stress on relative density was found 2.1 for the virtual foams and in good agreement with the experimental values that was 2 (Ashby and Gibson predict coefficient of 1.5) [46]. The Pearson's correlation coefficient for the fitted power law was 0.997 and 0.98 for experiments and simulations respectively. The averaged compressive responses for each density predicted well the yield stress of the material. This method potentially provides an improved and lower cost solution to alternative methods found in literature. [7]

The stress response is scaling with density in all loading modes (Figure 4-19b). Stress surface tends to be quadratic with higher response values in compression rather than in tension. Nevertheless the study was confined to strains of $\varepsilon = 0.05$. Comparison between the experiments and predicted values (Figure 4-19b) for the lower density foam ρ=1625 kgm^{-3} $(\bar{\rho} = 0.36)$ show very good agreement in compression. Less agreement was observed in tension and shear as no failure model was applied for the parent material. The failure effects were not modelled in

FE predictions. These effects are likely to be more pronounced in tensile modes and larger strains. The macroscopic response of the virtual foams was approached using the constitutive relations developed for low density foams by Deshpande and Fleck [74] (Figure 4-20). The material response was captured within a band of 70-120 MPa for various loading modes. The small specimen size (1 mm^3) in addition to the lack of a failure model are possible reasons for the scatter. The scatter is more pronounced in triaxial loading modes.

This chapter was focused on developing a method for virtually generating irregular geometries that can capture the structural characteristics of irregular foams.

The method was used to produce Ti foam geometries and predict quasi static macroscopic responses using FE simulations. The method can potentially assist understanding and optimisation of foam behaviour.

4.7 **Conclusions**

The method proposed in this chapter for producing foam structures was able to capture geometrical characteristics of irregular foam geometries and produce specimens for FE simulations. FE predictions of compressive loading of structures of different density were able to reproduce mechanical characteristics of Ti foams of this type and behave in good agreement with experimental data.

The material model did not include failure for the parent material and therefore were unable to predict failure of the specimen. Predictions were less accurate on loading modes that have pronounced failure effects such as tension or shear.

The influence of this type of porosity on the material properties was captured in macroscopic material behaviour for compressive responses and scaling with density. Agreement was significantly increased with increasing specimen size.

5 Modelling high rate response of Ti foam structures

Summary

Ti foams previously investigated experimentally are found to be strain rate sensitive, with both the yield stress and the strain hardening increasing with applied strain rate, and the strain rate sensitivity is more pronounced in foams of lower relative density. This chapter is focused in finite element simulations modelling explicitly the material’s microstructure at the micron length scale, via a 3D Voronoi tessellation method. Low and high strain rate simulations were conducted in order to predict the material’s compressive response, employing both rate-dependant and rate-independent constitutive models. Results from numerical analyses suggest that the primary source of rate sensitivity is represented by the intrinsic sensitivity of the foams parent material. However results suggest that inertial effects at micron length scale also influence responses.

5.1 FE simulations of the compressive response

Abaqus was employed to perform static and dynamic simulations of the foams response. The microstructure of the foams was reproduced using a random 3D Voronoi tessellation of the specimen's space. A cube of material was subdivided in randomly-shaped Voronoi cells and a number of these cells was flagged as pores (as described in the previous chapter). The density of the seed points was chosen in order to ensure that the distribution of pore sizes followed the distribution measured via X-ray tomography. The solid material defined by the difference between the specimen domain and the pore domains was meshed with linear tetrahedral, wedge and hexahedral elements by a commercial meshing tool [120, 132]. The representative volume element for the geometrical characteristics was defined as the minimum volume (for the target porosity) that can include a set of pores with size characterized by a probability distribution approximately equal to that measured via X-ray tomography.

Compressive loading was applied by imposing a displacement on the top and bottom faces of the mesh. Boundary conditions were applied on lateral faces, imposing that opposite lateral faces moved by uniform displacements, perpendicular to the faces and of equal and opposite amount. J_2 incremental plasticity was used to model deformation of the foams parent material, and the strain hardening was chosen to be isotropic and was calibrated against the data for the sintered powders of density 0.9 shown (Figure 5-1, Figure 5-2). Both rate-sensitive and rate-insensitive models were used. The rate sensitivity was described by a power-law dependence of the flow stress upon the applied strain rate, and was deduced from the compressive stress versus strain curves obtained by testing the parent material at different strain rates; the exponent of the power-law expression (of type $\sigma_{0.2} = \Psi \dot{\varepsilon}^{m}$ where Ψ is a material constant and m a material dependent exponent) was found to be 0.016. Figure 5-3 and Figure 5-4 display samples of the mesh and the FE predictions of the macroscopic compressive response at low (~0.01 s^{-1}) and high (~10^3 s^{-1}) strain rate, for foams of two selected densities.

FE simulations on different densities were employed to investigate the macroscopic compressive response of the structures at high rates of deformation (

Figure 5-6). The specimens and method for the simulations was the same as the one developed in the previous chapter. Strain rate sensitivity was included in the J_2 material model. Again scatter effects were less pronounced with increasing specimen size. Predictions were scaling with density in agreement with the experimental fit. However predictions made with small size specimens (cubic edge=0.97 mm) displayed scatter around their average value.

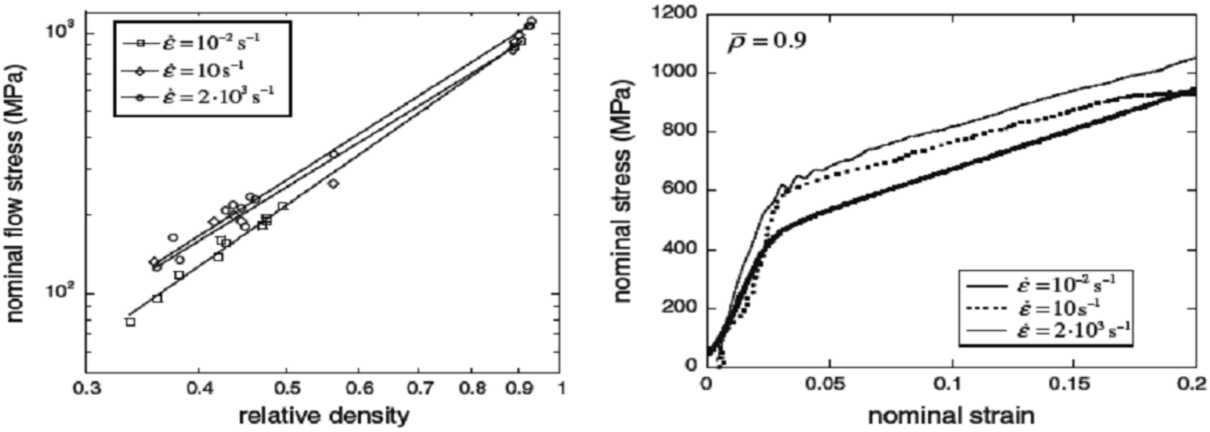

Figure 5-1 (Left) Measured flow stress (at a plastic strain of 0.2) as a function of foam density, in low, medium and high strain rate experiments. (Right) Compressive nominal stress versus strain response of sintered powder of relative density 4100 Kgm^{-3} ($\bar{\rho} = 0.9$) at low, medium and high strain rates

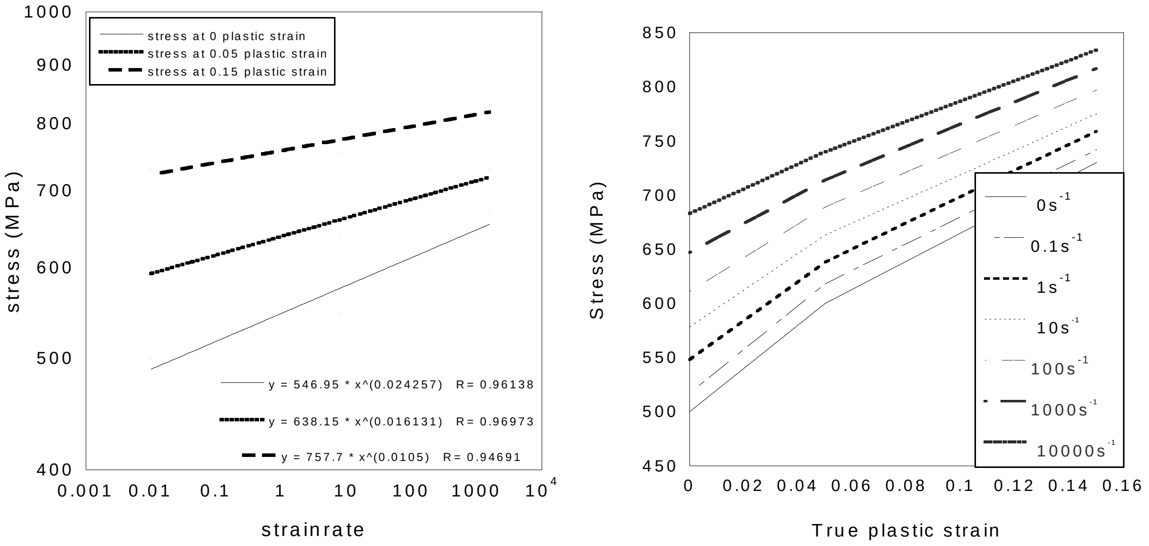

Figure 5-2 (Left) Fit on data from experiments on sintered powders (parent material 4100 Kgm^{-3} $\bar{\rho} = 0.9$) showing stress to strain rate. Each fit is for true plastic strains at 0, 0.05 and 0.15 at 3 different strain rates. (Right) True stress true plastic strain curves for different strain rates. Based on the fits on data from experiments the points for 7 different strain rates were extrapolated

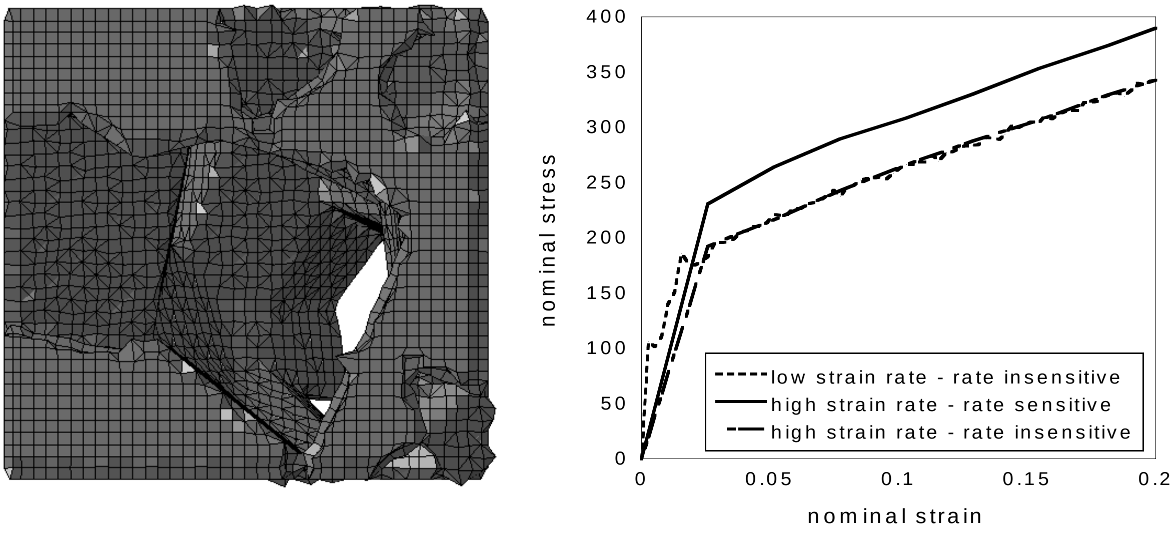

Figure 5-3. Left: mesh of a virtual foam of relative density 2244 Kgm^{-3} ($\bar{\rho} = 0.49$) Right: FE predictions of the macroscopic material responses for strain rates of 0.01-500 s^{-1}

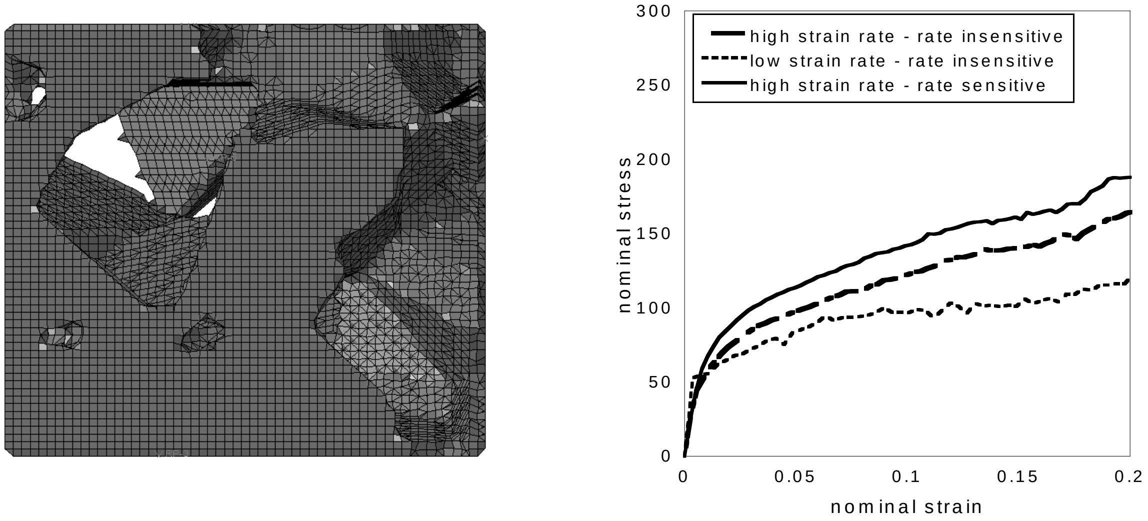

Figure 5-4. Left: mesh of a virtual foam of relative density 1625 Kgm^{-3} ($\bar{\rho} = 0.36$). Right: FE predictions of the macroscopic material responses for strain rates of 0.01-1500 s^{-1}.

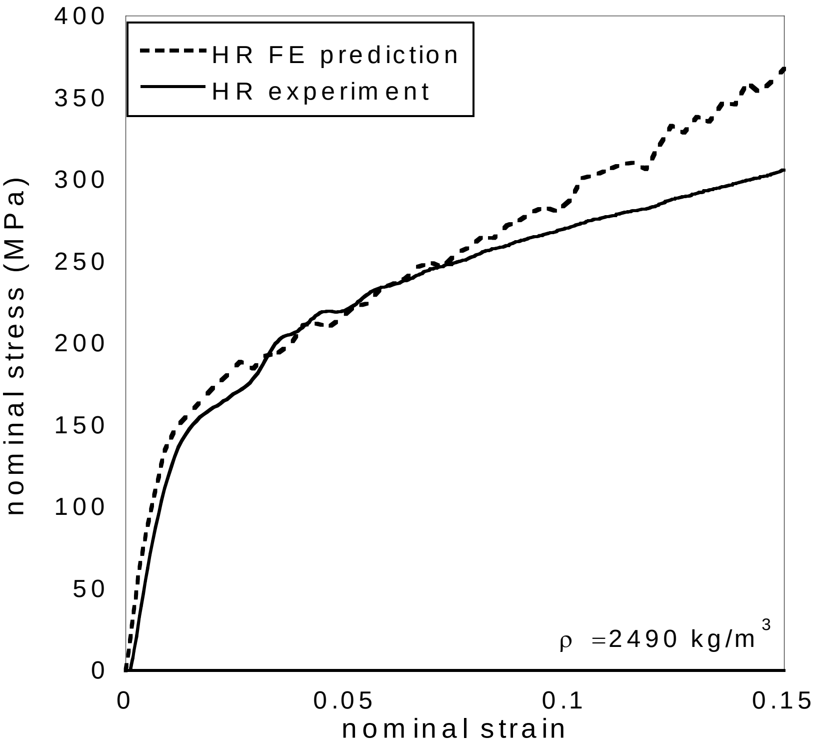

Figure 5-5. Comparison between a HR compression experiment and FE prediction of the macroscopic material responses for a foam of 2490 Kgm^{-3} ($\bar{\rho} = 0.55$) for strain rate of 1500 s^{-1}.

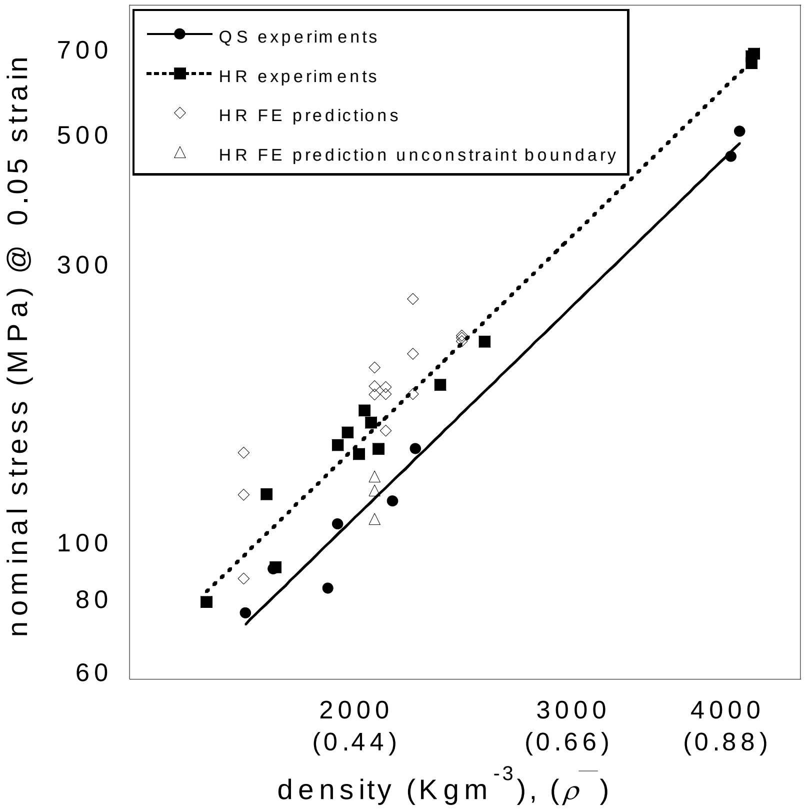

Figure 5-6. Comparison of experimental measurements of flow stress as a function of density and predictions by models for virtual foams with different cell volume at low and high strain rates $\dot{\varepsilon} = 10^{-2}$, $2x10^3 s^{-1}$

5.2 **Discussion**

At all compressive strain rates, foams initially deform elastically and subsequently collapse plastically further to followed by flattening of the macro-pores perpendicularly to the loading direction. Correspondingly, strain hardening and densification is observed in the macroscopic response, due to progressive self-contact of the internal surfaces of the pores. The predicted macroscopic strain hardening is due partially to pore self-contact and partially to the intrinsic strain hardening characteristic of the parent material. At compressive axial strains in the range 0.15–0.3, micro-cracking is observed. At sufficiently high axial strains the strain hardening rate increases for these foams, due to material densification by complete closure of the pores (densification).

The static and dynamic mechanical response of the foams is sensitive to relative density; elastic modulus, flow stress and strain hardening rate increase with the foam relative density. Comparisons of the measured stress–strain responses at different strain rates revealed that the material response is sensitive to the applied strain rate. Sintered Ti powder 4100 Kgm^{-3} ($\bar{\rho} = 0.9$) displays an increase of the yield stress with strain rate comparable to those observed by other authors [47, 80, 133] for fully dense crystalline Ti alloys. This elevation in yield stress was measured to be of 13 % as the strain rate was varied from 0.01 to 2000 s^{-1}; for these sintered powders, the measured strain hardening rate is independent of the applied strain rates. Foams ($\bar{\rho} = 0.3 - 0.5$) display an elevation of both yield stress and strain hardening rate with increasing applied strain rate. Foams with relative density 1486 Kgm^{-3} ($\bar{\rho} = 0.33$) displayed an elevation of 32 % in flow stress (at a plastic strain of 0.2) as the strain rate was varied from 0.01 to 2000 s^{-1}. In more quantitative terms, the measured flow stress (at a plastic strain of 0.2) $\sigma_{0.2}$ versus imposed strain rate ($\dot{\varepsilon}$) data could be fitted by a power-law relation of type $\sigma_{0.2} = A\dot{\varepsilon}^{m}$, where A and m were a function of relative density. The measured exponents (*m)* were found to be 0.027 and 0.017 for relative densities of 0.35 and 0.9, respectively.

Figure 5-6, 6 shows a good agreement of the predicted high rate response to that of the fitted experiment values. The data points for densities of 1577-2253 Kgm^{-3} ($\bar{\rho} = 0.35 - 0.5$) were fitted using a power law with exponents for experimental data of 1.92 and for FE predictions of 1.72. A specimen without constraint boundary conditions is compared with the specimens were a linear relation was imposed on opposing faces. The response of the unconstraint specimen was significantly reduced. Scatter was most likely the result of the small size of virtual specimens that cause anisotropic effects and the lack of failure within the material model.

FE predictions help understanding of the origin of strain rate sensitivity. Figure 5-3 shows that for foams of relatively high density the low and high strain rate macroscopic responses coincide in the case where intrinsic rate sensitivity of the parent material is not modelled. It may be deduce that the effects of inertia at a micron length scale are negligible for foams of this density. In contrast, for foams of lower density, such as that associated to the mesh and data in Figure 5-4, the FE-predicted high strain rate response is stronger than the low strain rate response in absence of rate sensitivity of the parent material. Modelling such sensitivity gives an even stronger macroscopic high strain rate response. It may be deduce for foams of lower density that inertial effects at the micron level contribute positively to the macroscopic rate sensitivity of the material.

5.3 Conclusion

The Ti foams under investigation displayed strain rate sensitivity, with both yield stress and strain hardening rate increased with increasing strain rate. Strain rate sensitivity appears to be more pronounced for foams of lower relative density: numerical analyses suggest that the primary source of rate sensitivity is represented by the intrinsic sensitivity of the sintered powders, however micro-inertial effects intervene for rapid loading of foams of lower relative density.

6 Conclusions – future work

Summary

The behaviour of Titanium foams was studied under different states of loading. Strain rate sensitivity, structure geometry and various loading modes where examined on both existing and virtually generated foam structures. A method to virtually produce foam structures was developed in order to replicate the types of foams under investigation. Finite element models were employed to simulate tests and compared with experimental results. Predictions were used to assist in understanding material behaviour and to compliment experimental observations by simulating loading modes that are difficult to perform experimentally. The conclusions of this study are summarised in this chapter and further development is suggested.

6.1 **Experimental characterisation of Ti foams**

- Porous solids made from commercially pure Ti powder were studied; the microstructure of these solids comprised (i) micro-pores (diameter 10 μm) of round, smooth shape, resulting from the incomplete sintering of the gaps between titanium powder particles and (ii) macro-pores (diameter >100 μm) of irregular shape and sharp corners, formed by the decomposition of the foaming agent. The sintered Ti powder tested presented only micro- porosity, while the sintered Ti foams presented both micro- and macro-porosity.
- Upon loading in compression foams initially deform elastically and subsequently collapse plastically by flattening of the macro-pores perpendicularly to the loading direction. For the sintered powder (4100 $\mathrm{Kgm^{-3}}$, $\bar{\rho} = 0.9$), produced without binder and foaming agent, plastic collapse occurs by flattening of the micro-pores. The pore-flattening mechanism is accompanied by traverse strain; the Poisson's ratio is found to increase with the imposed axial strain at a rate depending on the foam density. At compressive axial strains in the range 0.15–0.3, micro-cracking is observed. At sufficiently high axial strains the strain hardening rate increases for these foams, due to material densification by complete closure of the pores. The densification strain increases as the foam relative density decreases.
- Upon loading in tension and shear foams performed in a brittle manner. The elastic deformations phase was shorty followed by failure. The sintered powder (4100 $\mathrm{Kgm^{-3}}$, $\bar{\rho} = 0.9$) material under tensile loading responded with an elastic and plastic phase. The strain hardening rate was insensitive to

imposed strain rate. However the plastic region was in the form of a plateau leading to material failure at nominal strains of around 0.15. The material around the micro pores is elongated at the direction of deformation. Macroscopic necking of specimen and microscopic necking of the material around the pores is followed by failure

- The mechanical response of the foams is sensitive to relative density; elastic modulus, yield stress and the strain hardening rate increase with the foam relative density. Comparisons of the measured stress–strain responses at different strain rates revealed that the material response is sensitive to the applied strain rate.
- Sintered Ti powder (4100 Kgm^{-3}, $\bar{\rho} = 0.9$) displays an increase of the yield stress with strain rate comparable to those observed by other authors [6–8] for fully dense crystalline Ti alloys. This elevation in yield stress was measured to be of 13 % as the strain rate was varied from 10^{-2} to $2x10^{3}$ s^{-1}; for these sintered powders, the strain hardening rate is independent of the applied strain rates.
- Foams (1486-2253 Kgm^{-3}, $\bar{\rho} = 0.33 - 0.5$) display an elevation of both yield stress and strain hardening rate with increasing applied strain rate. Relative strain rate sensitivity was found as a function of density. The strain rate sensitivity appears to be more pronounced for foams of lower relative density: foams with density of 1486 Kgm^{-3}, $\bar{\rho} = 0.33$ displayed an elevation of 32 % in flow stress (at a plastic strain of 0.2) as the strain rate was varied from 10^{-2} to 2×10^{3} s^{-1}. Deformation mechanisms observed via quasi-static in situ testing for the foams were insensitive to relative density. However increased porosity

in the foam microstructure in combination to the rough texture of the pores may result in inertial stress fields, affecting the deformation and failure mechanisms.

- The surfaces of the examined foams are highly textured due to the sintered powder particles used during manufacturing (Figure 3-1). SEM in situ observations show that deformation mechanisms involve pore flattening that leads to opposing surfaces folding and interacting (Figure 3-10). In addition post test SEM reveals smeared powder particles as well as cracks through the particles and necks.

  It could be argued that the ligaments and powder particles on the interacting surfaces are less constraint by inertia during quasi static interactions rather than in high rate. During quasi static interactions powder particles on interacting surfaces are more able to slide on the periphery of each other; rather than during high rate. During high rate interactions the ligaments and powder particles are additionally constraint by the effects of inertia on the lateral directions. The inertial effects add rigidity to the ligaments restricting the interacting powder particles from sliding around and bypassing obstacles. Ligaments that are interacting by partially intercepting powder particles; and would otherwise shift or move quasi statically by deformation of the ligaments; may be blocked by inertial constraints subsequently increasing the stress response. Higher porosity foams have larger open surfaces and therefore a larger number of surface interactions occurring during pore flattening and surface folding (e.g. $\varepsilon = 0.2$) (Figure 3-24). Therefore the effect is more pronounced in higher porosities and contributes positively to the relative strain rate sensitivity of the material. Quantifying the effect of surface roughness and strain rate on surface interactions for different densities will be a subject of future work.

6.1.1 Future Work

- This is not the only possible explanation for the enhanced strain rate sensitivity in foams compared to that observed in sintered Ti powders: further microscopic observations and modelling of the dynamic foam deformation and fracture should be conducted in order to aid interpretation of the observed strain rate sensitivity. Frictional effects in combination to inertial effects at micron scale, during high strain rate deformation may add to the enhancement in the material strain rate sensitivity for lower density foams.

6.2 **Modelling Ti foam structures**

- The method proposed for producing foam structures was able to capture geometrical characteristics of irregular foam geometries and produce specimens for FE simulations. FE predictions on structures of different density were able to reproduce mechanical characteristics of Ti foams of this type and behave in good agreement with experimental data.
- The influence of this type of porosity on the material properties was captured in macroscopic material behaviour for compressive responses and scaling with density. Agreement was significantly increased with increasing specimen size.
- However, the material model did not include failure for the parent material and therefore were unable to predict failure of the specimen. Predictions were less

accurate on loading modes that have pronounced failure effects such as tension or shear.

6.2.1 Future work

The method presented in chapter 4 for producing stochastic open cell structures can assist in investigating the effect of geometrical characteristics on the macroscopic mechanical properties. Pore surface roughness, pore sizes and orientation, failure and hardening in relation to density is the object of future work.

6.3 Modelling high rate response of Ti foam structures

- The Ti foams under investigation displayed strain rate sensitivity, with both yield stress and strain hardening rate increased with increasing strain rate. Strain rate sensitivity appears to be more pronounced for foams of lower relative density: numerical analyses suggest that the primary source of rate sensitivity is represented by the intrinsic sensitivity of the sintered powders,
- Results from FE predictions suggest that inertial effects intervene for rapid loading of foams of lower relative density. The structure of the foams adds to the strain rate sensitivity.
- Strain rates within the structure can vary significantly and can be up to two orders of magnitude higher than the macroscopic rate imposed.
- The strain rate sensitivity scaling with density is captured well by the virtual geometry models.

6.3.1 Future Work

Scatter in FE predictions due to size restrictions can be significant from small specimen sizes. Using equipment with high processing power would reduce the time and enable the use of larger specimens in order to reduce errors.

Further investigation around the effect of geometrical features on the porous material properties is the object of future work. Strain rate sensitivity in relation to structure and surface roughness would allow for more inside in how inertial mechanisms are triggered and how they can be enhanced or eliminated.

The method for producing foam geometries could potentially apply on different types of foam and materials. This study was limited in examining open cell Ti foams, however expanding this method on different materials is to be investigated in the future.

6.4 **Published work**

The content of this thesis was extracted from studies published (or in the process of being published) in refereed scientific journals or conference proceedings

Publications in refereed Journals

- P. Siegkas, V. L. Tagarielli, N. Petrinic, and L. P. Lefebvre, 2011, "The compressive response of a titanium foam at low and high strain rates," J Mater Sci vol. 46, pp. 2741–2747.
- Siegkas, P.; Tagarielli, V.L.; Petrinic, N.; Lefebvre, L.-P. 2012, Rate Dependence of the Compressive Response of Ti Foams. *Metals (special issue)*, *2*, 229-237.

Conference Paper

- P. Siegkas, V. Tagarielli, N. Petrinic, L. P. Lefebvre, 2011, Rate Dependency of the Response of Ti Foams in Compression. Proceedings of the 7th International Conference on Porous Metals and Metallic Foams held in Busan, Korea, September 18-21, (METFOAM 2011) p.6

7 References

[1] T. Ryan and G. Krovitz, 2006 "Trabecular bone ontogeny in the human proximal femur," *J Hum Evol*, vol. 6, pp. 591-602.

[2] Lorna J. Gibson, 2012, "The hierarchical structure and mechanics of plant materials," *J. R. Soc.*, vol. 9, pp. 2749-2766.

[3] J. W. G. Lutjering, 2007 *Titanium (Engineering Materials and Processes)*, 2nd ed. Springer.

[4] M. Donachie, 2000 *Titanium: a technical guide*, 2nd ed. ASM International, 2000, p. 381.

[5] C. Leyens and M. Peters, 2003 *Titanium and Titanium Alloys: Fundamentals and Applications*, 1st ed. Wiley VCH.

[6] M. Cervenka. (5 October 2000), The Rolls Royce Trent jet engine Plc., slide 24.

[7] R. Singh, P. D. Lee, T. C. Lindley, C. Kohlhauser, C. Hellmich, M. Bram, T. Imwinkelried, and R. J. Dashwood, 2010, "Characterization of the deformation behavior of intermediate porosity interconnected Ti foams using micro-computed tomography and direct finite element modeling," *Acta Biomaterialia*, vol. 6, pp. 2342-2351.

[8] L. J. Gibson, 2000, "Mechanical behaviour of metallic foams," *Annual Review of Materials Science*, vol. 30, pp. 191-227.

[9] E. Andrews, W. Sanders, and L. J. Gibson, 1999, "Compressive and tensile behaviour of aluminum foams," *Materials Science and Engineering: A*, vol. 270, pp. 113-124.

[10] G. J. Davies and S. Zhen, 1983/07/01 1983, "Metallic foams: their production, properties and applications," *Journal of Materials Science*, vol. 18, pp. 1899-1911.

[11] G. Ryan, A. Pandit, and D. P. Apatsidis, 2006, "Fabrication methods of porous metals for use in orthopaedic applications," *Biomaterials*, vol. 27, pp. 2651-2670.

[12] L.-P. Lefebvre and Y. Thomas2003 "Method of making open cell material," ed: Google Patents.

[13] J. Banhart and J. Baumeister, 1998 "Production methods for metallic foams," in *MATERIALS RESEARCH SOCIETY SYMPOSIUM PROCEEDINGS*, pp. 121-132.

[14] O. Lame, D. Bellet, M. Di Michiel, and D. Bouvard, 2004, "Bulk observation of metal powder sintering by X-ray synchrotron microtomography," *Acta Materialia*, vol. 52, pp. 977-984.

[15] D. C. Dunand, 2004, "Processing of Titanium Foams," *Advanced Engineering Materials*, vol. 6, pp. 369-376.

[16] R. Cirincione, R. Anderson, J. Zhou, D. Mumm, W. Soboyejo, and A. Ghosh, 2002, "An investigation of the effects of sintering duration and powder sizes on the porosity and compression strength of porous Ti–6Al–4V," *Processing and properties of lightweight cellular metals and structures*, p. 189.

[17] A. E. Markaki, V. Gergely, A. Cockburn, and T. W. Clyne, 2003, "Production of a highly porous material by liquid phase sintering of short ferritic stainless steel fibres and a preliminary study of its mechanical behaviour," *Composites Science and Technology*, vol. 63, pp. 2345-2351.

[18] J. C. Tan and T. W. Clyne, 2008, "Ferrous Fibre Network Materials for Jet Noise Reduction in Aeroengines Part II: Thermo-Mechanical Stability," *Advanced Engineering Materials*, vol. 10, pp. 201-209.

[19] P. Ducheyne,1987 "Porous flexible metal fiber material for surgical implantation," ed: Google Patents.

[20] D. C. Dunand, (2004), " Processing of Titanium Foams," *Adv. Eng. Mater.*, vol. 6, pp. 369–376.

[21] W. Niu, C. Bai, G. Qiu, Q. Wang, L. Wen, D. Chen, and L. Dong, 2009/08/01 2009, "Preparation and characterization of porous titanium using space-holder technique," *Rare Metals,* vol. 28, pp. 338-342.

[22] Z. Esen and Ş. Bor, 2007, "Processing of titanium foams using magnesium spacer particles," *Scripta materialia,* vol. 56, pp. 341-344.

[23] D. Kupp, D. Claar, K. Flemmig, U. Waag, H. Goehler, and I. Fraunhofer, 2002, "Processing of controlled porosity titanium-based materials," *ADVANCES IN POWDER METALLURGY AND PARTICULATE MATERIALS,* pp. 2-126.

[24] X. Zhang, R. Ayers, K. Thorne, J. Moore, and F. Schowengerdt, 2001, "Combustion synthesis of porous materials for bone replacement," *Biomedical sciences instrumentation,* vol. 37, p. 463.

[25] R. A. Ayers, D. E. Burkes, G. Gottoli, H.-C. Yi, F. Zhim, L. H. Yahia, and J. J. Moore, 2007, "Combustion synthesis of porous biomaterials," *Journal of Biomedical Materials Research Part A,* vol. 81A, pp. 634-643.

[26] C. Chu, C. Chung, P. Lin, and S. Wang, 2004, "Fabrication of porous NiTi shape memory alloy for hard tissue implants by combustion synthesis," *Materials Science and Engineering: A,* vol. 366, pp. 114-119.

[27] C. L. Chu, C. Y. Chung, P. H. Lin, and S. D. Wang, 2004, "Fabrication of porous NiTi shape memory alloy for hard tissue implants by combustion synthesis," *Materials Science and Engineering: A,* vol. 366, pp. 114-119.

[28] Y.-H. Li, L.-J. Rong, and Y.-Y. Li, 2002, "Compressive property of porous NiTi alloy synthesized by combustion synthesis," *Journal of Alloys and Compounds,* vol. 345, pp. 271-274.

[29] A. Salito, U. Van Osten, and F. Brime, 1998, "Gentle Coating Technique," *SULZER TECHNICAL REVIEW,* pp. 34-37.

[30] H. Herman and D. R. Marantz1985 "Process for thermally spraying porous metal coatings on substrates," ed: Google Patents.

[31] J. R. Groza and A. Zavaliangos, 2000, "Sintering activation by external electrical field," *Materials Science and Engineering: A,* vol. 287, pp. 171-177.

[32] R. Miyao, M. OMORI, F. WATARI, A. YOKOYAMA, H. MATSUNO, T. HIRAI, and T. KAWASAKI, 2000, "Fabrication of functionally graded implants by spark plasma sintering and their properties," *Journal of the Japan Society of Powder and Powder Metallurgy,* vol. 47, pp. 1239-1242.

[33] J. Schneider, 1996, "Plasma activated sintering of ceramic materials," *Ceram. Trans. Vol. 79,* pp. 143-151.

[34] N. G. D. Murray, C. A. Schuh, and D. C. Dunand, 2003, "Solid-state foaming of titanium by hydrogen-induced internal-stress superplasticity," *Scripta materialia,* vol. 49, pp. 879-883.

[35] M. C. Melican, M. C. Zimmerman, M. S. Dhillon, A. R. Ponnambalam, A. Curodeau, and J. R. Parsons, 2001, "Three-dimensional printing and porous metallic surfaces: A new orthopedic application," *Journal of Biomedical Materials Research,* vol. 55, pp. 194-202.

[36] J. P. Li, J. R. de Wijn, C. A. Van Blitterswijk, and K. de Groot, 2006, "Porous Ti6Al4V scaffold directly fabricating by rapid prototyping: Preparation and in vitro experiment," *Biomaterials,* vol. 27, pp. 1223-1235.

[37] D. K. Pattanayak, A. Fukuda, T. Matsushita, M. Takemoto, S. Fujibayashi, K. Sasaki, N. Nishida, T. Nakamura, and T. Kokubo, 2011, "Bioactive Ti metal analogous to

human cancellous bone: Fabrication by selective laser melting and chemical treatments," *Acta Biomaterialia,* vol. 7, pp. 1398-1406.

[38] S. M. O. b. H. Shen a, D.C. Dunand b, L.C. Brinson a,b,*, "Numerical modeling of pore size and distribution in foamed titanium," *Mechanics of Materials 38 (2006) 933–944,*

[39] L. Salvo, P. Cloetens, E. Maire, S. Zabler, J. J. Blandin, J. Y. Buffière, W. Ludwig, E. Boller, D. Bellet, and C. Josserond, 2003, "X-ray micro-tomography an attractive characterisation technique in materials science," *Nuclear Instruments and Methods in Physics Research Section B: Beam Interactions with Materials and Atoms,* vol. 200, pp. 273-286.

[40] S. W. Smith,2003 *Digital signal processing: a practical guide for engineers and scientists*: Access Online via Elsevier.

[41] G. Wang, M. W. Vannier, M. W. Skinner, M. G. Cavalcanti, and G. W. Harding, 1998, "Spiral CT image deblurring for cochlear implantation," *Medical Imaging, IEEE Transactions on,* vol. 17, pp. 251-262.

[42] M. Ohkubo, S. Wada, S. Ida, M. Kunii, A. Kayugawa, T. Matsumoto, K. Nishizawa, and K. Murao, 2009, "Determination of point spread function in computed tomography accompanied with verification," *Medical Physics,* vol. 36, pp. 2089-2097.

[43] I. Al-Shakhrah and T. Al-Obaidi, 2003, "Common artifacts in computerized tomography: A review," *Applied Radiology,* vol. 32, pp. 25-32.

[44] J. F. Barrett and N. Keat, 2004, "Artifacts in CT: Recognition and avoidance1," *Radiographics,* vol. 24, pp. 1679-1691.

[45] B. Münch, P. Trtik, F. Marone, and M. Stampanoni, 2009, "Stripe and ring artifact removal with combined wavelet-Fourier filtering," *Opt. Express,* vol. 17, pp. 8567-8591.

[46] Michael Ashby, Tony Evans, N. A. Fleck, J.W. Hutchinson, H.N.G. WAdley, and L. J. Gibson,2000 *Metal Foams A Design Guide*: Butterworth Heinmann.

[47] M. Guden, E. Celik, E. Akar, and S. Cetiner, (2005), " Compression testing of a sintered Ti6Al4V powder compact for biomedical applications," *Materials Characterization,* vol. 54 pp. 399- 408.

[48] T. Imwinkelried, (2007), " Mechanical properties of open-pore titanium foam.," *J. Biomed. Mater. Res.,* vol. 81A, pp. 964-970.

[49] M. F. Ashby, A. G. Evans, N. A. Fleck, J. W. Hutchinson, H. N. G. Wadley, and L. J. Gibson,(2000) *Making metal foams. Metal foams: a design guide. Chapter 2*: Butterworth-Heinemann. ISBN 0-7506-7219-6.

[50] M. Gudena, T. E. Celikc, E. Akara, and S. Cetiner, 2005, "Compression testing of a sintered Ti6Al4V powder compact for biomedical applications," *Materials Characterization,* vol. 54, pp. 399– 408.

[51] C. E. Wen, Y. Yamada, K Shimojima, Y. Chino, T. Asahina, and Mabuchi, (2002), "Processing and Mechanical properties of autogenious titanium implant materials," *Journal of Material science: Materials in medicine,* pp. 397-401.

[52] L. J. Gibson, 2000, "MECHANICAL BEHAVIOR OF METALLIC FOAMS," *Annu. Rev. Mater. Sci.,* vol. 30, pp. 191–227.

[53] V. S. Deshpande and N. A. Fleck, 2001, "Multi-axial yield behaviour of polymer foams," *Acta Materialia,* vol. 49, pp. 1859-1866.

[54] Y. Masso Moreu and N.J. Mills, 2004, "Rapid hydrostatic compression of low-density polymeric foams," *Polymer Testing,* vol. 23, pp. 313–322.

[55] George T. Gray, 2000, "Classic Split Hopkinson Pressure Bar Testing," *ASM International*, pp. 462-476.

[56] B. Hopkinson, 1914, "A method of Measuring the Pressure Produced in the Detonation of High Explosives or by the Impact of Bullets " *Philos Trans R. Soc.*, vol. 213, pp. 437-456

[57] J. E. Field, S. M. Walley, W. G. Proud, H. T. Goldrein, and C. R. Siviour, 2004, "Review of experimental techniques for high rate deformation and shock studies," *International Journal of Impact Engineering*, vol. 30, pp. 725-775.

[58] F. Yi, Z. Zhu, F. Zu, S. Hu, and P. Yi, 2001, "Strain rate effects on the compressive property and the energy-absorbing capacity of aluminum alloy foams," *Materials Characterization*, vol. 47, pp. 417-422.

[59] S. Ouellet, D. Cronin, and M. Worswick, 2006, "Compressive response of polymeric foams under quasi-static, medium and high strain rate conditions," *Polymer Testing*, vol. 25, pp. 731-743.

[60] K. T. Ramesh, 2010 *Handbook of experimental solid mechanics*, Springer.

[61] Marc A. Meyers,"Dynamic behaviour of materials," ed. New York: Willey Interscience.

[62] G. I. Taylor, 1948, "The use if flat ended projectiles for determining dynamic yield stress," *Proceedings of the Royal Society of London Series a-Mathematical and Physical Sciences*, vol. 194, pp. 289-299.

[63] W. E. Carrington and M. L. V. Gayler, 1948, "The use of flat-ended projectiles for determining dynamic yield stress," *Proceedings of the Royal Society of London Series a- Mathematical and Physical Sciences*, vol. 194, pp. 323-331.

[64] A. C. Whiffin, 1948, "The use of flat ended projectiles for determining dynamic yield stress," *Proceedings of the Royal Society of London Series a-Mathematical and Physical Sciences*, vol. 194, pp. 300-322.

[65] B. Plunkett, O. Cazacu, R. A. Lebensohn, and F. Barlat, 2007, "Elastic-viscoplastic anisotropic modeling of textured metals and validation using the Taylor cylinder impact test," *International Journal of Plasticity*, vol. 23, pp. 1001-1021.

[66] P. J. Maudlin, G. T. Gray, C. M. Cady, and G. C. Kaschner, Jun. 1999., "High-rate material modelling and validation using the Taylor cylinder impact test," *Philosophical Transactions of the Royal Society A: Mathematical, Physical and Engineering Sciences*, vol. 357, pp. 1707-1729.

[67] N. K. Bourne, K. Bennett, A. M. Milne, S. A. MacDonald, J. J. Harrigan, and J. C. F. Millett, 2008, "The shock response of aluminium foams," *Scripta Materialia*, vol. 58, pp. 154-157.

[68] E. Wielewski, M. R. Arthington, C. R. Siviour, S. Carter, F. Hofmann, A. M. Korsunsky, and N. Petrinic, 2010, "A method for the in situ measurement of evolving elliptical cross-sections in initially cylindrical Taylor impact specimens " *The Journal of Strain Analysis for Engineering Design*, vol. vol. 45, pp. pp. 429-437.

[69] Gibson L. and M. Ashby, 1997 *Cellular Solids Structure and Properties*. New York: Cambridge University Press.

[70] A. N. Gent and A. G. Thomas, 1959, "The deformation of foamed elastic materials," *Journal of Applied Polymer Science*, vol. 1, pp. 107-113.

[71] L. J. Gibson, 2005, "Biomechanics of cellular solids," *Journal of Biomechanics*, vol. 38, pp. 377-399.

[72] T. Mori and K. Tanaka, 1973, "Average stress in matrix and average elastic energy of materials with misfitting inclusions," *Acta Metallurgica*, vol. 21, pp. 571-574.

[73] S. Demiray, W. Becker, and J. Hohe, 2006, "Homogenisation of elasto-plastic open-celled foams," *PAMM · Proc. Appl. Math. Mech.,* vol. 6, pp. 473–474.

[74] V. S. Deshpande and N. A. Fleck, 2000, "Isotropic constitutive models for metallic foams," *Journal of the Mechanics and Physics of Solids,* vol. 48, pp. 1253-1283.

[75] S. Abrate, 2008, "Criteria for Yielding or Failure of Cellular Materials," *Journal of SANDWICH STRUCTURES AND MATERIALS,* vol. 10, pp. 0005–47.

[76] N. A. F. V. S. Deshpande, 2000, "Isotropic constitutive models for metallic foams," *Journal of the Mechanics and Physics of Solids,* vol. 48, p. 1253±1283.

[77] L.-P. Lefebvre, E. Baril, and M. N. Bureau, (2009), "Effect of the oxygen content in solution on the static and cyclic deformation of titanium foams," *J Mater Sci Mater in Med* vol. 20, p. 2223:2223.

[78] D. J. Jorgensen and D. C. Dunand, 15 January 2010, " Ti-6Al-4V with micro- and macropores produced by powder sintering and electrochemical dissolution of steel wires," *Materials Science and Engineering: ,* vol. Volume 527, pp. Pages 849-853.

[79] S. Nemat-Nasser, W. G. Guo, and J. Y. Cheng, (1999), "Mechanical properties and deformation mechanisms of commercially pure Titanium," *Acta mater.,* vol. Vol. 47, p. 3705±3720.

[80] A. Rouxel and C. Y. Chiem, (1988), " Strain-Rate History Effects on TiAl6V4 Titanium Alloy," *Impact Loading and Dynamic Behaviour of Materials,* vol. Vol. 2, pp. 601-608.

[81] C. E. Wen, M. Mabuchi, Y. Yamada, K. Shimojima, Y. Chino, and T. Asahina, 2001, "Processing of biocompatible porous Ti and Mg " *Scripta Materialia,* vol. 45, pp. 1147-1153

[82] N. Tuncer and G. Arslan, (2009), " Designing compressive properties of titanium foams," *J Mater Sci Mater in Med,* vol. Vol. 44, pp. 1477-1484.

[83] S. Thelen, F. Barthelat, and L. C. Brinson, (2004), "Mechanics considerations for microporous titanium as an orthopedic implant material," *J. Biomed. Mater. Res.,* vol. 69A, pp. 601-610.

[84] M. Ashby and L. Gibson, 1997 *Mechanics of foams. Cellular solids: structure and properties. Chapter 5*. New York: Cambridge University Press.

[85] V. S. Deshpande and N. A. Fleck, (2000), "Isotropic constitutive models for metallic Foams," *Journal of the Mechanics and Physics of Solids,* vol. 48 p. 1253±1283.

[86] D. D. Radford, V. S. Deshpande, and N. A. Fleck, (2005), "The use of metal foam projectile to simulate shock loading on a structure," *Int. J. Impact Eng.* , pp. 31:1152-1171

[87] L.-P. Lefebvre and Y. Thomas, 9 Dec 2003., " Method of Making Open Cell Material," Issue.

[88] T. Imwinkelried, 2007, "Mechanical properties of open-pore titanium foam," *Journal of Biomedical Materials Research Part A,* vol. 81A, pp. 964-970.

[89] C. E. Wen, Y. Yamada, K. Shimojima, Y. Chino, T. Asahina, and M. Mabuchi, 2002/04/01 2002, "Processing and mechanical properties of autogenous titanium implant materials," *Journal of Materials Science: Materials in Medicine,* vol. 13, pp. 397-401.

[90] P. Sevilla, C. Aparicio, J. A. Planell, and F. J. Gil, 2007, "Comparison of the mechanical properties between tantalum and nickel–titanium foams implant materials for bone ingrowth applications," *Journal of Alloys and Compounds,* vol. 439, pp. 67-73.

[91] C. Wen, Y. Yamada, K. Shimojima, Y. Chino, H. Hosokawa, and M. Mabuchi, 2002, "Novel titanium foam for bone tissue engineering," *Journal of materials research,* vol. 17, pp. 2633-2639.

[92] Synergy,2006 "Kaleidagraph 4.0 user manual," S. software, Ed., 4.0 ed.

[93] B. L. Eppley and A. M. Sadove, 1990, "Effects of material porosity on implant bonding strength in a craniofacial model," *J Craniofac Surg,* vol. 1, pp. 191-5.

[94] V. Karageorgiou and D. Kaplan, 2005, "Porosity of 3D biomaterial scaffolds and osteogenesis," *Biomaterials,* vol. 26, pp. 5474-5491.

[95] M. Navarro, A. Michiardi, O. Castaño, and J. A. Planell, October 6, 2008 2008, "Biomaterials in orthopaedics," *Journal of The Royal Society Interface,* vol. 5, pp. 1137-1158.

[96] Arabnejad Khanoki S and Pasini D, "Multiscale design and multiobjective optimization of orthopedic hip implants with functionally graded cellular material,"

[97] W. Niu, C. Bai, G. Qiu, and Q. Wang, 2009, "Processing and properties of porous titanium using space holder technique," *Materials Science and Engineering: A,* vol. 506, pp. 148-151.

[98] I.-H. Oh, N. Nomura, N. Masahashi, and S. Hanada, 2003, "Mechanical properties of porous titanium compacts prepared by powder sintering," *Scripta Materialia,* vol. 49, pp. 1197-1202.

[99] Thomas Imwinkelried, 2007, "Mechanical properties of open-pore titanium foam," *Wiley InterScience,* vol. 84A,

[100] Y. Li, Z. Guo, J. Hao, and S. Ren, 2008, "Porosity and mechanical properties of porous titanium fabricated by gelcasting," *Rare Metals,* vol. 27, pp. 282-286.

[101] P. Siegkas, V. L. Tagarielli, N. Petrinic, and L. P. Lefebvre, 2011, "The compressive response of a titanium foam at low and high strain rates," *J Mater Sci* vol. 46, pp. 2741–2747.

[102] M. Arkadiusz Sitek*, IEEE, Ronald H. Huesman, Fellow, IEEE, and Grant T. Gullberg, Fellow, IEEE, "Tomographic Reconstruction Using an Adaptive
Tetrahedral Mesh Defined by a Point Cloud," *IEEE TRANSACTIONS ON MEDICAL IMAGING, VOL. 25, NO. 9, SEPTEMBER 2006,*

[103] H. Shen, S. M. Oppenheimer, D.C. Dunand, and L.C. Brinson, (2006), "Numerical modeling of pore size and distribution in foamed titanium," *J. Mechanics of Materials* vol. 38, pp. 933-944.

[104] M. Borovinsek and Z. Ren, 2008, "Computational modelling of irregular open-cell foam under impact loading," *Mat.-wiss. u. Werkstofftech,* vol. 39, pp. P.p.114-120. .

[105] M. Vesenjak, Z. Ren, and A. Ochsner, 2008, "Behaviour of cellular materials under impact loading," *Mat.-wiss. u. Werkstofftech.,* vol. 39, pp. 125-132.

[106] Jorg Hohe and Wilfried Becker, 2003, "Effective mechanical behavior of hyperelastic honeycomps and two dimensional model foams at finite strain," *International Journal of Mechanical Sciences* vol. 45, pp. 891-913.

[107] N. A. Fleck, L. T. Kuhn, and R. M. McMeeking, 1992, "Yielding of metal powder bonded by isolated contacts," *J. Mech. Phys. Solids* vol. 40, pp. 1139-1162.

[108] J. Banhart, 2000/12/01 2000, "Manufacturing routes for metallic foams," *JOM,* vol. 52, pp. 22-27.

[109] R. Singh, P. D. Lee, J. R. Jones, G. Poologasundarampillai, T. Post, T. C. Lindley, and R. J. Dashwood, 2010, "Hierarchically structured titanium foams for tissue scaffold applications," *Acta Biomaterialia,* vol. 6, pp. 4596-4604.

[110] Skyscan. (2011). *NRecon User Manual*.

[111] L. A. Feldkamp, L. C. Davis, and J. W. Kress, 1984/06/01 1984, "Practical cone-beam algorithm," *Journal of the Optical Society of America A,* vol. 1, pp. 612-619.

[112] E. W. Andrews, G. Gioux, P. Onck, and L. J. Gibson, 2001, "Size effects in ductile cellular solids. Part II: experimental results," *International Journal of Mechanical Sciences,* vol. 43, pp. 701-713.

[113] C. R. Siviour, S. M. Walley, W. G. Proud, and J. E. Field, 2005, "The high strain rate compressive behaviour of polycarbonate and polyvinylidene difluoride," *Polymer,* vol. 46, pp. 12546-12555.

[114] M. S. Aly, 2010, "Effect of pore size on the tensile behavior of open-cell Ti foams: Experimental results," *Materials Letters,* vol. 64, pp. 935-937.

[115] Mathworks;, 2002 *Matlab Help Files, Solution of Equations*, Campridge MA.

[116] G. V. (1907), "Nouvelles applications des paramètres continus à la théorie des formes quadratiques. Journal für die Reine und Angewandte Mathematik, 133:97-178, 1907,"

[117] Ansa,2007 *Ansa User's Guide*: Beta CAE Systems.

[118] L. S. T. Corporation, "LS DYNA user's manual Volume 1 Version 971 May 2007,"

[119] K. Hibbitt and Sorensen,2001 *ABAQUS/Standard User's Manual*: Hibbitt, Karlsson & Sorensen.

[120] Abaqus,2009 "Classical metal plasticity, rate dependence-direct tabular data.," in *Analysis User's Manual.*, ed: Simulia Abaqus CAE 6.9 Documentation.

[121] R. von Mises, 1913, " Mechanik der Festen Korper im plastisch deformablen Zustand. ," *Göttin. Nachr. Math. Phys.,* vol. 1, pp. pp. 582–592.

[122] R. Hill, 1998, "The Mathematical Theory of Plasticity," *Oxford University Press,*

[123] A. L. Gurson, 1977, "Continuum Theory of Ductile Rupture by Void Nucleation and Growth," *Journal of Engineering Materials and Technology,* vol. 99 pp. 2-15.

[124] Simulia, 2009 *Abaqus theory manual 6.9: 4.3.6 Porous plasticity*.

[125] Viggo Tvergaard, 1981, "Influence of voids on shear band instabilities under plane strain conditions," *International Journal of Fracture,* vol. 17,

[126] H. X. Zhu, J. R. Hobdell, and A. H. Windle, 2000, "Effects of cell irregularity on the elastic properties of open-cell foams," *Acta Materialia,* vol. 48, pp. 4893-4900.

[127] G. W. Ma, Z. Q. Ye, and Z. S. Shao, 2009, "Modeling loading rate effect on crushing stress of metallic cellular materials," *International Journal of Impact Engineering,* vol. 36, pp. 775-782.

[128] W. J. Drugan and J. R. Willis, 1996, "A micromechanics-based nonlocal constitutive equation and estimates of representative volume element size for elastic composites," *Journal of the Mechanics and Physics of Solids,* vol. 44, pp. 497-524.

[129] M. Ostoja-Starzewski, 1998, "Random field models of heterogeneous materials," *International Journal of Solids and Structures,* vol. 35, pp. 2429-2455.

[130] H. Shen, S. M. Oppenheimer, D. C. Dunand, and L. C. Brinson, 2006, "Numerical modeling of pore size and distribution in foamed titanium," *Mechanics of Materials,* vol. 38, pp. 933-944.

[131] H. Shen and L. C. Brinson, 2006, "A numerical investigation of the effect of boundary conditions and representative volume element size for porous Titanium," *JOURNAL OF MECHANICS OF MATERIALS AND STRUCTURES,* vol. 1, pp. 1179-1204.

[132] S.A. Ansa, "v. 12. 1.3. User's Guide, Chapter 10, Volume Meshing. ," ed: Beta CAE Systems, pp. 503-575.

[133] L. W. Meyer, L. Krüger, S. V. Razorenov, and G. I. Kanel, (2003), "Investigation of dynamic flow and Strength properties of Ti-6-22-22S at normal and elevated temperatures," *International Journal of Impact Engineering* vol. 28, pp. S. 877-890.